Shape and Stability of Liquid Threads and Jets: A Link to Droplet Formation

W. G. N. van Heugten

Thesis committee

Promotor

Prof. Dr C. J. M. van Rijn

Professor of Micro Fluidics and Nanotechnology for Food and Health

Wageningen University

Other members

Prof. Dr J. van der Gucht , Wageningen University

Prof. Dr M. T. Kreutzer, Delft University of Technology

Prof. Dr J. H. Snoeijer, University of Twente, Enschede

Dr H. Reinten, Océ Technologies BV, Venlo

This research was conducted under the auspices of the Graduate School VLAG (Advanced studies in Food Technology, Agrobiotechnology, Nutrition and Health Sciences).

Shape and Stability of Liquid Threads and Jets: A Link to Droplet Formation

W. G. N. van Heugten

Thesis

submitted in fulfilment of the requirements for the degree of doctor

at Wageningen University

by the authority of the Rector Magnificus

Prof. Dr A.P.J. Mol,

in the presence of the

Thesis Committee appointed by the Academic Board

to be defended in public

on Monday 7 December 2015

at 4 p.m. in the Aula.

W. G. N. van Heugten

Shape and Stability of Liquid Threads and Jets: A Link to Droplet Formation

160 pages.

PhD thesis, Wageningen University, Wageningen, NL (2015)

With references, and summary in English

ISBN: 978-94-64-6257-570-7

Table of contents

Chapter 1

General introduction

This thesis aims to provide a better understanding of relevant fluid dynamics in microfluidic systems for the formation of uniformly sized droplets. Growing droplets made from a bulk source have often liquid threads or jets in between to supply liquid to the droplet. Liquid threads and jets are however known to be instable and finding parameters determining their instability/stability will possibly promote a more controlled formation of uniformly sized droplets. Droplet formation processes in this chapter are explained for cross-flow, co-flow and flow focussing microfluidic devices and different breakup processes of liquid threads and jets will be given. Relevant fluid dynamics within microfluidic systems will be treated by the introduction of dimensionless numbers; they represent the ratio between different acting forces, such as viscous forces, surface tension force, and inertial force. These force/pressure ratios can be expressed with relevant fluid dynamic parameters, such as viscosity, interfacial tension, mass density and velocity of the fluid within a specific fluid channel confinement represented by a typical length scale. The dimensionless Reynolds, Weber and Capillary numbers can be associated with the stability of liquid threads and jets.

1. General introduction to microfluidics

Microfluidics is the technology and science to study and handle small fluid volumes by using microfluidic devices. The volumes are typically 10^{-9}-10^{-12} L with dimensions in the order of tens of micrometres to several hundreds of micrometres for the channel diameter (Whitesides 2006). The behaviour of confined single and multiple phase flows in such channels is a broad object of study. Microfluidics is also a technology for miniaturisation of current macro-fluidics application, for example, from a laboratory to a Lab-on-a-Chip, or a process plant to a Process-on-a-Chip. Microfluidics is applied in synthesis chemistry (Nieuwland et al. 2011) and high-throughput sample preparation for analysis (Shen et al. 2013).

In microfluidics understanding processes for the formation of uniform droplets originating from confined liquid threads or jets is of interest for both science and applications. Well-defined emulsions with controlled droplet sizes are of great importance for many industries, such as food, cosmetics and pharmaceuticals.

1.1. Physical parameters in fluid dynamics

Fluid dynamics within microfluidic systems are dependent on driving forces to set the fluid in motion and their effects are determined by physical parameters of the intrinsic fluid or interface, which are mass density ρ, viscosity η, and interfacial tension γ.

Mass density ρ

The two physical effects in fluids in which mass density is important are inertia and buoyancy. Inertia of a fluid is the resistance of that fluid to a change in motion. Inertia becomes important when a fluid accelerates/decelerates, for example, a rain droplet falling on a water surface. Inertia plays also an important role in the transition from laminar flow to one in which the fluid is turbulent. Buoyancy force (formulated by Archimedes' principle) is the force that a body experiences when it is placed in a fluid with another density than the body. The body can also be another fluid that is immiscible with the other fluid. For example an oil droplet will float when brought in water.

Viscosity η

The viscosity parameter η determines the resistance to flow of a fluid when a driving force or pressure is exerted. Layers of fluid with different velocities, forming a parabolic profile (laminar flow regime), are formed when a fluid flows at low flow rates in a tube. The velocity of the fluid v is fastest in the centre of the pipe is and lowest near the wall of the pipe where the fluid velocity is often zero (no slipping flow). Two adjacent layers experience friction and determine the amount of shear between these layers of fluid. The effect of shear to obtain a certain fluid velocity is determined by its viscosity. There is a linear relation between generated flow at low fluid velocities and the pressure difference between both ends of the tube (Poiseuille 1840, Sutera & Skalak 1993).

Interfacial tension γ

The behaviour of an interface can be explained by the physical concept of interfacial- or surface tension. Interfacial tension and surface tension are related physical parameters, where "surface tension" is used for an air-liquid interface, and "interfacial tension" is used for a liquid-liquid interface. Interfacial and surface tension are always tensile (resist against stretching), due to the cohesive forces between identical molecules (mainly Van der Waals forces) and aim for the smallest surface or interface area as possible.

An interface between two fluids is often curved, especially if the curved surface can acquire a smaller size than the corresponding flat surface given the boundary conditions. Thomas Young and Pierre-Simon Laplace found that a pressure difference Δp over a curved interface exists and scales with the two principle curvatures ($1/R_1$ and $1/R_2$) and interfacial tension γ (equation 1) (Laplace 1806, Young 1805):

$$\Delta p = \frac{\gamma}{R_1} + \frac{\gamma}{R_2} \tag{1}$$

R_1 and R_2 are the radii related to the two components of curvature. The two components of curvature are equal in a sphere (see figure 1). The two components of curvature in other shapes differ from each other. The $1/R_2$ component of curvature is zero in the special case of a cylinder.

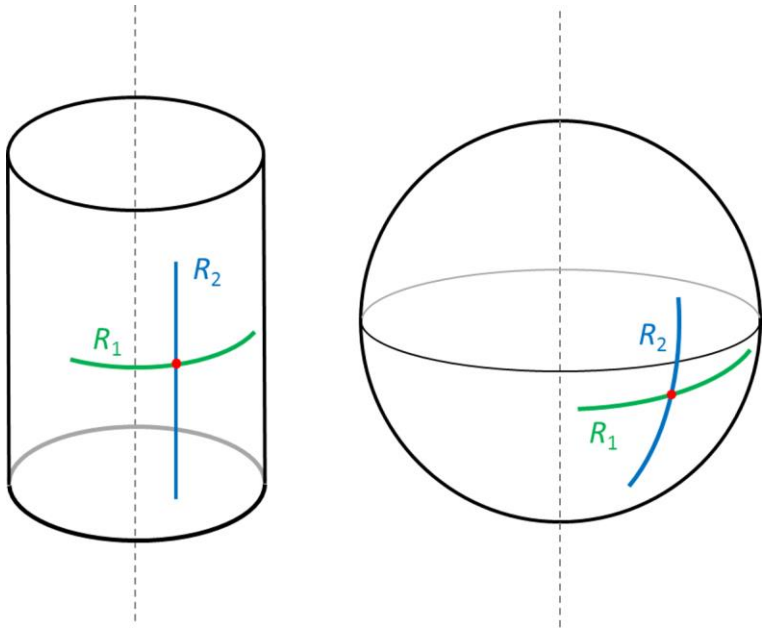

Figure 1. Radii of components of curvature R_1 and R_2 for a cylinder and a sphere.

The shape of a liquid may form to the shape of a container or spread on a solid surface. The effect of adhesion of a liquid with a solid is called wetting. Wetting changes the shape of a fluid, because interaction of liquid molecules with the solid surface lowers the interfacial energy.

1.1.1. Dimensionless numbers

The behaviour of fluids in microfluidics depends on the different physical forces that can act on the fluids or interfaces. Dimensionless numbers express the relative importance of these forces within a given fluidic system configuration. A dimensionless number is normally defined as a ratio between two different physical forces or pressures.

The relation between viscous forces and interfacial forces is given by the capillary number Ca, and is used to indicate the stability of an interface. If the interface is instable, breakup of a liquid thread results in droplet formation. Viscous forces in a flowing fluid always oppose interfacial forces:

$$Ca \equiv \frac{viscous\ pressure}{surface\ tension\ pressure} \equiv \frac{\eta v}{\gamma} \tag{2}$$

The Reynolds number *Re* is often used in microfluidics to determine the type of flow regime and is based on the ratio between inertial and viscous forces:

$$Re \equiv \frac{inertial\ pressure}{viscous\ pressure} \equiv \frac{\rho v D}{\eta} \tag{3}$$

With D representing a characteristic length scale, e.g. a droplet diameter or channel height of a microfluidic device. At high *Re* (typically above 2300) inertia is dominant, which marks a turbulent flow regime. At low *Re* (typically below 1000) viscous effects are dominant marking a laminar flow regime.

The Weber number *We* measures the relative importance of inertial and interfacial forces:

$$We \equiv \frac{inertial\ pressure}{surface\ tension\ pressure} \equiv \frac{\rho v^2 D}{\gamma} \tag{4}$$

We is useful for analysis of droplet formation and thin film flows at high velocities, to verify if inertial effects dominate the flow characteristics. Please note that *Re = We/Ca.*

Bond number (also named Eötvös number *Eo*) *Bo* measures the effect of surface tension on a liquid body in a gravity field. *Bo* indicates to what extent a spherical drop is deformed by gravity.

$$Bo \equiv Eo \equiv \frac{\Delta\rho g D^2}{\gamma} \tag{5}$$

With g is the standard gravity, and $\Delta\rho$ is the density difference between droplet and its surrounding medium.

There are many more dimensionless numbers. Ohnesorge number *Oh* and Froude number *Fr* are also mentioned in this thesis. *Oh* relates three forces: viscous, inertial and interfacial tension force, and *Fr* is a ratio between inertial and gravity force.

1.2. Droplet formation in microfluidics

In free surface flow, droplets are the most stable form in which finite liquid volumes appear. Droplet formation is driven by interfacial energy minimization, which occurs by

forming a spherical shape, and then the ratio between interfacial area and liquid volume is minimized. Other, stable liquid free surface shapes can be observed as well, such as a sessile drop that has a deformed spherical shape due to gravity (cf. Bond number *Bo*). Less stable liquid free surface shapes can also be observed, for example, when a droplet is separated from a source (for example from a dripping tap), a liquid thread is often formed.

In microfluidics an outer fluid (the fluid that carries the droplets) and an immiscible inner fluid (the fluid that is dispersed in the outer fluid) are brought together. Droplet formation is often controlled by forces exerted by the outer fluid on the inner fluid. The outer fluid applies a friction or shear force on the inner fluid volume via their interface. The front part of the inner fluid will be pushed away from its origin resulting in a droplet that is attached via a liquid thread to the source of the inner fluid. The droplet is dragged away further from the source of inner fluid and eventually breaks up (Christopher & Anna 2007, Seemann et al. 2012, Yuan & Williams 2014).

In two phase microfluidics three major types of microfluidic structures have been studied for droplet formation: T-junction, co-flow and flow focussing devices (figure 2).

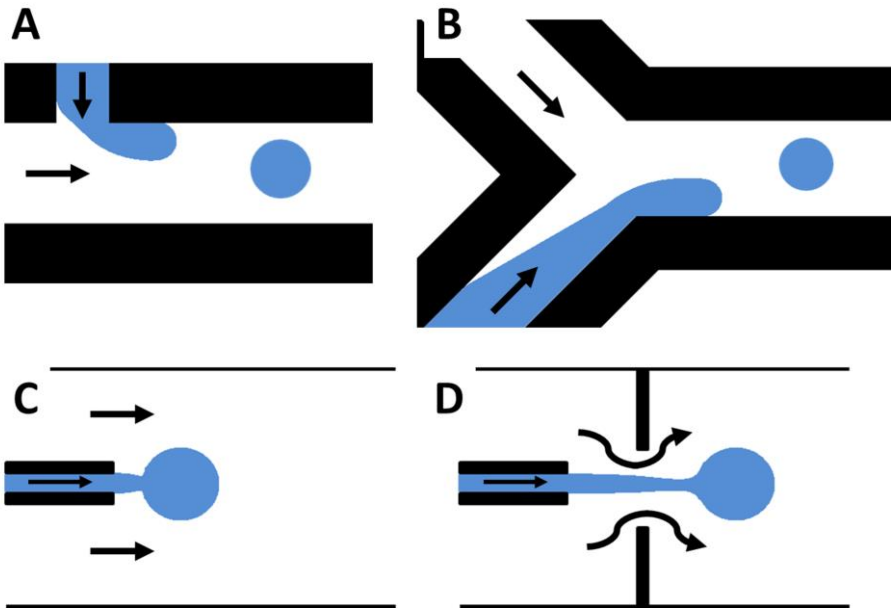

Figure 2. Schematics of microfluidic approaches to study droplet formation: **A** T-junction, **B** Y-junction, **C** co-flow and **D** flow focussing. Flow directions of the inner fluid and the outer fluid are marked by arrows.

The differences between these microfluidic structures are in how the inner and outer fluids are brought together. In T-junction, the outer fluid flows perpendicular to the initial flow direction of the inner fluid from the nozzle. In co-flow, the outer fluid flows parallel to the flow of the inner fluid. In flow focussing a flow restrictor is inserted in the microchannel to locally apply a high shear on the inner fluid.

1.2.1. Cross flow emulsification

Generating a single stream of uniform droplets was first demonstrated in a T-junction microchannel (Thorsen et al. 2001). T-junction microfluidic systems can be quasi-2D when the formed droplets are larger than the height of the channel. This confinement squeezes droplets into discoid shapes. Water in oil (W/O) and oil in water (O/W) emulsions can be made by T-junction systems with droplet sizes ranging from tens up to hundreds of micrometres (Nisisako et al. 2002, Zhao et al. 2006). The use of T-junction microchannels yields uniform sized droplets, typically with a coefficient of variation (CV) below 5% (Steegmans et al. 2009). Although several thousands of droplets per second can be realised, for industrial scale applications even a higher through-put is required. Parallelisation was demonstrated to be possible without increasing the CV (Nisisako & Torii 2008).

Understanding the effects of physical parameters, such as, flow rates, channel dimensions, η, γ, effect of surfactants and wettability of the channel walls on droplet formation in T-junctions have been reviewed by (Christopher & Anna 2007, Seemann et al. 2012, Yuan & Williams 2014). Models have been derived from these experimental data to predict droplet sizes. In general, three different regimes can be distinguished and are related to the capillary number Ca of the outer fluid (equation 2).

The physical parameters γ and η of the outer fluid are assumed to be constant. Droplet formation will go from squeezing regime, to dripping regime, to subsequently jetting regime upon increasing v of the outer fluid (figure 3). Subdivisions of these regimes have been recognised.

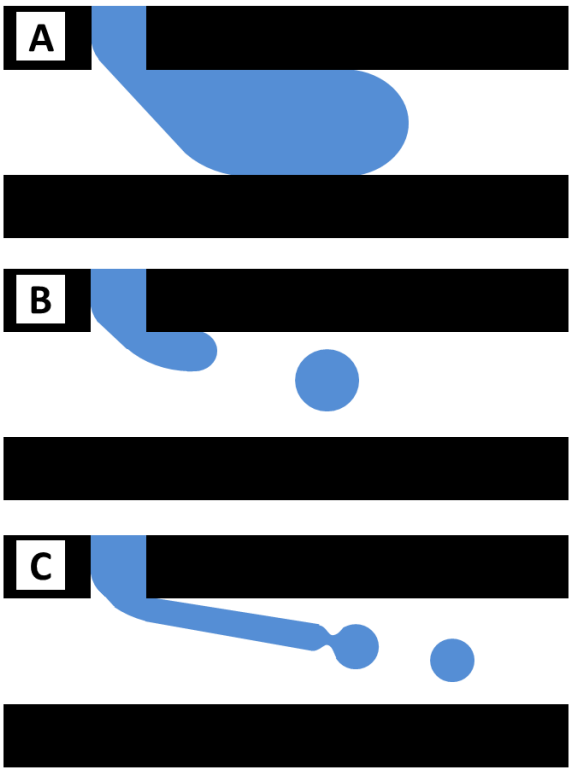

Figure 3. Three regimes of cross flow droplet formation in microfluidic devices from T-junctions: **A** squeezing flow, **B** dripping and **C** jetting.

T-junction droplet formation is thought to be a two-step process: growth of the droplet followed by detachment (Peng & Williams 1998). An empirical model is based on initial growth of the droplet until shear forces take over. During the time between initial instability and breakup liquid is added to the droplet (Steegmans et al. 2009).

A slightly different microfluidic device is the Y-junction (figure 2B). The breakup mechanism is thought to be simpler than in a T-junction, although the droplet formation process is the same. Droplet sizes depend mainly on the flow of the inner fluid (Steegmans et al. 2010, Ushikubo et al. 2014).

The use of cross flow to shear the inner fluid droplets from the surface of micro-porous glass membranes (Nakashima et al. 1991) was applied much earlier than by using micro-machined membranes (Gijsbertsen-Abrahamse et al. 2004). Micro-machined membranes are also an effective way to scale up T-junction microfluidic systems. The inner fluid is pressed into the outer fluid through a flat sheet with many pores. Uniform

pore size and a uniform shear of the outer fluid on the inner fluid yield uniformly sized droplets (Gijsbertsen-Abrahamse et al. 2004, van Rijn 2004, Spyropoulos et al. 2014).

1.2.2. Co-flow emulsification and flow focussing

Jetting and dripping regimes have also been observed in co-flow emulsification and flow focussing experiments. Two jetting sub-regimes can be classified based on increasing flows of the inner fluid: normal jetting, also known as tip streaming and the widening jet regime (figure 4) (Fu et al. 2012). The transition from widening jetting to dripping is dependent on the Weber number *We* of the inner fluid (equation 4). Squeezing is seen as a special type of dripping in e.g. the T-junction. Similarly, squeezing flow is reached when the flow of the outer fluid is slow and the droplet becomes larger than the channel (Suryo & Basaran 2006).

The widening neck regime is entered when *We* is larger than 2 (Utada et al. 2007), suggesting that inertia of the outer fluid plays a major role in this droplet formation process. A similar widening neck regime in cross flow emulsification at low shear flows was identified by (Meyer & Crocker 2009).

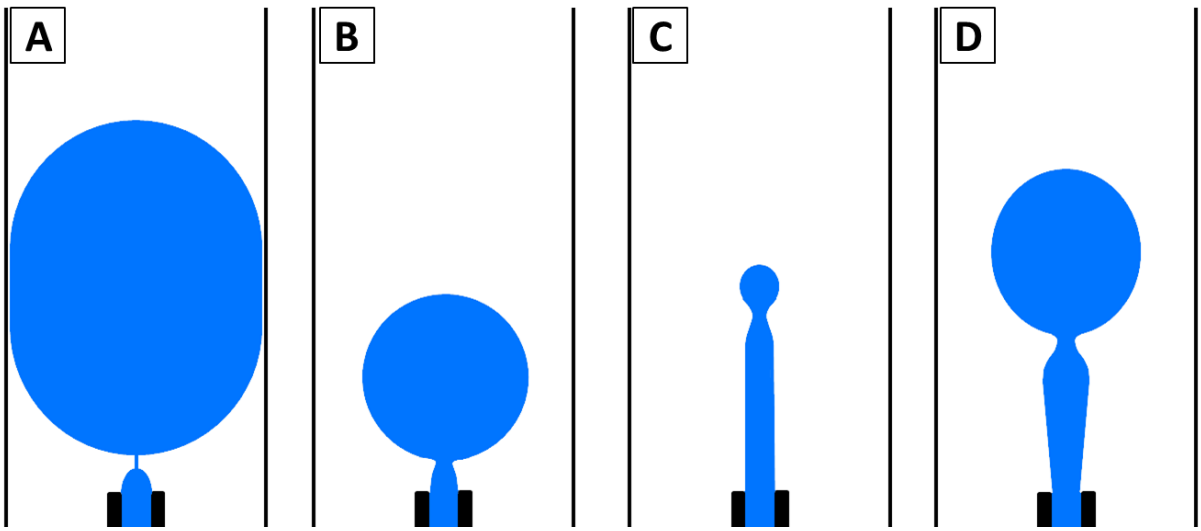

Figure 4. Four different regimes can be recognised in co-flow droplet formation: **A** squeezing regime, **B** dripping regime, **C** jetting regime, and **D** widening jet regime.

The transition of dripping to jetting or tip streaming depends mainly on the flow of the outer fluid (Cramer et al. 2004). In jetting, smaller droplets are formed while they are attached via a long cylindrical neck before breakup. The breakup mechanism follows the Rayleigh-Plateau instability (section 1.3.1) and is initiated by a convective or absolute instability (Lin & Reitz 1998). Absolute instabilities start as perturbations which are amplified at the same position as where they start. Convective instabilities are growing perturbations at a different position relative to the velocity of the liquid thread (Eggers 1997, Huerre & Monkewitz 1990).

The breakup in the dripping regime follows from an absolute instability (Utada et al. 2008). The transition between absolute and convective in a jet (section 1.3.1) is also affected by low inner fluid flow rates (Guillot et al. 2008). The instability happens then at low pressure gradients. Changing these values may cause perturbations showing convective instability towards the droplet at the end of the liquid jet (Colin & Tancogne 2011). The transition from dripping to jetting can be determined by the co-flowing outer liquid (Clanet & Lasheras 1999).

Flow focussing has been done for the first time by focussing a flow of a liquid in a gas stream (Gañán-Calvo 1998) hereby generating a monodispersed fine spray. Vice versa, micro-bubbles have been generated in a liquid stream (Gañán-Calvo & Gordillo 2001).

For flow focussing in liquid-liquid systems, similar regimes have been observed as in cross-flow and co-flow devices (figure 5) (Nie et al. 2008). A major difference is that in flow focussing systems the effective co-flow area is limited to the flow restrictor, which is relatively short. Breakup is observed in the flow restrictor and also satellite droplets may be formed (Anna et al. 2003).

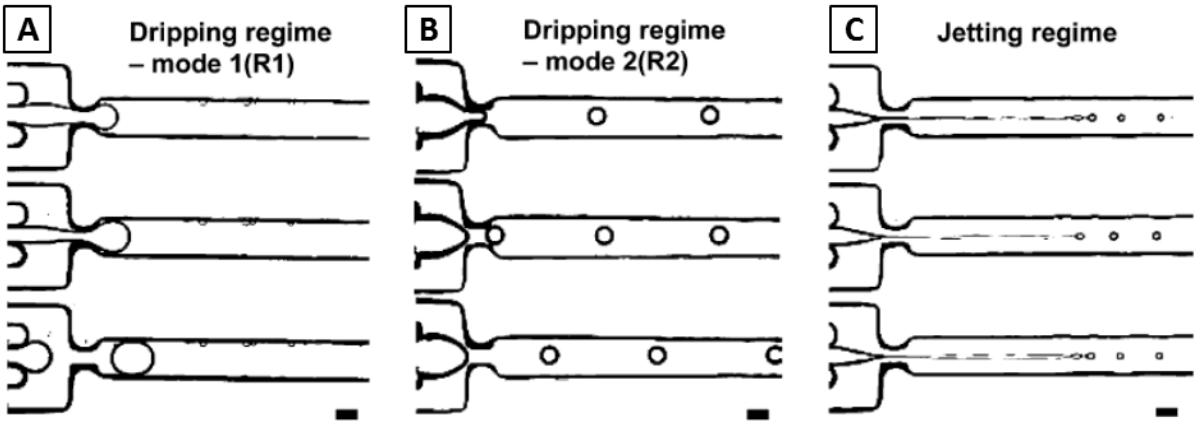

Figure 5. Three flow focussing regimes at different flow rates seen with topview: **A** squeezing flow (channel height is smaller than channel width), **B** dripping, and **C** jetting (Nie et al. 2008). Scale bars are 100 µm.

The flow restrictor in the microfluidic channel is an important factor to tune the inner fluid shape and determines the stability of the interface (Garstecki et al. 2005, Humphry et al. 2009). Increase of the width of the channel increases the hydrodynamic stability of a liquid jet at low capillary numbers *Ca* (Shui et al. 2008). The droplet sizes for a uniform emulsion cannot be predicted from *Ca* alone which suggests that besides interfacial tension and viscous forces other forces contribute to liquid thread instability (Nie et al. 2008).

1.3. Fluid breakup in dripping and jetting regimes

Dripping and jetting regimes can also be distinguished with respect to the stability of the generated liquid thread between the droplet and the nozzle/flow restrictor (Seemann et al. 2012). In general, a relative big droplet detaches relatively close to the nozzle in the dripping regime. Dripping is caused by an absolute instability close to a forming droplet where the instability directly induces breakup. The last stage of breakup is found to follow universal pinch-off (Eggers 2005). In the jetting regime a small droplet is dragged away from the nozzle, but is still attached via a long liquid thread. The subsequent breakup can originate from an absolute instability (near the droplet), but also from a

convective instability caused by perturbations upstream on the liquid jet originating from the nozzle (Utada et al. 2008).

1.3.1. Rayleigh-Plateau instability in jetting regime

Breakup of liquid jets is essentially a surface tension driven process in which a liquid thread breaks up into several droplets (Eggers & Villermaux 2008). This surface tension driven breakup is caused by Plateau–Rayleigh instability and leads always to a decrease of total surface area (figure 6).

Figure 6. Jetting: the convective instability of a liquid thread breaking up into droplets is driven by interfacial tension.

Perturbations (small changes that are induced on an interface) destabilise the liquid thread and are amplified at an optimal wavelength (Rayleigh 1878, 1892). The perturbations that are leading to instability are initiated at the front of the liquid thread and move to the end where the breakup happens and droplets are formed. However, from a computational study, perturbation could also be initiated from the end of the liquid jet (Ali & Umemura 2009). Jetting and optimal wavelength have been examined in a laminar flow field (Cramer et al. 2004).

Liquid jets have been computationally studied by solving the Navier-Stokes equations for incompressible fluids (equation 6) numerically. The equations, based on the change of the impulse of a fluid by forces acting on the fluid, are used to describe the interior of the jet.

$$\rho\left(\frac{\partial v}{\partial t} + v \cdot \nabla v\right) = -\nabla p + \eta \nabla^2 v + F \tag{6}$$

With t time, p pressure, and F representing applied forces. The interface of the jet is described by γ at a local axisymmetric point on the jet and is related to Laplace pressure in ∇p term of equation (6). Breakup of fluids and droplet formation can be well described (Eggers & Dupont 1994, Eggers & Villermaux 2008, Papageorgiou 1995, Subramani et al. 2006, Wilkes et al. 1999).

The Navier-Stokes equations can be simplified by reducing one dimension to axisymmetric systems. Furthermore, the Laplace pressure term can be simplified in the slender jet approximation. In the slender jet approximation the curvatures can be approached by the inverse of the radius of the liquid thread. (Eggers & Villermaux 2008, Kowalewski 1996).

1.3.2. Pinch-off in dripping regime

In the dripping regime, a thin micro-thread can be observed between droplet and liquid jet in the last stage of the breakup process (figure 7). This behaviour during breakup can be explained as a universal pinch-off mechanism derived from Navier-Stokes equations (6). A viscous droplet close to breakup could be explained by the similarity solution (Cohen et al. 1999, Eggers 1993, 2005; Eggers & Dupont 1994, Henderson et al. 1997, Kowalewski 1996, Papageorgiou 1995, Stone & Leal 1989).

The liquid micro-thread that is formed during pinch-off has an asymmetric profile near the point of breakup: steep towards the droplet and slender towards the rest of the liquid thread. The liquid micro-thread between the droplet and the liquid thread can be described by non-linear dynamics and is independent of the initial conditions. The singularity between droplet and liquid thread can be described by similar solutions derived from Navier-Stokes equations. Similar solutions describe fluid shapes that look the same in all time and length scales. The existence of similar solutions makes the pinch-off mechanism universal (Eggers 1993). Pinch-off of a viscous fluid surrounded by another immiscible viscous fluid is also observed computationally (Booty et al. 2013).

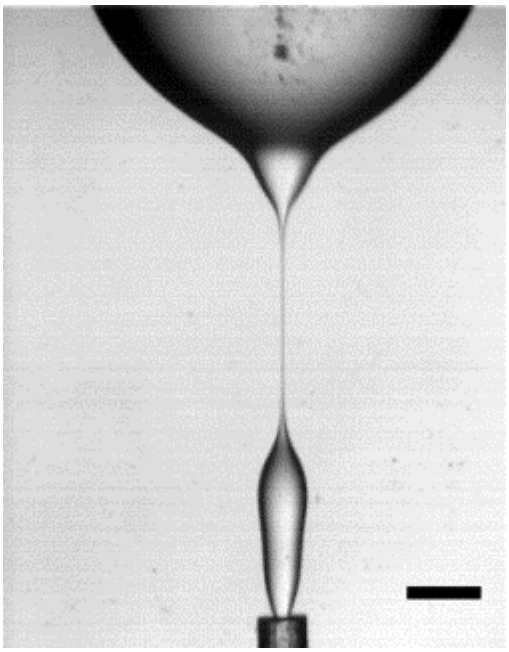

Figure 7. Snapshot of a droplet attached to the bulk liquid via a long micro-thread. The inner fluid is silicone oil (370 mPa·s) and the outer fluid is 1% tween20 in water (1 mPa·s) with an interfacial tension of 5 mN/m. The inner fluid flow rate is 0.5 µL/s. Scale bar is 500 µm.

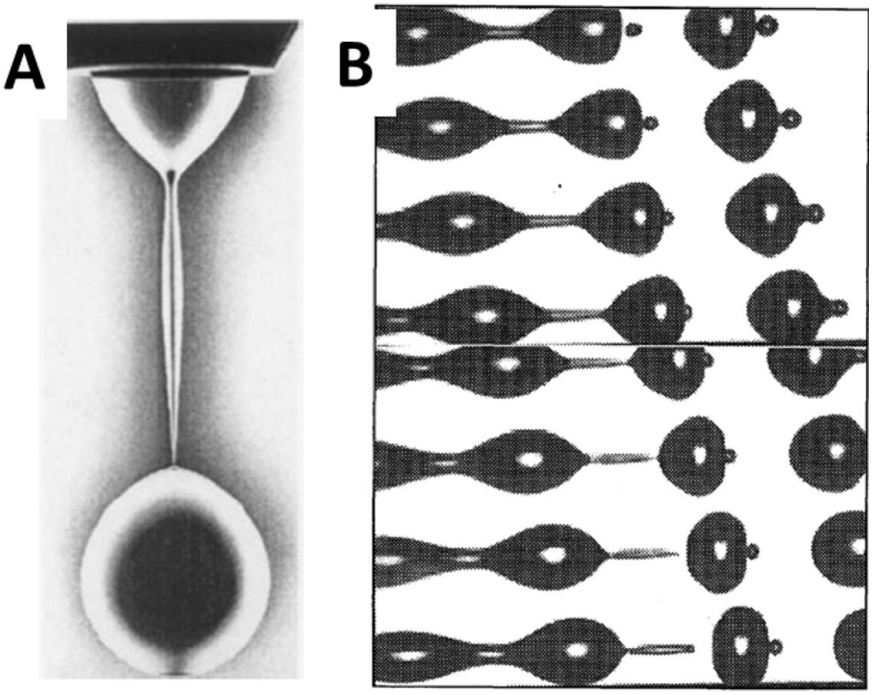

Figure 8. Pinch-off **A** in dripping regime (Cohen et al. 1999), **B** in jetting regime (Kowalewski 1996).

The formation of a liquid thread can be observed in the dripping regime (figure 8A) and also in the jetting regime (figure 8B). The subsequent breakup of the liquid thread often follows the universal pinch-off mechanism (Doshi et al. 2003). The paradox, that pinch-off is universal for different regimes, can be explained by the scalability of the similarity solutions. Two distinguished extremes may be recognised within the solutions derived from Navier-Stokes. For very low viscosities the similar solution is called "Euler" solution. For large viscosities the similar solution is called "Stokes" solution (Eggers 2005). More similar solutions may be recognised within one regime. Infinite similar solutions can be found in both Navier-Stokes regime and Stokes regime. The solution, which is realised in practice, can be found by computational stability analysis against perturbations in time (Brenner et al. 1996, Eggers 2012).

1.4. Emanating jet after droplet impact

Overlooking a nearby surface of a pool when it is raining is a good place to observe the phenomenon; small jets may emanate from the pool surface a short while after raindrops hit the surface. The result after a droplet impact may be either coalescence of that droplet with the water surface, or a splash that results in the formation of crown and/or a central jet (figure 9) (Rein 1996, Yarin 2006).

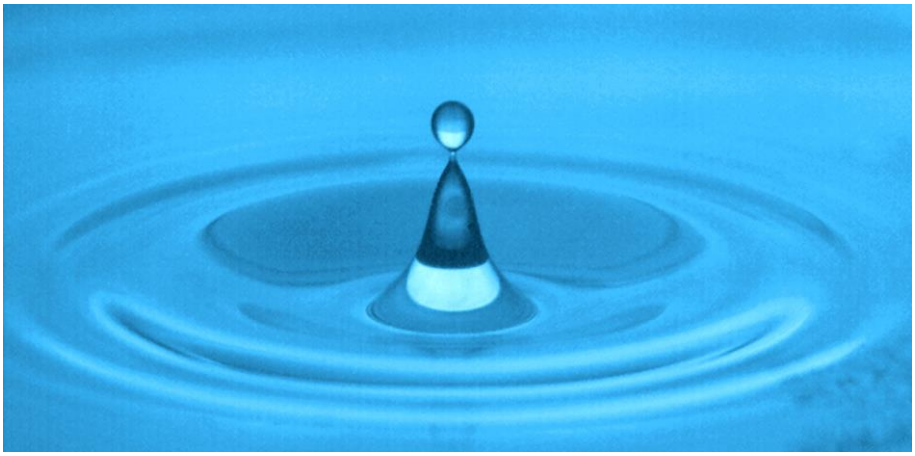

Figure 9. Snapshot of a water jet emanating from a surface (FASTCAM miniUX100, recorded at 6250 frames per second). The horizontal diameter of the droplet on top of the jet is 1.60 mm.

Coalescence of a droplet with the liquid surface occurs typically at low impact velocity (Rein 1996, Rodriguez & Mesler 1985). Quickly the surfaces merge leaving small ripples spreading out on the surface. Further, during the impact of the droplet in the fluid surface the fluid from the liquid surface is flowing up on the surface of the droplet by a thin layer (Marston & Thoroddsen 2008). Complete coalescence is when the droplet is completely absorbed by the liquid surface. Partly coalescence is when a second smaller droplet is formed during impact of the droplet with the liquid surface (Cai 1989, Ray et al. 2010).

An upward result of droplet impact on a liquid surface is called “splash”. Splash means that fluid is launched from the liquid surface and can happen as a crown surrounding the impact crater and/or the formation of a central jet. The transition from coalescence to splash is associated with a higher energy by droplet impact. Models with threshold values were identified for different dimensionless numbers *Oh*, *Fr*, *Re* and *We* and combinations, but no conclusive model has been established (Huang & Zhang 2008, Manzello & Yang 2002, Rein 1993, Zhao et al. 2011). The motion of the fluid below the surface in the form of a vortex ring could be observed in the coalescence regime, but also after a splash, but only when no central jet arises (Rein 1996).

A crater (a cavity on the liquid surface) is formed after droplet impact. The collapse of the crater may entrain air below the liquid surface. Jets are created both upwards and downwards at the points where the crater walls collapse (Gordillo & Gekle 2010, Rein 1996). These two jets are observed clearly when the impact on the liquid surface is created by a flat disc, because then a large amount of air is entrained (Gekle et al. 2009). The impact of the fluid walls during collapse of the crater forms a high pressure point inducing high vertical acceleration and thus the forming of the upward and downward jets (Gekle & Gordillo 2010).

Jetting is in general associated with high speeds and droplet formation. And indeed the initial liquid jet emanating from the crater has a high speed and is emitting a couple of small droplets (Hogrefe et al. 1998, Marston & Thoroddsen 2008). The size of the jet, as well as the droplet on top of the jet, increases in height and width (Rein 1996). Breakup of this droplet was found to follow a dripping mechanism described as pinch-off (Gordillo & Gekle 2010, Stone & Leal 1989).

2. Aim of the thesis

The aim of the thesis is to gain further insight in shape and stability of liquid threads and jets, to gain also more insight in droplet formation processes. The study includes novel attempts to formulate new analytical models to understand (quasi) stable shapes of liquid threads and jets and to predict droplet sizes obtained with different droplet formation techniques.

3. Outline of the thesis

In this thesis droplet formation techniques with microfluidic devices are explored and new insights in shape and stability of liquid threads and jets are obtained under free surface flow and also confined flow conditions.

In **chapter 2** and **3**, a phenomenon called "auto breakup" is investigated. Droplets formed spontaneously, without applying shear forces from the outer fluid, from specially designed capillaries. In **chapter 2**, experiments are described with micro-corrugated and rectangular capillaries, and in **chapter 3**, an analytical model to describe auto breakup was introduced that accurately predicts droplet size. A dimensionless Capillary number was predicted that determines the range of auto breakup and has been verified by experimental results.

In **chapter 4**, the formation and stability of viscous liquid threads was studied. The liquid thread was feeding a large growing droplet and it was shown that the velocity through this liquid thread is important to maintain its stability. A viscous based pressure gradient inside the liquid thread is necessary to oppose the interfacial tension driven squeezing of the liquid thread. A model, based on simplified Navier-Stokes equations, was derived that predicts the conditions for a stable liquid thread and has been verified with experiments. It was derived that the axial shape of a viscous liquid thread is concave and that its radial dimension has initially a cubic dependence with respect to the axial dimension.

In **chapter 5**, the shape and stability of emanating jets and accompanying droplets were studied. Liquid jets were formed by falling droplets impinging on a liquid surface. A new analytical model was derived for the shape of the emanating jet. It is shown that the jet

shape is universal and seems fully determined by a force balance that rules above the fluid surface; an inertial deceleration pressure exerted on the liquid inside the jet and an increasing Laplace pressure along the jet, with both pressures originating from the surface tension. The model has been compared with experimental data and a good conformation is found.

Chapter 6 is a general discussion on the treated fluid dynamics in the former chapters with an outlook on its potential use in microfluidics. Differences and similarities between the studied fluidic systems are discussed. Industrial applications of auto breakup seem feasible given the found operating window for auto breakup in chapter 3.

Chapter 2

Auto breakup: The phenomenon of spontaneous droplet formation at low flow rates

Abstract

In this chapter, the phenomenon of spontaneous droplet formation of an inner fluid at low flow rates confined in a microfluidic channel is studied with a number of experiments. A short overview of known processes of spontaneous droplet formation with micro-engineered microfluidic devices is presented. We have studied auto breakup with a rectangular glass capillary and a round capillary, the latter provided with micro-corrugations. The micro-corrugations enable passive inflow of outer fluid during outflow of the inner fluid. Breakup of the confined liquid thread occurs after a fast necking process leading to auto-breakup and was observed inside the capillary. The experimental findings support the analytical model that is described in chapters 3.

1. Introduction

Auto breakup processes, a process of spontaneous droplet formation, from terrace based geometries were first published in 1997 by Kawakatsu and co-workers (Kawakatsu et al. 1997) within the group of Nakajima, later followed by (Sugiura et al. 2001). Kobayashi and co-workers extended the work in the application of straight through emulsification devices (Kobayashi et al. 2004) and membrane emulsification with oblong nozzles (Kobayashi et al. 2002). The use of porous tubes generating highly uniform droplets has been attributed to the principle of auto breakup (Hoppe & Melin 2007).

In the regime of auto breakup, the size of the droplet seems mainly determined by the geometry of the fluidic micro-channels. It was observed that the flow rate of the inner fluid could co-determine droplet size. However, the influence of the outer fluid flow seems insignificant on the droplet size. The absence of a drag force of the outer fluid on the droplet formation makes the process of auto breakup different from other emulsification techniques such as used in cross flow and co-flow emulsification (Seemann et al. 2012).

1.1. Micro-channel emulsification: Droplet formation from a terrace

One of the systems in which the flow of the outer fluid plays an insignificant role in droplet formation is by using terrace based micro-channels (figure 1). The inner fluid flows through a small channel onto a rectangular flat terrace. On the terrace the inner fluid forms a disc, which grows and reaches the end of the terrace. Then the inner fluid flows in a deep well forming a spherical droplet, which detaches itself from the bulk on the terrace. Important in this process is that the outer fluid also can access the terrace enabling change of the shape of the inner fluid on the terrace. (Kawakatsu et al. 1997, Sugiura et al. 2001, 2002). If the depth of the well is smaller than the diameter of the to-be-droplet the fluid remains a discoid. (Kobayashi et al. 2006a). A critical step height as function of the width of the channel has been found; below that step height no breakup takes place (Kobayashi et al. 2009).

The fluid dynamic steps during terrace based emulsification are quiet well understood and explained by a geometric model (van der Zwan et al. 2009). A pressure drop is the trigger for breakup. This theory was confirmed by simulations with computational fluid dynamics (CFD) (van Dijke et al. 2008).

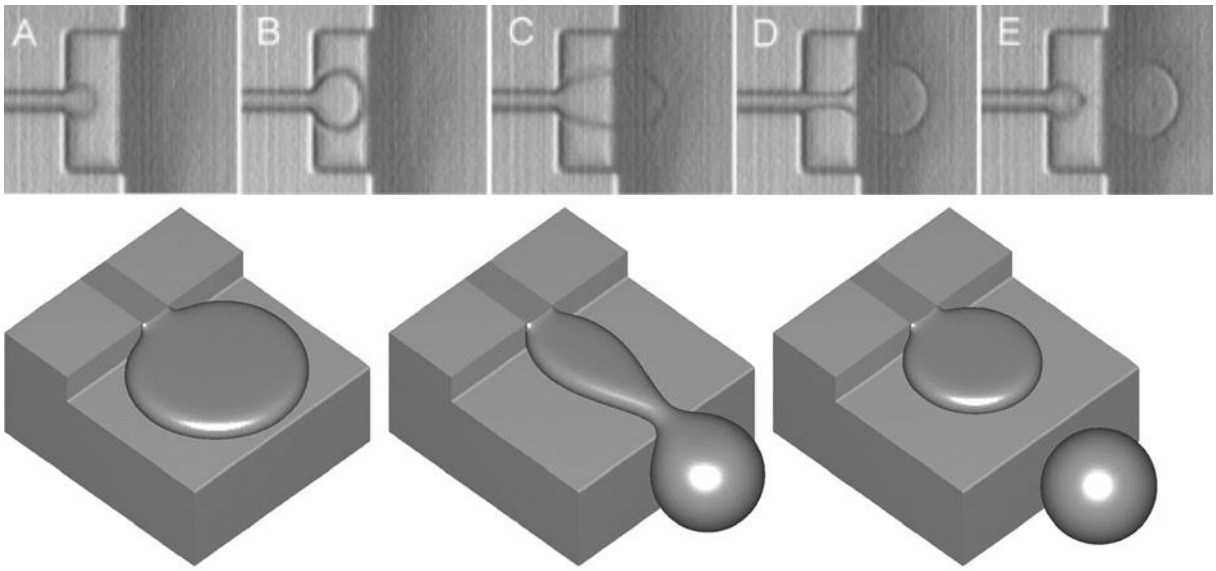

Figure 1. Terrace based droplet formation: microscopy and a schematic images of process of micro-channel emulsification (van der Zwan et al. 2009, van Dijke et al. 2008).

Methods for scaling up this micro-channel system have been proposed, however, there are still limitations in the scalability. Parallelisation by adding up multiple micro-channels to one vessel was successful; however, such a microfluidic system is large, costly and complex (Kobayashi et al. 2010).

A related terrace based auto breakup technique is edge-based droplet generation emulsification (EDGE), and is based on the formation of several uniform sized droplets at the same time from one single terrace with a very large width (van Dijke et al. 2010b). CFD simulations and experimental data show that droplet sizes depend mainly on the height of the channel. Further, a scaling relation was found on the ratio between the viscosity of the inner and outer fluid (van Dijke et al. 2010a).

1.2. Membrane emulsification using oblong pores

In 2D, membranes in which each pore forms a microfluidic channel has high potential for upscaling microfluidics. The terrace based geometry can also be applied in membranes with oblong pores. The cross section of a terrace based micro-channel at the mouth of the terrace is rectangular (oblong). The outer fluid enters the pore via the corners of the oblong pores, during outflow of the inner fluid via the centre of the pores.

(Kobayashi et al. 2002). Only an aspect ratio above 3 between the width and length of the pore would produce monodispersed emulsions (Kobayashi et al. 2004).

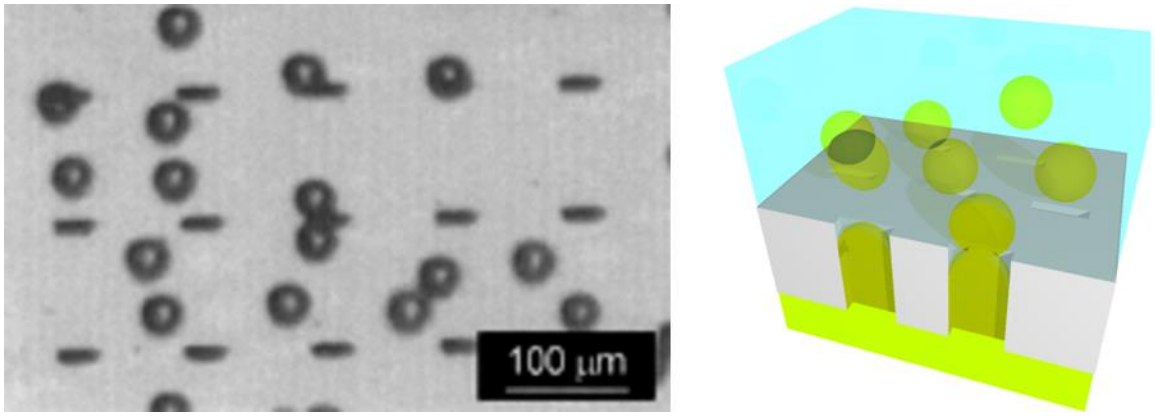

Figure 2. Emulsification from membranes with oblong pores. (left) Microscopic snapshot of emulsification at low flow rate. Highly uniform droplets are formed from the oblong pores (Kobayashi et al. 2002). (right) A schematic image that depicts the formation of oil-in-water droplets from oblong pores.

Scaling up membrane emulsification, using auto breakup pores instead of round pores as used in cross flow emulsification techniques (van Rijn 2004), is of wide interest for industrial applications, especially pharmaceutical applications (www.nanomi.com). The auto breakup technique yields highly concentrated emulsions with droplets uniform in size, and are therefore more stable than polydispersed emulsions (Kobayashi et al. 2008). Also the possibility to generate water-in-oil-in-water double emulsions is feasible when starting from a water-in-oil pre-emulsion (Kobayashi et al. 2005a).
Droplets with uniform sizes have been formed at low flow rates of the inner fluid and with no flow of the outer fluid. This process has been described by computational models in CFD showing breakup inside the channel (Kobayashi et al. 2005b, 2006b). At higher flow rates droplets become very large, because breakup via this spontaneous interfacial tension driven process is then inhibited.

In summary, the principle of auto breakup, a seemingly spontaneous process driven by interfacial tension at low inner flow rates of the inner fluid, has been studied and industrially applied. However, a clear view on the physical mechanism is lacking. In this chapter a description of the phenomenon of auto breakup is given, providing insight in droplet formation, but also on the stability of the confined liquid thread.

2. Materials and methods

2.1. Experimental setup

An inner fluid with viscosity η and equilibrium interfacial tension γ is led through a capillary with radius R_c, which is wetted by an outer fluid at the end of the capillary. The inner fluid forms a growing droplet with radius R_d adhering to the capillary mouth. The formation of droplets was studied by using a module as depicted in figure 3. The dimensions of the rectangular outer fluid chamber are 10 x 10 x 120 mm. Different capillaries with different cross section have been used and made and were typically 50 to 80 mm long to provide a fully developed laminar flow within the capillary. The fluidic module was placed under an optical microscope (Olympus BH2) connected to a Motic MC 2000 camera operating and recording at a rate of about 15 frames per second (fps). The inner fluid was pressed through the capillary by applying pressurized nitrogen on the inner fluid and its overpressure was controlled by a pressure controller (Wallace & Tierman). This pressure control is chosen above a syringe pump, because pressure fluctuations from a syringe pump may induce perturbations and premature breakup (Li et al. 2014). Droplets were carried away by a very mild co-flow of the outer fluid; just to clear the view for new droplet formation, and not to apply a significant drag or shear force on the droplet.

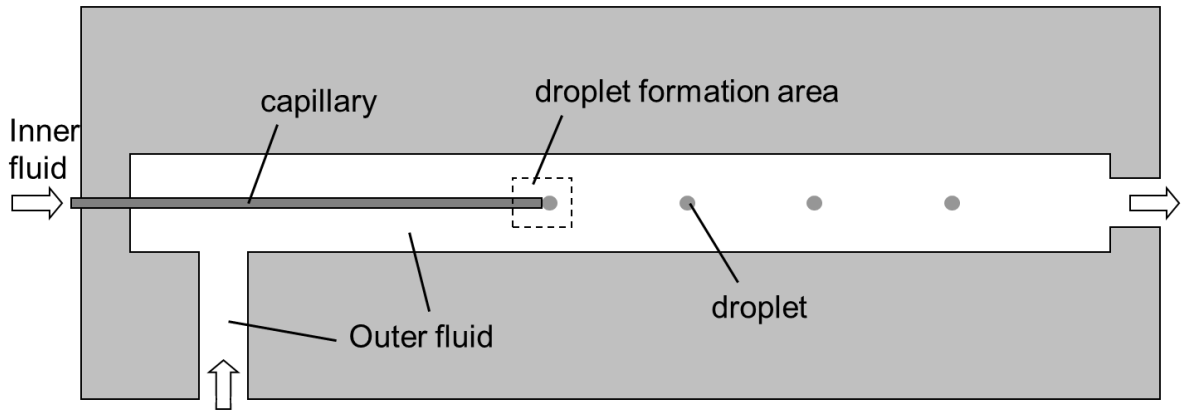

Figure 3. Schematic image of the module used for studying droplet formation.

2.2. Micro-corrugated capillary design and preparation

A micro-corrugated capillary has been made, which allows droplet formation via the mechanism of auto breakup. Nine capillaries of 1.5 mm outer diameter were assembled in a hollow cylindrical glass rod of 6.8 mm outer diameter around its inside wall. The assembly was next heated in a blue flame until the glass started to melt in the middle of the glass rod. The ends of the assembly were pulled away from each other yielding a uniform thin micro-structured capillary with cross sections as depicted in figure 4A. The capillary is based on a cylindrical cross-section in the middle and with nine micro-corrugations aside.

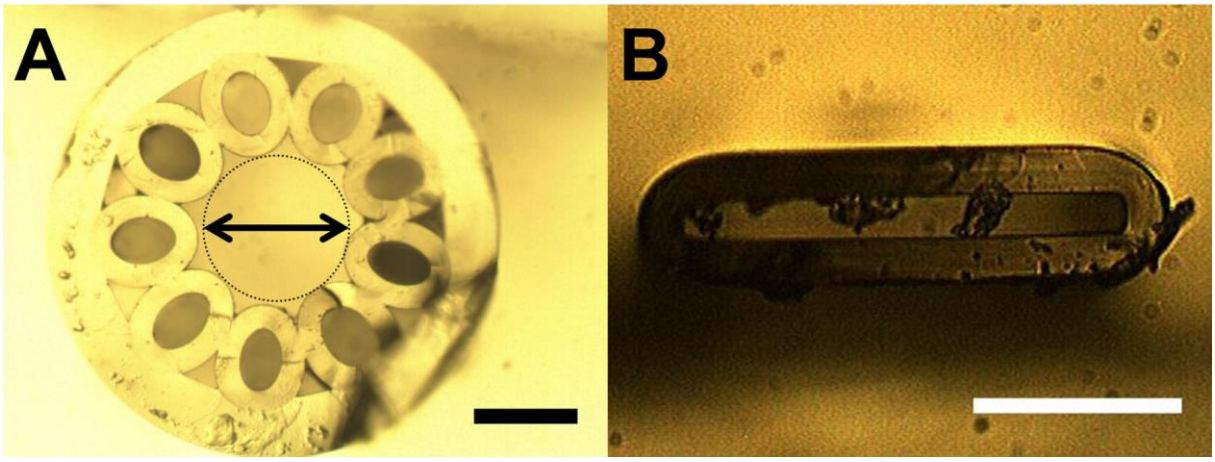

Figure 4. Optical microscopic images of cross sections of capillaries: **A** micro-corrugated and **B** rectangular. The arrow indicates the shortest inner diameter of the micro-corrugated capillary. Scale bars are 100 μm.

The shortest inner radii of the micro-corrugated capillaries (figure 4A) used in the experiments are of 39, 50 and 62 μm. Inner fluid was only allowed in the middle capillary of this micro-structured capillary, because the remaining pores were sealed at the inlet end of the capillary. Rectangular capillaries were purchased from The Technical Glass Company (UK) and have inner cross section of 200 μm by 20 μm.

2.3. Materials

The physical properties of the inner fluids and outer fluids are listed in table 1. The outer fluid was demineralized water containing Tween–20 (Merck) (1 and 5 w/v %) or sodium dodecyl sulphate (SDS) (Fluka) (1 w/v %). Three different inner fluids were used. Filtered natural sunflower oil (AH, η = 62 mPa·s), silicone oil DC 200 fluid 350 Cs

(Dow Corning η = 373 mPa·s), silicone oil AS100 (Fluka; η = 111 mPa·s), and silicone oil; PMX-200 silicone fluid (Sigma Aldrich; η = 5 mPa·s).

Dynamic viscosities were measured using rheometer (Paar Physica MCR 300). Interfacial tensions were measured using the pendant drop method using profile analysis (Sinterface PAT-1). Densities were measured at 20 °C on a balance density meter.

Table 1. Measured values of interfacial tensions and viscosities (at 20 °C).

	Viscosity (mPa·s)	Interfacial tension (mN/m)		
		1% tween20	5% tween20	1% SDS
Sunflower oil	68	4.5	4.0	2.3
Silicone oil 5	5	4.0	3.5	6.0
Silicone oil 100	110	4.0	3.5	10.0
Silicone oil 350	370	5.0	4.5	8.0

The movies and images were analysed by using computer software ImageJ and Matlab. ImageJ was used to process the movies frame by frame. Per frame the outline of the droplet shape was obtained and the coordinates of the pixels in these outlines were recorded. The coordinates were processed by a Matlab script, which calculates values of droplet radii, inner fluid flows and velocities. A more detailed description of how the snapshots in the movies have been processed is described in appendix A.

3. Results and discussion

The auto breakup regime has been studied from experimental observations. Auto breakup is associated with low flow of the inner fluid, fast droplet formation times and small droplet/nozzle diameters ratios. Droplets are formed by an interfacial tension driven breakup process. A capillary has been developed where micro-corrugations provide access of the outer fluid in the capillary flow of the inner fluid. Spontaneous droplet formation is demonstrated to be possible experimentally and has been observed from rectangular capillaries and micro-corrugated capillaries.

3.1. Auto breakup from a rectangular capillary

Droplets are formed spontaneously from a nozzle with a rectangular cross-section as has been observed by using a rectangular capillary (see cross section in figure 4B). In figure 5, the confined rectangular liquid thread narrows towards the capillary mouth. The liquid thread finally breaks close to the droplet, which contributes to an emulsion of droplets which are all very uniform in size. The covariance of variation (CV) of the droplet sizes is below 2%, which is smaller or comparable than from membranes with oblong pores.

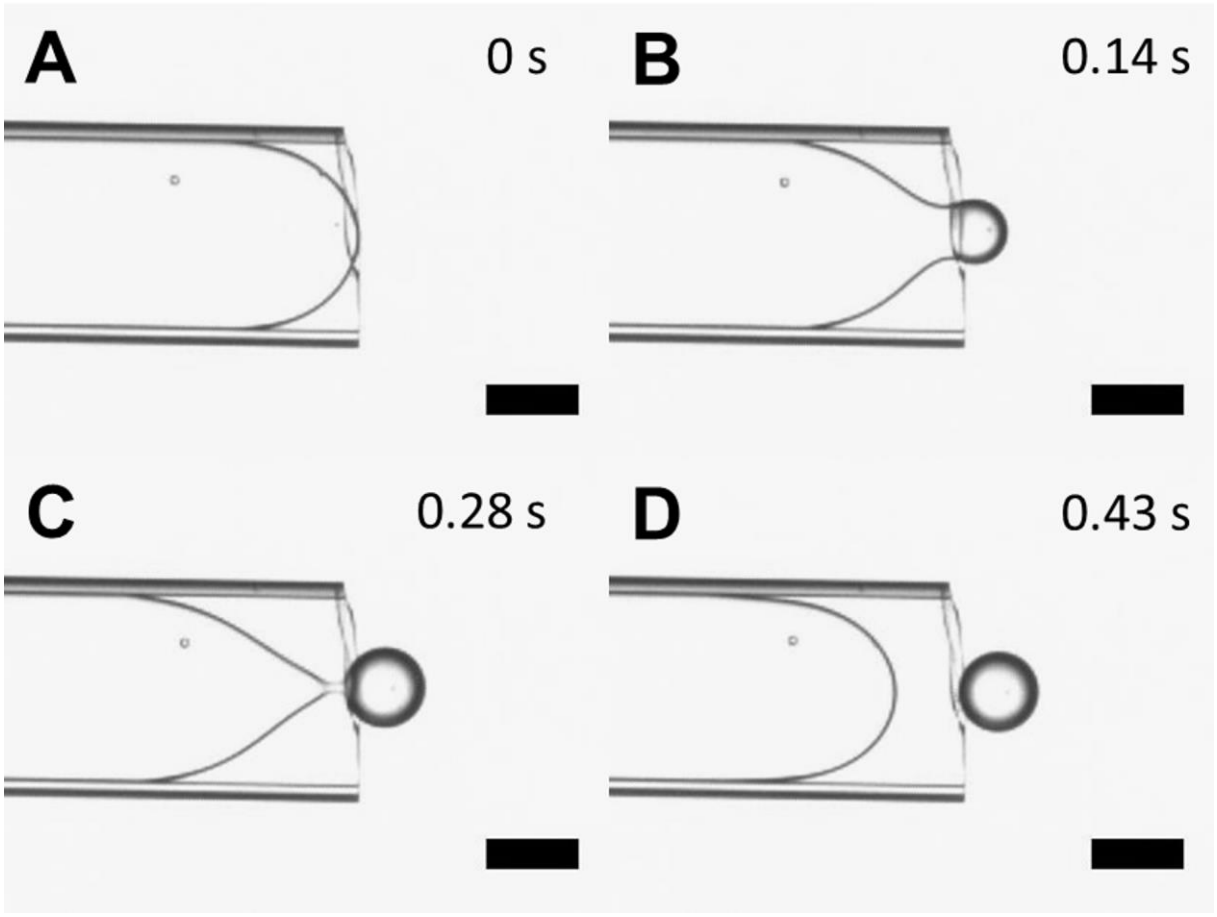

Figure 5. Optical microscopy snapshots sequence of a droplet formed from a rectangular capillary. Sunflower oil is emulsified in 1% SDS aqueous solution at $1.19 \cdot 10^{-4}$ µL/s. **A** The inner fluid flows to the capillary mouth. **B** A droplet is formed and grows, while **C** the thread radius decreases until **D** the droplet snaps off from the bulk fluid with a fast necking process. Scale bars are 100 µm.

First stage of droplet formation is when the inner fluid flows to the end of the capillary (figure 5A). A convex shaped interface (the interface between the inner fluid and outer fluid inside the capillary) is formed and next when the interface reaches the exit (cf. deep well in auto breakup) of the capillary a droplet is formed and grows still attached to the inner fluid from the capillary (figure 5B-C). A cylindrical neck is formed with the same diameter as the capillary height (figure 5C) and collapses. The droplet radii R_d are more than twice the height of the capillary at low flow rates of the inner fluid (figure 6). Above a critical flow rate the confined liquid thread remains intact and the droplet grows towards infinite large. Observed droplet sizes relative to the nozzle height and the existence of a critical flow rate behaved similar as in droplet formation techniques using membranes with oblong pores (Kobayashi et al. 2002).

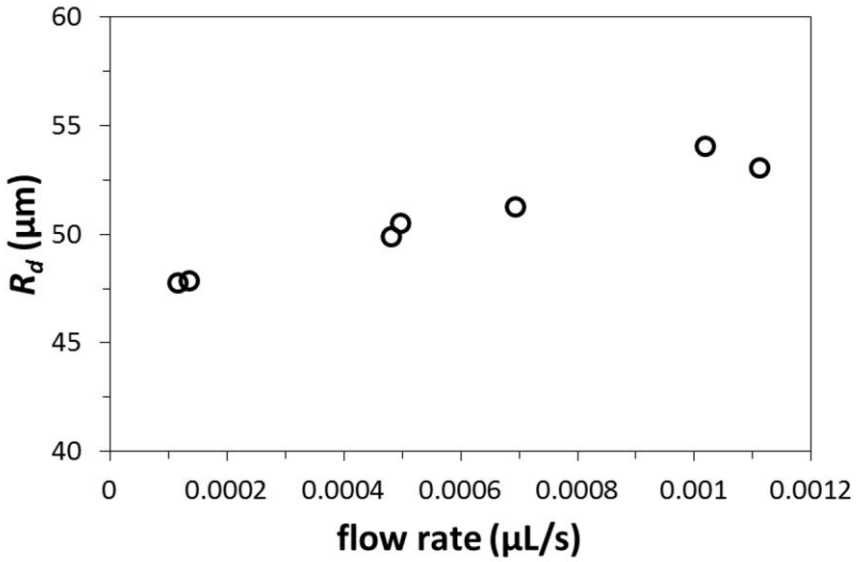

Figure 6. Graphs showing radii of droplets R_d formed by different flow rates of the inner fluid (sunflower oil). Above $1.2 \cdot 10^{-3}$ µL/s droplets grows towards infinite R_d sizes.

3.2. Auto breakup from a micro-corrugated capillary

A droplet is formed at the mouth of a micro-corrugated capillary that is connected to the cylindrical shaped confined inner fluid thread inside the capillary (figure 7A). The micro-corrugations (figure 4A) provide space for the outer fluid to enter the capillary while the centre of the capillary is filled with inner fluid. The gap, between the source of inner fluid and the droplet that is formed during the auto breakup process, can be filled by outer fluid.

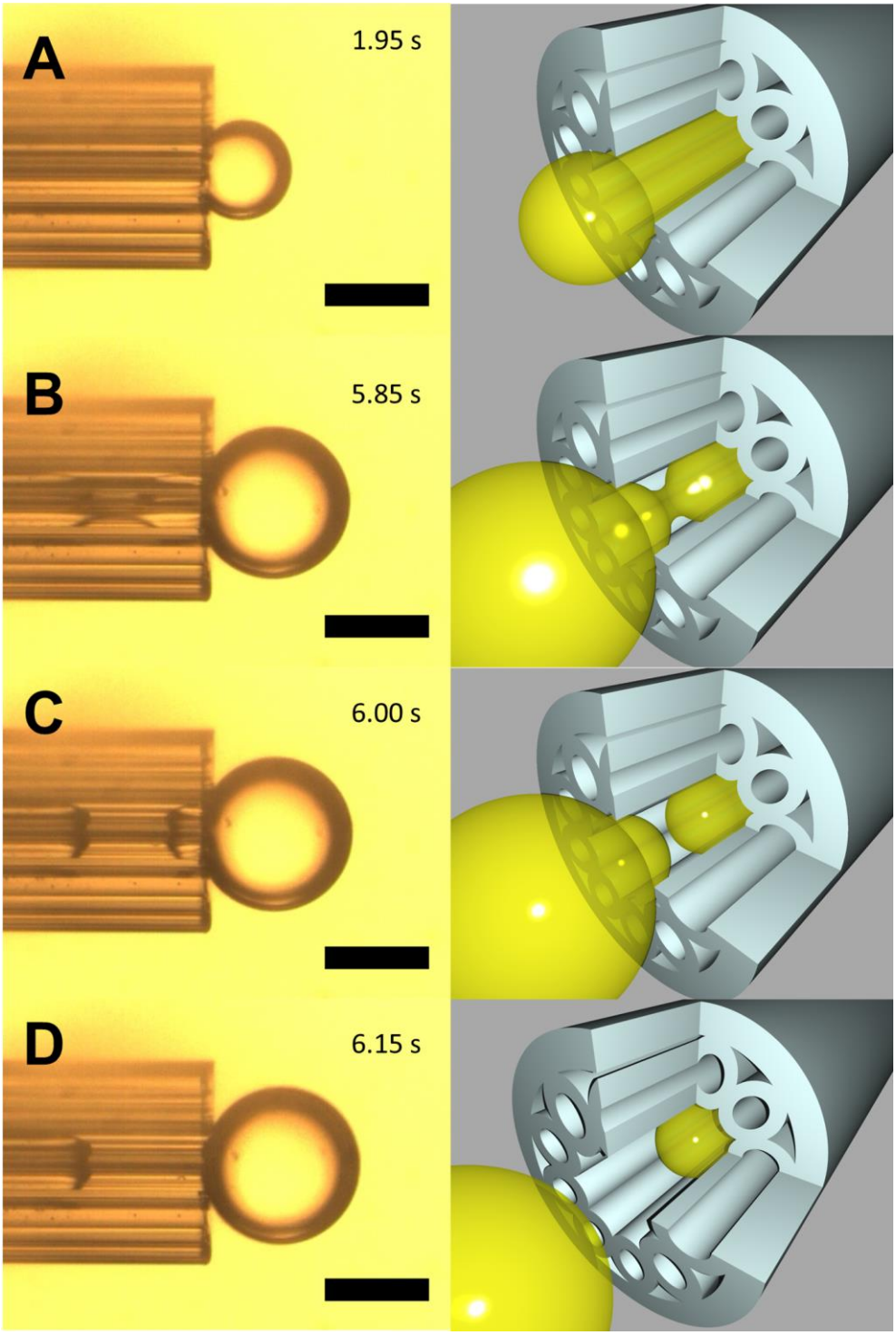

Figure 7. Image sequences showing droplet formation by auto breakup. Optical microscopy snapshots (left) and corresponding schematic images (right) from top to bottom four stages of droplet formation; **A** starting from initial droplet, **B** followed by necking process inside the capillary, and **C** detachment from the inner fluid thread. **D** The remaining liquid flows in the droplet. Scale bars are 100 μm.

The cylindrical shape of the confined liquid thread inside the capillary becomes unstable when the radius of the droplet increases beyond twice the radius of the capillary (figure 7B). Inside the capillary, an indentation of the confined liquid thread starts when the radius of the droplet is twice as large as the inner radius of the capillary. The indentation or necking of the confined liquid thread is enlarged quickly until breakup (figure 7C). Inside the capillary, the remaining fluid that is still connected to the droplet flows into the droplet and the final droplet detaches from the capillary mouth (figure 7D).
The breakup of the inner fluid occurs inside the capillary close to the mouth of the capillary. The gap caused by the necking process is replaced by outer fluid that passively flows inwards via the micro-corrugations at the exit of the capillary. However at higher flow rates of the inner fluid the liquid thread is stabilised and hampers the necking and breakup process.

In figure 8 the radii of the droplets R_d are shown for different flow rates of the inner fluid and R_d was normalised by the radius of the capillary R_c since different capillary sizes have been used in the experiments. The R_d of the droplets are about twice the radius of the inner capillary R_c at low flow rates. Within the regime of auto breakup, R_d increase slightly at increasing flow rates.

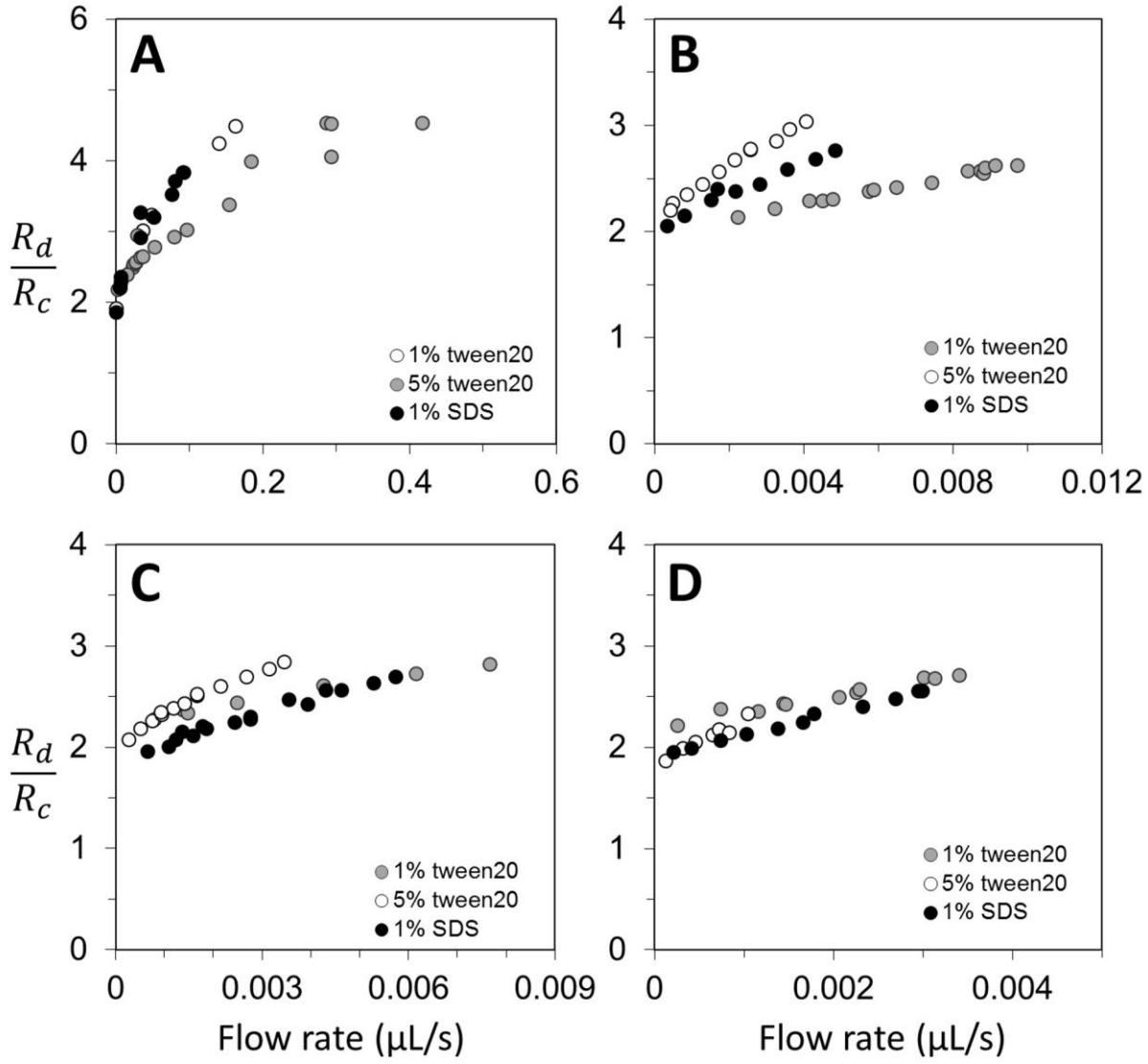

Figure 8. The size of the droplet as function of inner fluid flow rate with inner fluids: **A** silicone oil 5, **B** sunflower oil, **C** silicone oil 100 and **D** silicone oil 350. Outer fluids are marked by: (white) 1% (wt) tween20, (grey) 5% (wt) tween20 and (black) 1% SDS Tween20.

The dependence of the droplet size on the inner fluid viscosity and surface tension is shown in figure 8. The viscosity increases from figure 8A-D. The flow rates at which auto breakup is possible are larger at low viscosity and can be explained by the shear in the viscous flow. A certain amount of shear is needed to resist breakup inside the capillary and with higher viscosity this shear is reached at a lower flow rate than with lower viscosities.

Another effect is the difference at which droplet sizes R_d/R_c increase at increasing flow rate. In figure 8A, using a low inner fluid viscosity, the droplet sizes increase fast, which is not similar to results from literature for emulsification by membranes with oblong pores, terrace based emulsification and experimental use of higher inner fluid viscosities (figure 8B-D). The deviating upward trend from the plot of figure 8A with respect to 8B-8D may be explained by the fluidic, physical and/or chemical properties of working with silicone oil 5. The flow velocity through the nozzle is up to 100 times higher than for the other inner fluids with higher viscosities (up to 75 times). The inner fluid velocity through the capillary is higher, which means that possibly more inner fluid is added to droplet during the time needed to breakup. Furthermore, silicone oil 5 may wet the capillary wall more effectively than the other inner fluids, because the silicone oil is slightly more hydrophilic. The wetting of the inner capillary by the oil will hamper the breakup process.

Sometimes satellite droplets have been formed at low inner fluid velocities between the droplet and inner fluid inside the capillary, especially when working with a high viscous silicone oil (370 mPa·s) (figure 9).

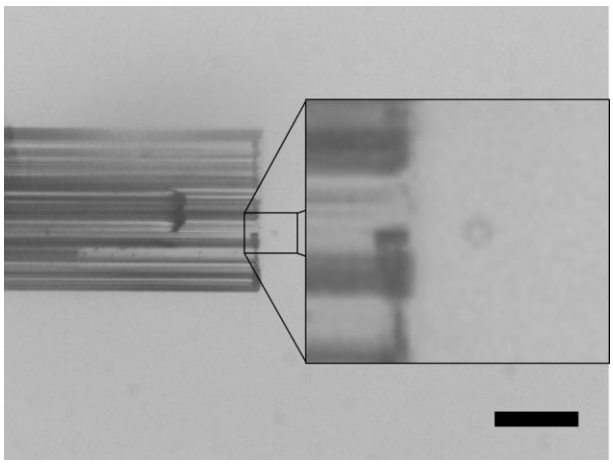

Figure 9. Snapshot of a satellite droplet (from the same movie as in figure 7). Diameter of the satellite droplet is 16 µm. Scale bar 200 µm.

This phenomenon can be explained by the collapse of the liquid thread at the final stage of breakup. The two half spheres that are formed when the liquid thread breaks at low velocities form a relatively long micro-thread, which can reshape into a small satellite droplet.

3.3. The stability of a confined liquid thread inside the capillary by increasing and decreasing the flow rate of the inner fluid

Auto breakup at low flow rates

At low flow rates it was found that uniform droplets can be made for all oils small. The flow rate and size of the droplet during several cycles of droplet formation is depicted in figure 10 as a typical example.

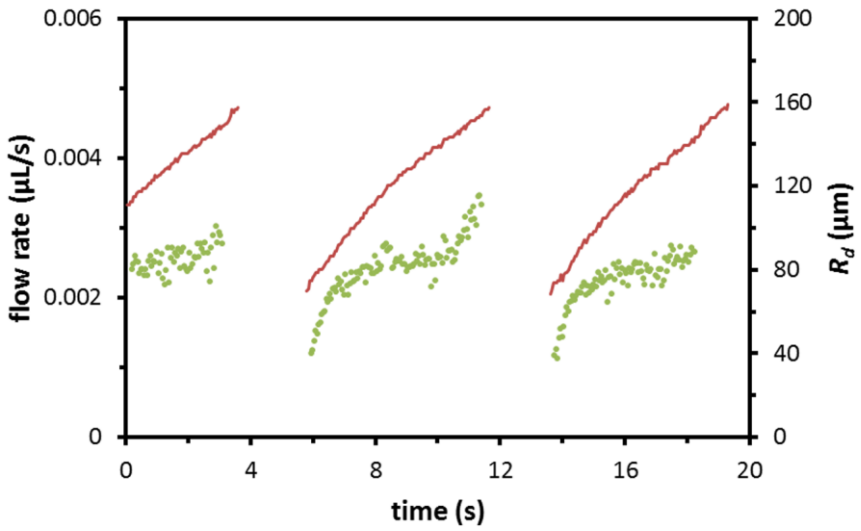

Figure 10. Graph showing auto breakup cycles during 20 seconds and the formation of three droplets with R_d of 160 µm.

Auto breakup at low flow rates followed by a high flow rate

The auto breakup process can be hampered by substantially increasing the flow rate as seen in figure 11. Up to 26 seconds droplets are formed via the auto breakup mechanism while the flow rate of the inner fluid increases slightly. After 26 seconds a new droplet is formed which grows without breakup. The experiment shows that a confined liquid thread remains stable when the flow rate increases.

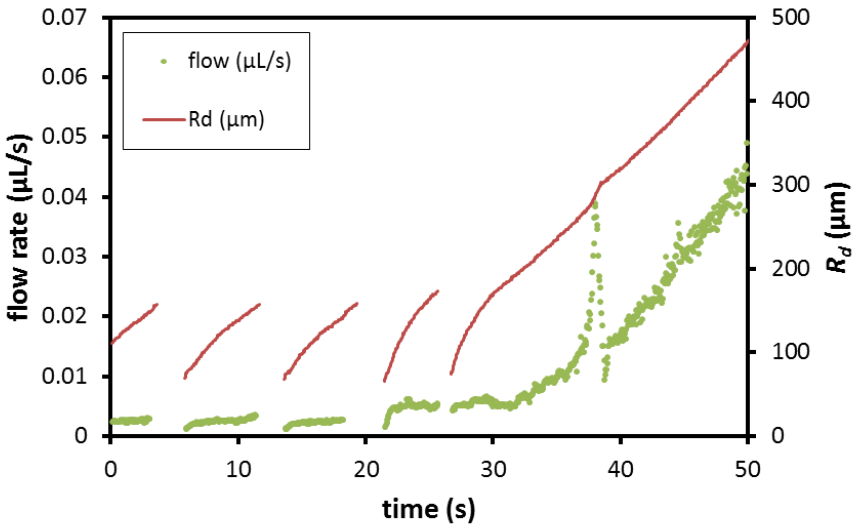

Figure 11. Graphs showing the hampering of the auto breakup process when the flow rate increases to higher than about 0.005 µL/s. After 26 seconds the droplet grows towards infinitely large.

Auto breakup at a critical flow rate

The breakup of the confined liquid thread inside a capillary is severely hampered if the flow of the inner fluid has reached a critical value. Inside the capillary a small stable necking of the liquid thread is observed (figure 12). The collapsed liquid thread (or neck) remains remarkably stable when the droplet grows at a constant flow rate.

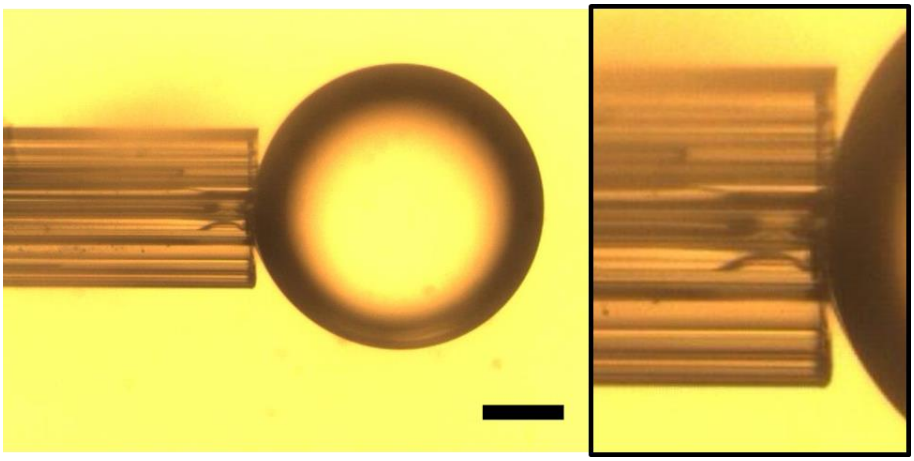

Figure 12. (left) Optical microscopy image shows a droplet that is connected via a neck to the confined liquid thread inside a corrugated capillary. (right) Detail of the left image. Scale bar in the left image is 200 µm.

The smallest radius of the stable neck of the collapsed liquid thread, however, seems to be larger at higher flow rates.

The stable neck of the collapsed liquid thread may be destabilised by decreasing the flow rate as is visualised in figure 13. First a large droplet is formed above the auto breakup regime at a high flow rate and next the flow rate is decreased. At 10.5 s when the flow rate has decreased to a value of about 0.006 µL/s the liquid thread collapses completely and a new droplet starts to grow. The process was repeated by decreasing the flow rate from 20 s steadily to breakup of the liquid neck at 36.5 s again at a flow rate of about 0.006 µL/s.

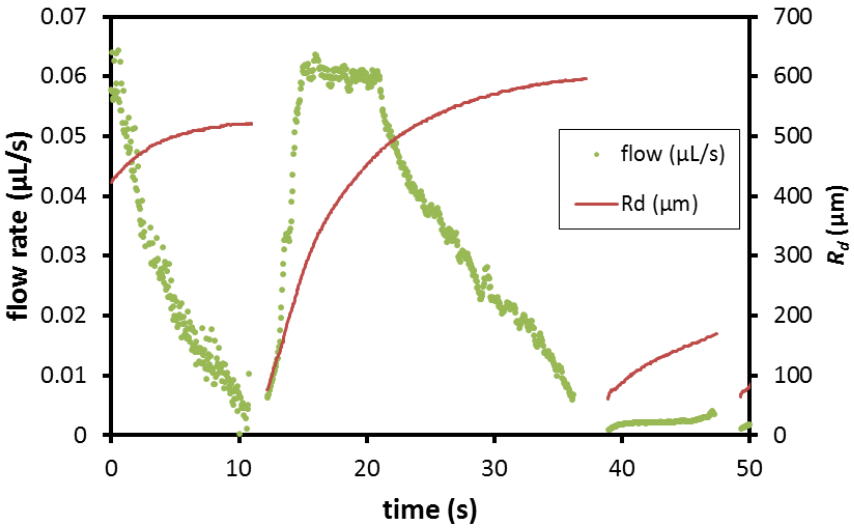

Figure 13. Graphs showing that a confined liquid thread has a complete breakup when the flow rate decreases below a critical value.

4. Conclusions

The phenomenon of auto breakup, a seemingly spontaneous instability of a confined liquid thread inside the capillary, was studied by optical microscopy. It was shown that it is possible to produce uniform sized droplets by auto breakup using a round micro-corrugated and a rectangular glass capillary, provided that the outer fluid is able to enter the capillary during droplet formation. The auto breakup instability of the confined liquid thread inside the capillary can be resisted by increasing the velocity/flow rate of the inner fluid above a critical value. Above this critical value a remarkable stability of the confined liquid thread inside the capillary was observed leading to infinitely large growing droplets.

Chapter 3

Auto breakup: Analytical model for droplet formation at low velocities

Abstract

An analytical model is introduced to describe the phenomenon of auto breakup. Droplets are formed by spontaneous breakup of a confined liquid thread flowing at a low velocity inside a microfluidic channel as long as the outer fluid is allowed to enter the channel. The analytical model accurately describes experimental observations, that auto breakup happens as long as the capillary number (Ca) is below a critical capillary number (Ca_{cr}) of 0.0625 (=1/16). Around Ca_{cr} the liquid thread collapses and a stable neck inside the microfluidic channel is observed. Above Ca_{cr} droplets grow towards infinitely large.

1. Auto breakup

The phenomenon of spontaneous breakup inside a microfluidic channel, here observed inside a micro-corrugated glass capillary, is depicted in figure 1.

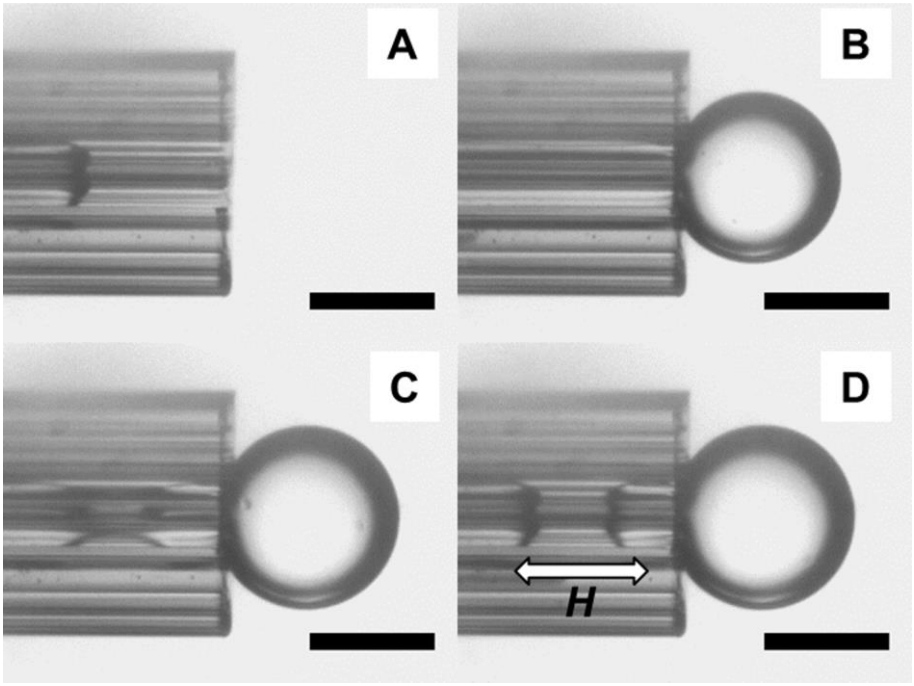

Figure 1. A sequence of optical microscopy snapshots shows the formation of a droplet. **A** An inner fluid is led through the capillary and the front forms a spherical shape. **B** A droplet is initially formed at the capillary mouth. **C** The outer fluid partially replaces the inner fluid via flow through the corrugated wall of the capillary. **D** The fluid cylinder inside the capillary has collapsed. Scale bars are 200 μm.

A micro-corrugated capillary is placed in a reservoir with outer fluid. The inner fluid is pressed through the capillary. Inside the capillary the inner fluid is capped with a half sphere (figure 1A). When the fluid reaches the mouth of the capillary the half sphere grows to a droplet (figure 1B). The inner fluid inside the capillary starts an indentation when the radius of the droplet is about twice the inner radius of the capillary (figure 1C). The indentation is amplified and the inner fluid breaks. Two half spheres are formed after breakup and the part of inner fluid attached to the droplet flows in the droplet (figure 1D). Then the droplet is carried away from the capillary mouth by a mild co-flow and a new cycle of droplet formation can start.

1.1. Analytical model for describing auto breakup

In the model presented here is postulated that the breakup process of the liquid thread, including droplet snap-off driven by interfacial tension force inside the capillary, will take place when two criteria are fulfilled:

1. Energy criterion: During the breakup process the total thermodynamic Gibbs energy change in the system ($\Delta G = \gamma \Delta A + p \Delta V$) should be negative. The term $p\Delta V$ is zero, because inner and outer fluids are considered Newtonian and, therefore, incompressible. Interfacial tension γ is assumed to be a constant. Therefore the total interfacial area between inner and outer fluid ΔA should decrease.

2. Pressure criterion: If the pressure in the droplet and near the mouth of the capillary becomes lower than the Laplace pressure of the inner fluid cylinder, the inner fluid will no longer be pressed against the wall of the capillary, and the process of breakup starts. The necessary pressure drop inside the capillary is induced by the growth of the droplet. Since the Laplace pressure decreases with increasing droplet radius, also the pressure of the inner fluid near the capillary mouth decreases.

Energy criterion

In the breakup process of the liquid thread inside the capillary, a cylinder of inner fluid with length H (see figure 1D) and interfacial area $2\pi R_c H$ is assumed to be removed, while two half-spheres with area $2\pi R_c^2$ each are created (see figure 1D). Radius of the cylinder is R_c. The reduction in interfacial area ΔA_c in the capillary before and after breakup is therefore:

$$\Delta A_c = 4\pi R_c^2 - 2\pi R_c H \tag{1}$$

The displaced inner fluid is taken up by the external droplet, which will therefore increase in volume and interfacial area, with ΔA_d. Therefore, the total amount of interfacial area lost is ΔA.

$$\Delta A = \Delta A_c + \Delta A_d = 4\pi R_c^2 - 2\pi R_c H + \Delta A_d \leq 0 \tag{2}$$

The increase in volume of the droplet ΔV_d is:

$$\Delta V_d = \pi R_c^2 H - \frac{4}{3}\pi R_c^3 \tag{3}$$

Pressure criterion

The Laplace pressure inside the droplet p_d compared with that of the surrounding outer fluid p_0 is:

$$p_d - p_0 = \frac{2\gamma}{R_d} \tag{4}$$

The pressure profile of the inner fluid along the capillary depends both on the flow velocity v_d through the capillary and on the Laplace pressure (equation (4)) of the droplet at the end of the capillary. At a distance z from the mouth of the capillary inwards, the pressure p_z inside the capillary at this place is given by a general flow/pressure relation:

$$p_z - p_0 = \frac{8\eta z v_d}{R_c^2} + \frac{2\gamma}{R_d} \tag{5}$$

The first term on the right is the contribution by Hagen-Poiseuille flow through the capillary, with η is the viscosity of the inner fluid. The second term is the Laplace pressure of the droplet as determined by equation (4).

As long as p_z - p_0 is larger than the Laplace pressure of the confined liquid thread inside the capillary (γ/R_c), the liquid thread will be stable, but as soon as it becomes smaller, the liquid thread will start to collapse by outflow of the inner fluid into the droplet. Breakup is initiated when:

$$p_H - p_0 = \frac{\gamma}{R_c} \tag{6}$$

Combining equations (5 and 6) yields a relation between R_d and R_c at the onset of breakup:

$$\frac{R_d}{R_c} = 2\frac{Ca_{cr}}{Ca_{cr} - Ca} \tag{7}$$

with Ca is the capillary number

$$Ca \equiv \frac{\eta v_d}{\gamma} \tag{8}$$

and Ca_{cr} is a critical capillary number

$$Ca_{cr} \equiv \frac{1}{8}\frac{R_c}{H} \tag{9}$$

Radius of the droplet R_d becomes infinitely large as soon as Ca reaches the value of Ca_{cr}.

Equation (7) has been derived with the pressure criterion and assuming a viscous pressure drop inside the capillary.

This result is combined with the energy criterion: equations (equation (2) and (3)). The droplet radius at the onset of breakup is denoted as R_{d0} and the final droplet size after breakup as R_{d1}. The final droplet volume V_{d1} can then be found by equation (10).

$$V_{d1} = \frac{4}{3}\pi R_{d1}^3 = \frac{4}{3}\pi R_{d0}^3 + \pi R_c^2\left(H - \frac{4}{3}R_c\right) \tag{10}$$

The radius of the final droplet R_{d1} after breakup can be expressed by using equation (7) for R_{d0}.

$$\frac{4}{3}\pi R_{d1}^3 = \frac{4}{3}\pi\left[2R_c\left(\frac{Ca_{cr}}{Ca_{cr}-Ca}\right)\right]^3 + \pi R_c^2\left(H - \frac{4}{3}R_c\right) \tag{11}$$

Bringing R_{d1}/R_c to the left side of the equation becomes

$$\frac{R_{d1}}{R_c} = \left(\frac{3}{4}\frac{H}{R_c} + 8\left(\frac{Ca_{cr}}{Ca_{cr}-Ca}\right)^3 - 1\right)^{1/3} \tag{12}$$

The increment of the surface area of the droplet can be calculated from the outflow of the inner fluid:

$$\Delta A_d = 4\pi R_c^2\left[\left(\frac{3}{4}\frac{H}{R_c} + 8\left(\frac{Ca_{cr}}{Ca_{cr}-Ca}\right)^3 - 1\right)^{2/3} - 4\left(\frac{Ca_{cr}}{Ca_{cr}-Ca}\right)^2\right] \tag{13}$$

Finally an implicit relation for H is obtained by combining this result with equation (2) and setting the difference in interfacial area ΔA to be zero. Breakup starts as soon as both energy and pressure criteria are fulfilled:

$$\frac{H}{R_c} = 4\left[1 + \left(\frac{3}{4}\frac{H}{R_c} + 8\left(\frac{Ca_{cr}}{Ca_{cr}-Ca}\right)^3 - 1\right)^{2/3} - 4\left(\frac{Ca_{cr}}{Ca_{cr}-Ca}\right)^2\right] \tag{14}$$

H is fully determined by equation (14). The other parameters in equation (14) are all known physical parameters: γ, η, v_d (via Ca) and R_c.

Plots of equations (12) and (14) are shown in figure 2. Breakup point H is found to be mildly dependent on Ca. At very low inner fluid velocity (or Ca goes towards 0) H/R_c is then 2.641. At higher velocity (or for Ca goes towards the Ca_{cr}) H/R_c is 2. Now Ca_{cr} can be calculated from equation (9) and is 1/16 =0.0625.

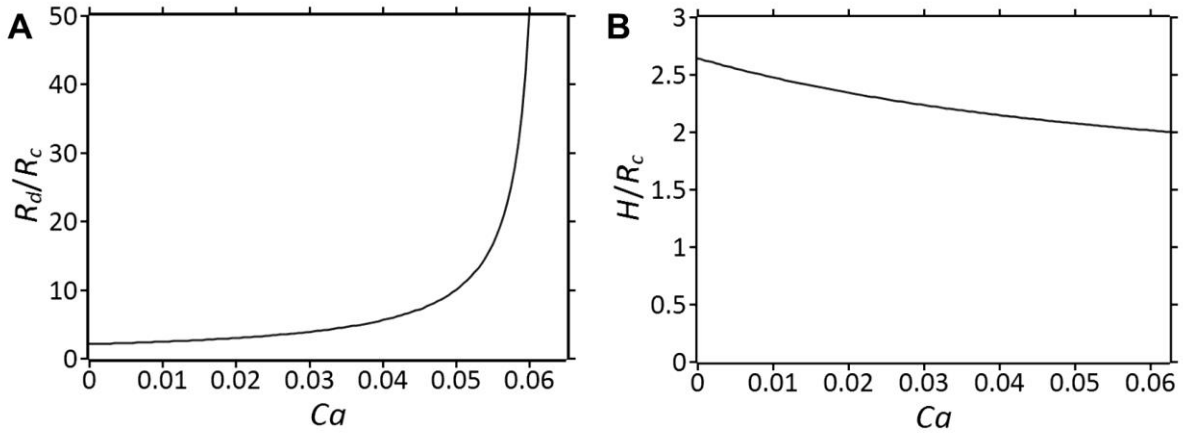

Figure 2. Graphs plotting **A** radius of the droplet R_{d1} normalised by R_c as function of Ca according to equations (12) and **B** the breakup point H normalised by R_c as function of Ca according to equation (14).

1.2. Implicit limitations of the analytical model

The model assumes that a number of possible physical effects that limit the scope of the auto breakup model are negligible, provided the system set-up and boundary conditions are well chosen. In this section the following physical effects are considered: gravity acting on the droplet, drag force by a flow of the outer fluid exerted on the forming droplet, wetting of the wall/corrugations inside the capillary that hamper breakup, slipping flow of the inner fluid inside the capillary, and pressure changes that may influence premature (auto) breakup.

1.2.1. Buoyancy force acting on the droplet

Buoyancy acts on a body by gravitational force and goes linear by density difference and cubic with droplet radius. The effect of buoyancy is formulated in equation (15):

$$F_b = \Delta\rho \frac{4}{3}\pi g R_d^3 \tag{15}$$

Here, g is gravitational acceleration (9.81 m/s^2) and $\Delta\rho$ the density difference of outer and inner fluid, here $\Delta\rho$ = 30-100 kg/m^3 for the viscous oils dispersed in aqueous solutions that are used.

The interfacial tension force F_{st}, the force which keeps the droplet attached to the inner fluid thread (van Rijn 2004):

$$F_{st} = 2\pi R_{thread}\gamma \tag{16}$$

Interfacial tension force F_{st} is 1 - 3 µN at a radius of the liquid thread R_{thread} = 50 µm and γ is 3 – 10 mN/m (table 1 in chapter 2).

The interfacial tension force is much larger than the buoyancy force (equation (15)) that pulls it away by gravity. Droplets formed by auto breakup in our experiments have about 100 µm radius. When choosing $\Delta\rho$ is 30 – 80 kg/m^3, the buoyancy force on the droplet is $F_b \sim 1 - 3$ nN and is a factor thousand lower than F_{st}. Therefore buoyancy force F_b plays no significant role in spontaneous breakup droplet formation unless the droplet becomes 5 – 10 times larger in diameter.

1.2.2. Drag force by mild co-flow of the outer fluid

Flow of outer fluid is very mild and used for clearing the view for next droplet formation. Drag force F_{drag} acting on the droplet is neglected as calculated from the linear Stokes equation (17):

$$F_{drag} = 6\pi\eta\bar{v}R_d \tag{17}$$

The radius of the droplet R_d is about 100 µm (neglecting the shade of the capillary) and the average velocity $\bar{v}$ of the outer fluid flow is typical < 2 mm/s. The drag force is ~ 4

nN and thus significant smaller than the interfacial tension force of ~ 1 μN, which keeps the droplet attached to the capillary.

1.2.3. Wetting of the wall inside the capillary by the inner fluid

The effect of wetting of the inside glass wall by the inner fluid is important, because complete wetting would mean that the corrugations of the capillary will also be filled with inner fluid. This would inhibit the auto breakup process. It is rather difficult to estimate the contribution of this effect on the auto breakup process in case of non-complete wetting. Wetting can be taken into account by using a wetting contact angle of the inner fluid with the inner wall of the microfluidic channel. Contact angles of the inner fluid with the walls in terrace based emulsification have been fitted to 30° (van Dijke et al. 2008). In our system the area of contact between the capillary wall is minimized and the inner fluid by using micro-corrugations; the inner fluid inside the capillary is forming a cylindrical liquid thread. Only a small part of the interfacial area of the liquid thread is in contact with the glass wall and mostly with the outer fluid inside the capillary. Optimizing the inner geometry of the microfluidic channel to decrease the contact area of the inner fluid with the inner wall will enable the auto breakup process to be even more effective. Also the breakup process will then happen faster, with that preventing too much inflow in the forming droplet during the breakup process.

The use of surfactants is also a method to prevent the inner fluid from wetting the inner capillary wall. However the lowering of the interfacial tension between the inner and outer fluid will reduce the critical velocity. Also the emulsion that is made will contain these surfactants.

1.2.4. Slipping flow at the inner capillary wall

The fluid velocity near a rigid surface is most often very close to zero due to a good wetting of the fluid with the rigid surface. However for auto breakup a non-wetting surface is strongly preferred. Due to these non-wetting conditions a so-called slipping flow may occur when the inner fluid is interacting less tightly with the wall of the capillary. The velocity at the wall surface is not zero in the slipping flow regime.

In equation (5), a parabolic viscous flow profile (according to Hagen-Poiseuille's law) is assumed and the effect of slip on the auto breakup process according to our model is explored. Slip may be expressed quantitatively in slip length. This slip length λ relates the velocity at the surface v_s with its shear rate. This relation can be found in equation (18):

$$v - v_s = \lambda \frac{\partial v}{\partial r} \tag{18}$$

With r is the radius normal to the capillary wall, and v is the velocity in the inner fluid at r. A physical meaning of slip length is the virtual extension of the surface wall at which the no-slip condition would be satisfied. So, at a slip length further away from the centre of the tube the velocity would have been zero (Lauga & Stone 2003).

In our system of a micro-corrugated capillary, only a part of the inner capillary is in contact with the confined inner liquid thread. An average or effective slip length λ_{eff} can be calculated (Lauga & Stone 2003).

$$\frac{\lambda_{eff}}{R} = \frac{k}{\pi} \ln\left(\frac{1}{cos\left(\delta \, {}^{\pi}/_{2}\right)}\right) \tag{19}$$

With λ_{eff} the effective slip length, R the radius of the capillary (R = 39, 47, 62 µm), k the ratio of the periodicity of the longitudinal corrugations and δ is the fraction of slip area within a period. Our micro-corrugated capillaries consist of nine periodic structures: $k = \frac{2\pi}{9} \approx 0.70$. To calculate the λ_{eff}, δ is assumed to be 0.1 to 0.5.

The graph (figure 3) shows that with increasing slip conditions the overall effective slip length increases.

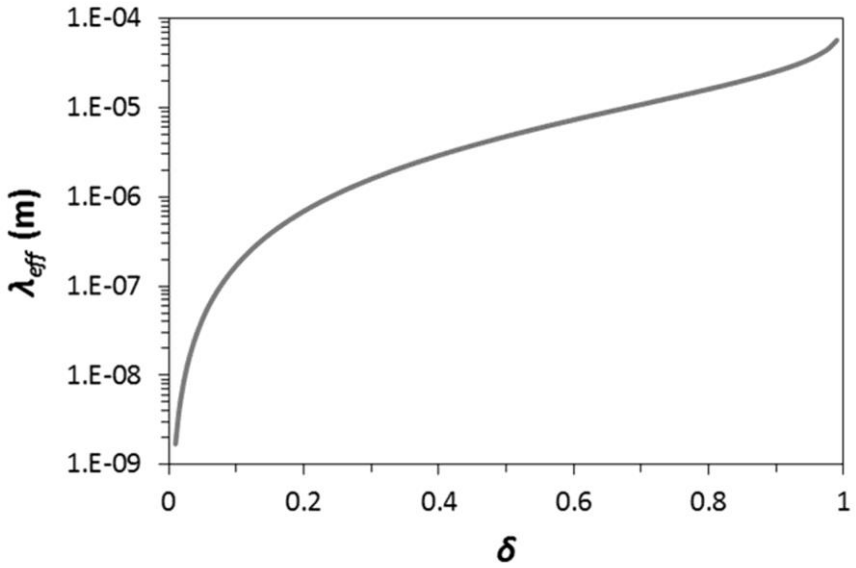

Figure 3. Graph showing the effective slip length λ_{eff} as function of slip fraction δ from equation (19) for R is 62 µm. Note that the y-axis scale is logarithmic.

Velocities at the surface v_s can be derived from the Hagen-Poiseuille law for viscous flow (equation 20) from flow Φ and effective slip length λ_{eff}.

$$v_s = \frac{2}{\pi}\Phi\frac{\lambda_{eff}^2}{\left(R+\lambda_{eff}\right)^4} \tag{20}$$

The velocity at the surface v_s is related to the flux Φ. Equation (20) is only valid at small surface velocities. The velocity at the surface wall v_s increases linear with the average velocity following from equation (18).

Derived slip velocities in our case are in the order of nm/s up to several µm/s for different δ values. Slip lengths are then calculated to be 100 nm up to 5 µm and are independent of the inner fluid velocity as shown in table 2. The velocity at the surface v_s are a factor hundred to ten thousands smaller than the average velocity v_d of the inner fluid derived from Φ. Therefore, neglecting slipping flow and thus effects of wetting are assumed to be valid.

Table 2. Calculated effective slip lengths λ_{eff} and velocities at the surface v_s at a δ of 0.1 and 0.5 and R_c of 62 µm.

	Average velocity	Slip length and surface velocity at δ = 0.1		Slip length and surface velocity at δ = 0.5	
	v_d (mm/s)	λ_{eff} (µm)	v_s (nm/s)	λ_{eff} (µm)	v_s (µm/s)
Sunflower oil (68 mPa·s)	0.73	0.17	10.9	4.8	5.55
Silicone oil (110 mPa·s)	0.63	0.17	9.4	4.8	6.42
Silicone oil (370 mPa·s)	0.28	0.17	4.2	4.8	2.48

1.2.5. Change of internal and applied pressure during breakup

The internal pressure between the place of breakup and the droplet may change during the breakup process, due to the forming of a neck in the liquid thread at the breakup point. The pressure in this liquid thread may increase when its radius becomes smaller and may keep the neck open for some longer time. If the velocity inside the neck exceeds a specific value, possibly related to the capillary number Ca of the inner fluid and becomes bigger than Ca_{cr} during the breakup process then the liquid neck may remain open and stable for an unknown time. Additional volume of inner fluid will then be added to the droplet during breakup and can lead to larger droplets than predicted by the new analytical model. It will be clear that this effect will be most present when the system is operating around the critical capillary number (or critical velocity). The Ca range between 0.04 and 0.06 also very large droplets and also small droplets were observed to be formed that can possibly be related to collapsing liquid thread phenomena. This effect can possibly explain our findings that no good droplet size was found in the Ca range between 0.04 and 0.06, therefore we omitted these data (see figure 5).

On the other hand it may happen that a sudden change in applied pressure may promote premature auto breakup and this will lead to smaller droplets than predicted by the model. A good pump guarantying a constant pressure is a sufficient means to overcome this effect.

1.3. Experimental results for the size of the droplets and the place of breakup

The analytical model is verified with experimental data and does not contain any (unknown) fitting parameter. All the needed variables are elements of physical reality that have been measured experimentally.

The inner fluid is generated with a constant pressure without any pulsations to prevent premature breakup. The outer fluid velocity was set lower than 2 mm/s to prevent premature breakup due to the viscous drag force of the outer fluid on the forming droplet.

All typical Reynolds number *Re* for the inner fluid are smaller than 0.001, implying a fully developed viscous laminar flow. Typical Weber numbers $We < 10^{-5}$ implies that inertial effects can be neglected in the auto breakup process.

A sufficiently non-wetting condition necessary for auto breakup was obtained by hydrophilising the glass capillary by flowing 0.1 M potassium hydroxide (KOH) solution and outer fluid through the capillary prior to the experiment.

The dependence on the capillary number *Ca* is shown in figure 4. At increasing *Ca* the experimental obtained droplet sizes increase a little when the *Ca* increases, and except for figure 4A, they concord with the solid lines according to the analytical model.

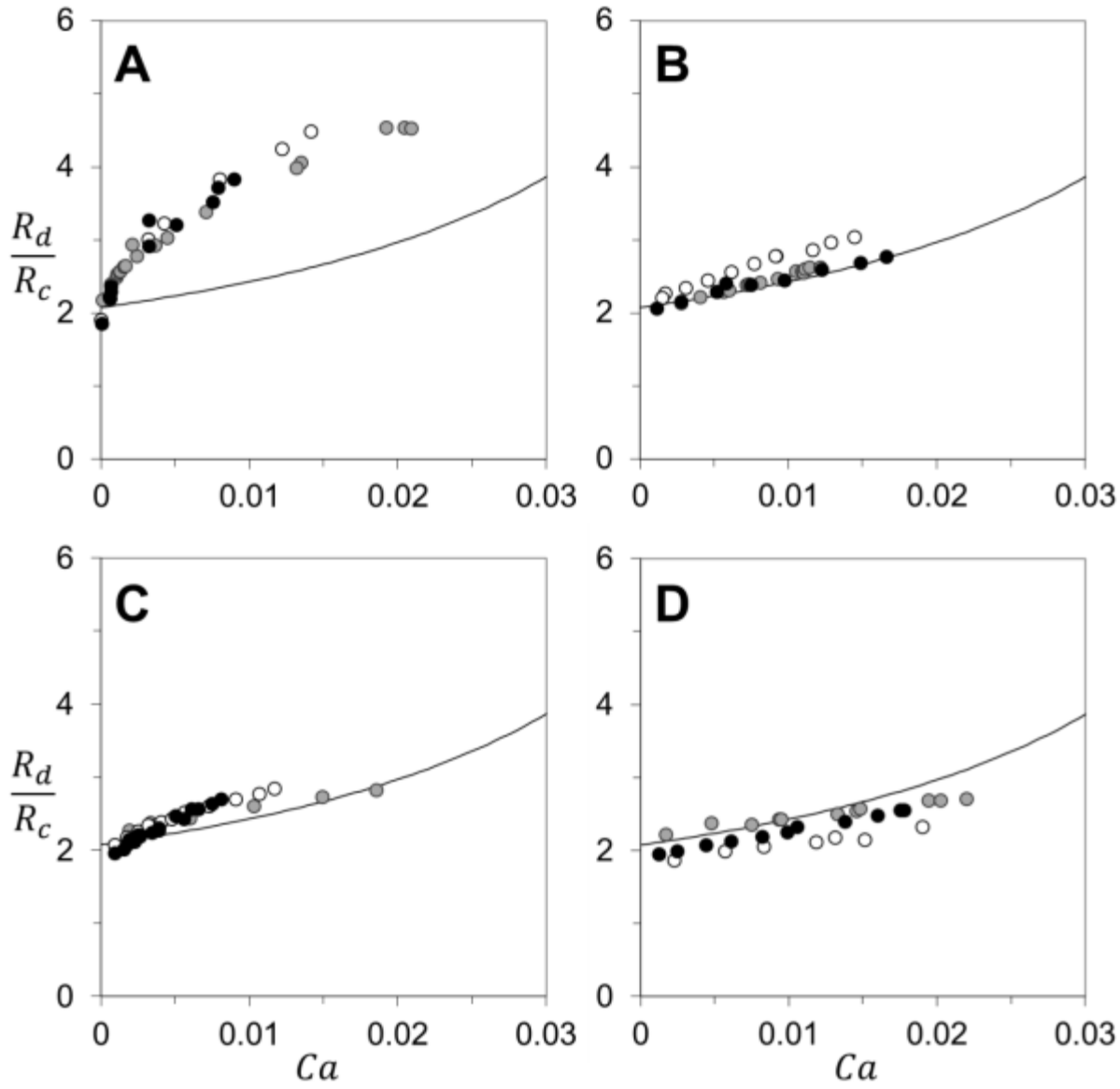

Figure 4. Graphs showing the increase of droplet radius of the final droplets at different Ca for different inner fluids: **A** silicone oil 5, **B** sunflower oil, **C** silicone oil 100, and **D** silicone oil 350. Different use of surfactants is marked by: (○) 1% (wt) tween20, (●) 5% (wt) tween20 and (●) 1% SDS (see table 1). Solid lines present the model from equation (12).

Combined experimental data of figure 4 is depicted on a logarithmic scale in figure 5, including the measurements outside the predicted auto breakup regime. According to our model we predict the existence of infinitely large droplets when Ca exceeds the Ca_{cr} number (=0.0625), and this is indeed verified. At Ca > 0.03 indefinite droplet sizes were

found, due to partially collapse of the liquid thread, resulting in an increase of velocity through this smaller cross section, implying a much higher effective *Ca* value. This effect is explained as set forth in 1.2.5.

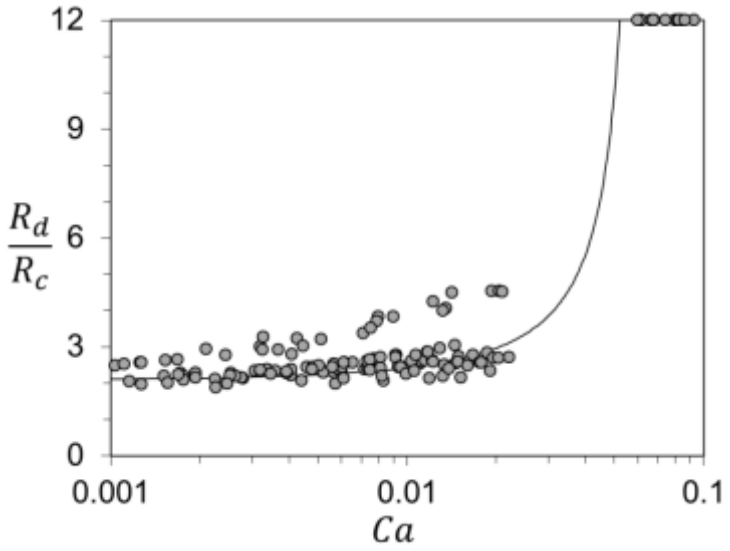

Figure 5. Showing the combined experimental data of the graphs presented in figure 4, extending now with higher capillary number *Ca*. *Ca* is shown in a ^{10}log scale for visibility. The solid line is according to the new analytical model equation (12) described in section 1.1.

The length of the breakup region *H* that has been found in the experiments by studying snapshots of movies made during the breakup process. The breakup region is located up to a length *H* inside the capillary as measured from the mouth of the capillary. Indentation (narrowing of the inner fluid cylinder) starts at the length *H*. Part of the inner fluid will subsequently be replaced by the outer fluid inwards the capillary over that length *H*. The outer fluid is being supplied from the corrugations inside the capillary, which is in contact with the bulk outer fluid. The replaced inner fluid will be up-taken by the droplet attached to the mouth of the capillary. The total amount of replaced inner fluid at the end, or slightly after the breakup process, is about a cylinder with length *H* with two half-spheres as an end cap each side.

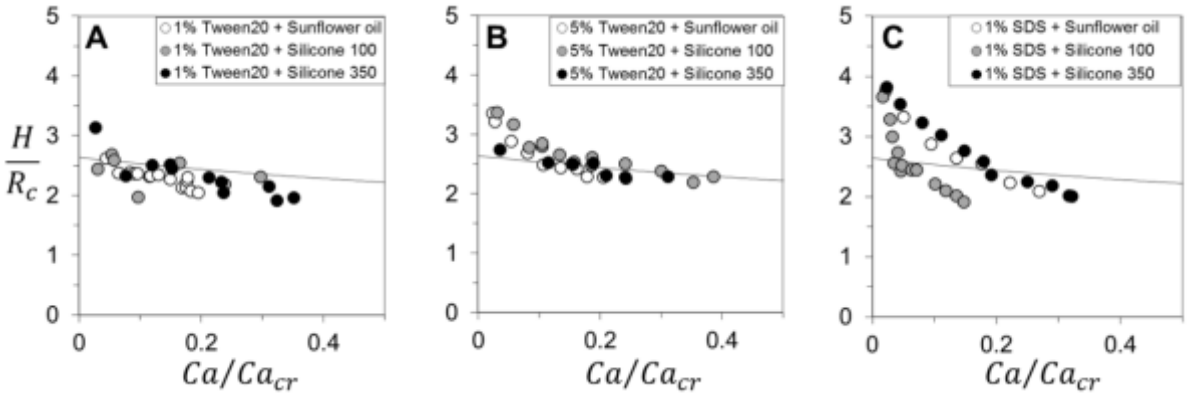

Figure 6. Graphs showing the decrease of H/R_c as function of Ca normalised to Ca_{cr}. Experimental data is from the use of different surfactants and concentrations: **A** 1% Tween20, **B** 5% Tween20 and **C** 1% SDS. Different inner fluid oils are used and marked by: (○) sunflower oil, (●) silicone oil 100 and (●) silicone oil 350 (see Table 1). Line presents the model by equation (14).

The breakup length was measured from the movies as a length H from the place where breakup starts to close the exit of the capillary mouth (figure 6). This length H becomes somewhat smaller at an increasing inner fluid velocity. The experimental data are scattered around the theoretical line, however the trend of the analytical model (solid line) is retrieved (figure 2B).

2. Conclusions

A new analytical model describing auto breakup has been presented predicting a critical capillary number Ca_{cr} of 1/16 (=0.0625) is derived. Predicted droplet sizes R_d have been accurately experimentally verified, and also the predicted length of breakup H has been verified. Between capillary number 0.03 and 0.0625 very large and also smaller droplets have been found, and this effect is possibly due to the formation of a partially collapsed inner liquid thread in the microfluidic channel near the Ca_{cr} point.

Chapter 4

Shape and stability of a viscous liquid thread in free surface flow

Abstract

In this chapter the formation and stability of a viscous liquid thread in free surface flow feeding a droplet is demonstrated and discussed. Inside the thread, fluid is in motion and moves towards the droplet. A model based on Navier-Stokes equations is introduced that describes the experimental data accurately. A pressure gradient has been identified as main parameter contributing to the stability of the liquid thread. Furthermore, oscillations have been observed in the liquid thread close to the growing droplet just before breakup.

1. Introduction

A droplet will detach from a leaking tap when it reaches a certain size. When the tap is opened a little further there is a transition where a liquid thread is formed between droplet and faucet (figure 1). This liquid thread may become longer when the tap is opened further. Long liquid threads have been formed also in microfluidic systems, showing a wide spectrum of instability regimes (Shaw 1984).

Figure 1. A droplet with a liquid thread is formed from a dripping tap (image from www.wikipedia.org).

Liquid threads or jets may also be generated by applying a shear force (chapter 1), when an outer fluid is shearing an immiscible inner fluid, that elongates to a liquid thread capped with a droplet. Liquid threads become longer when the applied shear force is larger (Basaran 2002, Seemann et al. 2012).

In this chapter, the role of viscous flow of the inner fluid in the formation and stability of a liquid thread in free surface flow has been studied. An oil droplet was formed at the mouth of a capillary and pulled upwards by a mild buoyancy force in water with surfactants, herewith creating a liquid thread between the capillary and the growing droplet. These liquid threads were stable for seconds up to minutes. An analytical model derived from Navier-Stokes equations is presented. This model describes the shape and

stability of widening liquid threads. This analytical model has been verified by experimental data.

1.1. Droplet formation in the dripping regime

Dripping is referred to a fluidic regime at which droplets are formed directly from a nozzle without the formation of a liquid thread or neck (Ambravaneswaran et al. 2000). Gravity and other forces that act on the droplet are interfacial tension force, drag force of the outer fluid and kinetics of the inner fluid (Wang et al. 2009).

In chapter 2 and 3, a special type of dripping regime is discussed where droplets are formed spontaneously instead of by shear forces from the outer fluid. Inside the capillary the liquid thread breaks up by interfacial forces. Inertia and viscous forces, provided by the flow of the inner fluid, are too low to stabilise the liquid thread in the auto breakup regime. At higher flow rates; above a critical capillary number Ca_{cr}, droplets become infinite large and the confined liquid thread inside the capillary seems stable due to viscous forces opposing the interfacial forces.

Droplet formation in the dripping regime changes into a jetting regime by enlarging the flow of the inner fluid. In this regime a liquid thread is formed between nozzle and droplet. Formation of an ever growing droplet supplied with inner fluid via a long and stable liquid thread in a stationary outer fluid is an interesting topic (Eggers & Villermaux 2008) and the main topic in this study (section 2 and 3).

1.2. Jetting and widening jet regime

The transition from dripping to jetting is normally caused by an increase of flow of the outer fluid or the inner fluid (Clanet & Lasheras 1999). It is perceived that the nature of the instability determines whether droplets are formed in the dripping or jetting regime (Guillot et al. 2007). An absolute instability of a liquid thread or jet is instability with a perturbation that is geometrically fixed, e.g. when he instability is close to the droplet. Absolute instability is associated with the dripping regime. On the other hand a convective instability is defined as when the perturbations increase along the jet surface,

e.g. due to capillary wave propagation. Jetting following Rayleigh-Plateau instability is an example of convective instability. Two different types of jetting may be distinguished: widening jet (figure 3) and jetting or tip streaming (figure 2).

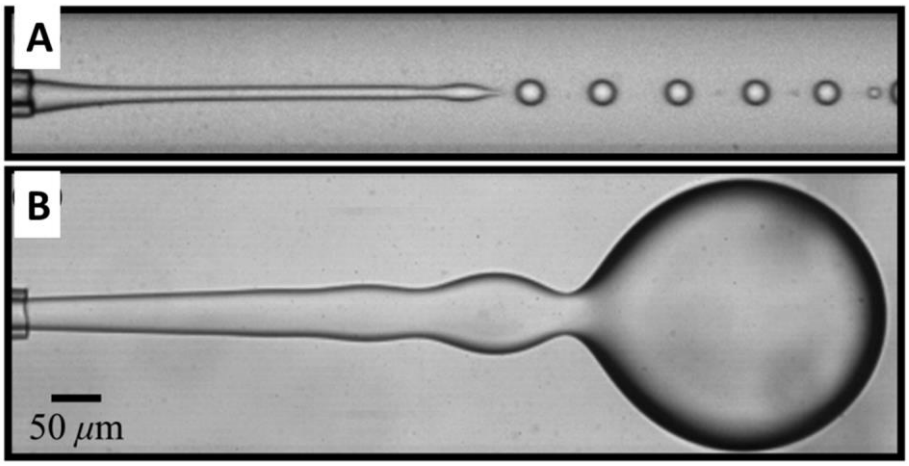

Figure 2. Microscopic images of co-flow jetting regimes. **A** Tip streaming or jetting and **B** widening jet (Utada et al. 2007).

Tip streaming may be reached by further increasing the flow of the outer fluid. A higher shear force is then applied on the liquid thread and forming droplet (Cramer et al. 2004). The droplet is dragged away and droplet size decreases with increasing co-flow. The breakup of this jet follows the Rayleigh-Plateau instability (Rayleigh 1878) and is convective due to capillary wave propagation (Eggers 1997, Utada et al. 2007). Perturbations in the jet generate multiple instabilities which are most large at the end of the jet (Ali & Umemura 2009).

The transition to a widening jet is mainly dependent on the flow of the inner fluid. The size of the droplet depends on a force balance: interfacial tension favours breakup while inertia and viscous flow of the inner fluid increase stability. Widening jets are formed in specific ranges of dimensionless numbers (see chapter 1) of the inner fluid: $We > 1$ if $Re > 1$ or at $Ca > 1$ if $Re < 1$ (Castro-Hernández et al. 2009).

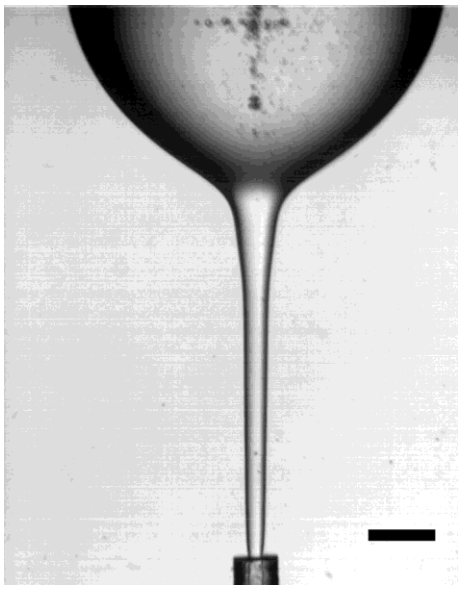

Figure 3. The liquid thread (or jet) is positively tapering towards the droplet. Inner radius of the round capillary is 50 µm. Silicone oil as inner fluid flows in 1% Tween20 in water at a rate of 0.52 µL/s. The droplet goes upward, because silicone oil has a lower density than that of water with 1% tween20 (table 1). Scale bar is 500 µm.

1.3. Navier-Stokes solutions

Fluidic flows obey the Navier-Stokes equation. This equation is derived from Newton's second law: conservation of impulse. For Newtonian fluids (incompressible and no viscoelastic effects) the following impulse conservation equation holds (equation (1)).

$$\frac{\partial v}{\partial t} + (v \cdot \nabla)v + \nabla p = \eta \Delta v + f \tag{1a}$$

and

$$\nabla \cdot v = 0 \tag{1b}$$

With v is velocity, η is viscosity, t is time, p is pressure and f is other forces.

The Navier-Stokes equations can be simplified when the fluidic system is axisymmetric (equation (2)) (Eggers 1993, 2005).

$$\underbrace{\partial_t v + v\partial_z v}_{\text{inertia}} = \underbrace{-\frac{\gamma}{\rho}\partial_z\left(\frac{1}{R_1}+\frac{1}{R_2}\right)}_{\text{Interfacial tension}} + \underbrace{3\frac{\eta}{\rho}\frac{\partial_z\left(R^2(\partial_z v)\right)}{R^2}}_{\text{viscosity}} + \underbrace{g}_{\text{gravity}} \tag{2a}$$

With R is local radius along z, γ is interfacial tension, ρ is density, R_1 and R_2 are radii of curvature and g is acceleration by gravity. Equation (2a) is a balance of forces in the dimension of acceleration. The first two terms form inertia. The third term is the pressure change term from equation (1), now defined by Laplace pressure of a curved interface. The fourth term contains viscous effects and the last term g is gravitational acceleration.

Equation (2b) is the conservation of mass:

$$\partial_t R^2 + \partial_z(vR^2) = 0 \tag{2b}$$

1.4. Liquid thread instability and micro-thread formation

Often a thin micro-thread is observed during the final part of droplet detachment, for example, as observed in figure 4. This breakup behaviour is observed in dripping, jetting and capillary bridging (McKinley 2005). The occurrence of micro-threads seems universal since the formation seems not dependent on initial conditions, nature of perturbations and length scale dimensions (Kowalewski 1996). The formation of micro-threads has also been studied in non-Newtonian fluids as polymer solutions, shear thinning and visco-elastic fluids. The shape and stability of these micro-threads depends on the inertial and viscous behaviour of the fluid which is more complex than from Newtonian fluids (McKinley 2005). The fluid dynamics of non-Newtonian fluids is out of the scope of this thesis.

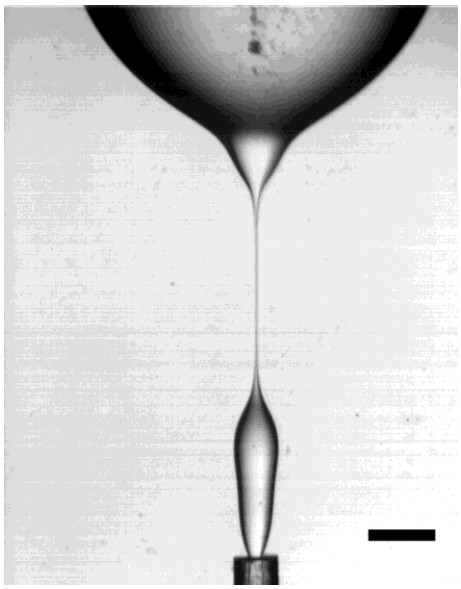

Figure 4. The snapshot shows a micro-thread during threading 10 ms before breakup in a gravitation field. Silicone oil 350 is dispersed in 1% Tween20 in water at a rate of 0.52 µL/s; velocity v_0 = 33.8 mm/s. Inner radius of the round capillary is 50 µm. Scale bar is 500 µm.

The formation of a micro-thread during the breakup process is considered to be asymmetric and nonlinear. It is asymmetric in the threading area because during thinning of the initial liquid thread, fluids at both side of the indentation retreat at different rates. This process is found to be self-similar, and often more and thinner micro-threads are formed in a cascade. The micro-thread can easily break at multiple positions leading to small satellite droplets. Multiple satellite droplets of dissimilar sizes originate from an asymmetric cascade of breakups (Shi et al. 1994). Obviously, the size of the satellite droplets depends on the volume between the two breakup points.

But why do micro-threads occur? The answer may be found in mathematics, which describes a micro-thread as a singularity that appears to be rather universal. Three parameters are important to characterise the fluid dynamics of a liquid thread: the radius of the nozzle, the capillary length ($l_c = \sqrt{\gamma/(\rho g)}$) and a characteristic viscous length (Eggers 1993). The length of the micro-thread is larger at larger viscosities. The minimal diameter of a micro-thread was found to be about 1 µm and seemed to be independent of liquid properties and molecular effects (Kowalewski 1996).

Liquid thread instability may also be induced by perturbations, which grow in time leading to breakup. Growing perturbations, observed as oscillations on a liquid thread, have been recognized as an absolute instability (Utada et al. 2008) and can be described with numerical simulations (Zhou et al. 2006).

2. Materials and methods

Experiments were performed by dispersing oils as inner fluid in an aqueous solution containing surfactant as outer fluid. The dispersing oils are silicone oils and sunflower oil. Viscosities of the inner and outer fluid are measured by rheometer (Paar Physica MCR 300) at 25 °C. Interfacial tension between the inner and outer fluid is measured using pendant drop method by using profile analysis tensiometer (Sinterface PAT-1). Densities of all fluids were measured at 20 °C using balancing density meter. Interfacial tensions γ, viscosities η, and densities ρ of inner fluids and outer fluids are listed in table 1.

Table 1. List of physical properties of the inner fluids and outer fluids: interfacial tensions γ, viscosities η, and densities ρ at 20 °C.

	η (mPa·s)	ρ (kg/m^3)	γ (mN/m)	
			1% Tween20	1% SDS
Silicone oil 5	5	917	4.0	6.1
Sunflower oil	68	919	4.5	2.3
Silicone oil 350	370	972	5.0	8.0
1% Tween20	1	998	-	-
1% SDS	1	1000	-	-

Two experimental setups as depicted in figure 5 were used. A capillary was brought in a microfluidic device and filled with outer fluid. The inner dimension of the rectangular device chamber is width 10 mm, depth 10 mm, and length 120 mm. Micro-corrugated capillaries (described in chapters 2 and 3) with inner radius of 62 μm or round capillaries with inner radius of 50 μm were used. Inner fluid was led through a capillary

by injection from a syringe pump. Droplet formation and thread formation were recorded by a conventional camera (Motic MC 2000) or high speed camera (Motionpro HS4) attached to an Olympus ZSX12 optical microscope. Droplets experience buoyancy, since the density of outer fluid is higher than of the inner fluid. The whole setup, including microscope, was adjustable with respect to the direction of gravity.

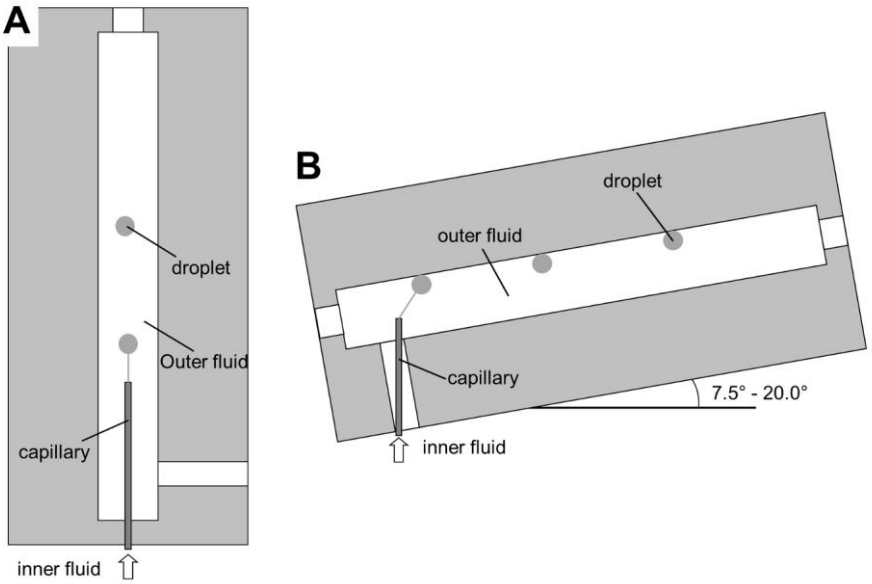

Figure 5. Experimental setup of the microfluidic device for studying liquid thread formation. **A** vertical thread formation, and **B** thread formation under a tilted angle.

Experiments with setup figure 5A yielded relatively short liquid threads for a brief time before the droplet pinches off from the liquid thread mainly due to buoyancy. In a similar experiment therefore the setup was tilted (figure 5B). Before the droplet pinches off it has reached the ceiling that immediately balances the buoyancy force to a large extent. With this setup it was well possible to monitor the stability of the thread while the droplet is stretching the liquid thread by buoyancy force but with considerable less force. Angle of tilt was 7.5° or 20.0°.

Images were processed by ImageJ software to retrieve the coordinates of the outline of the droplet and liquid thread. The coordinates of the interface were processed, together with the frame rate, by scripts in Matlab software to obtain the flow rate and droplet

radius. A detailed description of processing the captured images is found in appendix A. Thread lengths and thread radii were manually measured by using ImageJ software. Ordinary differential equations (ODE) were solved numerically by using the ode45 function in Matlab.

3. Stability of the liquid thread

Based on Navier-Stokes equations for axisymmetric systems we will attempt to describe shape and stability of liquid threads that have been obtained in the experiments.

3.1. Observing liquid thread formation

First a droplet will grow until it is big enough to leave the capillary mainly due to buoyancy and outflow of the inner fluid (figure 6). The velocity at the exit of the capillary v_0 of the silicon oil is 33.8 mm/s (which is well above the auto breakup critical velocity 0.84 mm/s, chapter 3). The length of the thread that is generated increases steadily for a number of seconds. At a certain length the liquid thread suddenly becomes instable (figure 6, frame -40ms), and a few wobbles in the thread close to the droplet are observed (see also section 3.5). The wobbles are considered absolute instabilities that lead to breakup of the liquid thread close to the droplet. The cylindrical thread retracts forming a new spherical droplet and the process restarts.

The thread breaks close to the droplet when the surface tension holding force of the liquid thread comes close to the buoyancy force. From the example of figure 6, the buoyancy force is about 3.6 μN, while the tapering thread holding the droplet with a interfacial tension force of about 2.5 - 4.7 μN around the place of breakup (see section 3.2 for explanation of the forces).

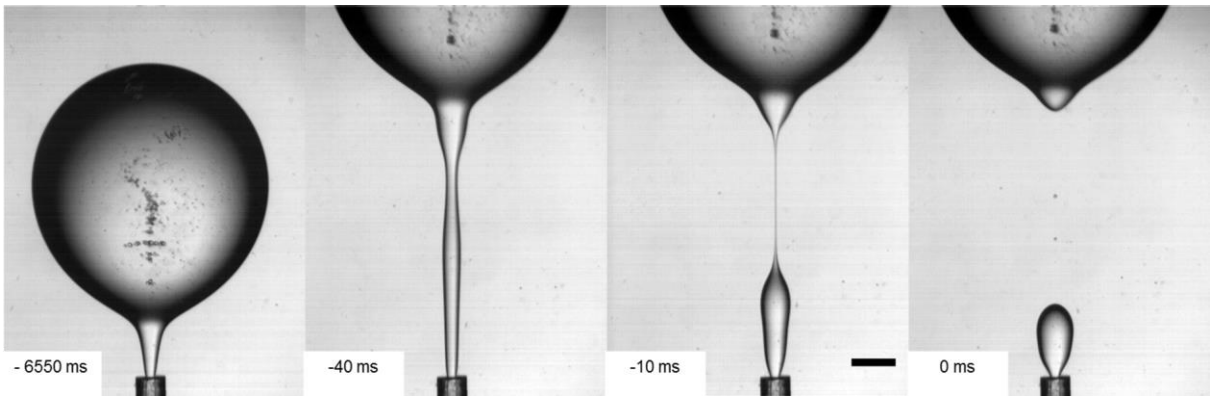

Figure 6. Snapshots of droplet and thread formation. Silicone oil 350 is dispersed in 1% Tween20 in water at a rate of 0.52 µL/s and v_0 = 33.8 mm/s. Inner radius of the round capillary is 50 µm. Scale bar is 500 µm.

Liquid threads of a lower viscosity (5 mPa·s silicone oil) of the inner fluid is shown in figure 7. The shape of the liquid thread is less straight, because of periodically changes in the thread radius, which can also be seen in jetting. The velocity of the inner fluid of the configurations depicted in figures 6 is about 4 times higher than the configuration depicted in figure 7. These observations suggest that viscous liquid threads may be straightened by viscous shear that is larger at higher inner fluid velocities and higher viscosities. Also a micro-thread is observed in figure 7, but much shorter than observed from figure 6.

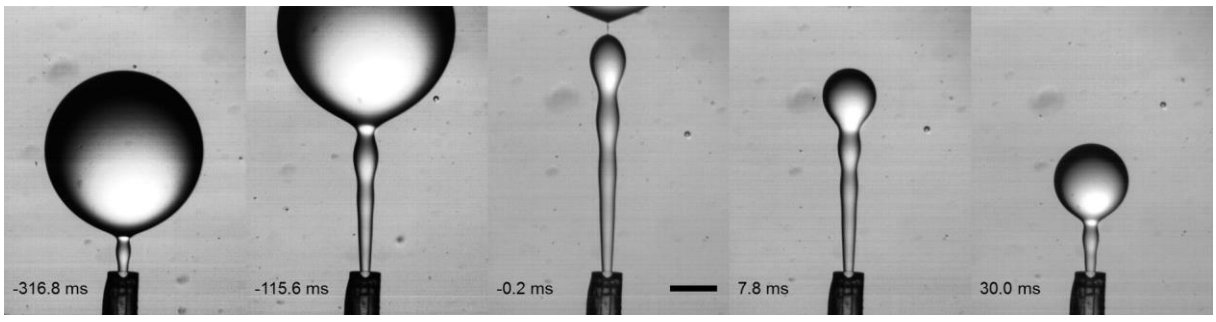

Figure 7. Snapshots of droplet and thread formation. Silicone oil 5 is dispersed in 1% Tween20 in water at a flow rate of 0.12 µL/s; velocity v_0 of 7.8 mm/s. Inner radius of the round capillary is 50 µm. Scale bar is 500 µm.

A very low interfacial tension γ < 0.1 mN/m (too low to be measured by pendent drop method) has been realised by emulsification of sunflower oil in 0.1 M potassium hydroxide (KOH) in water solution (see figure 8). Hydroxides hydrolyse the ester bonds of sunflower oil at the interface making the products more water soluble and interfacial active.

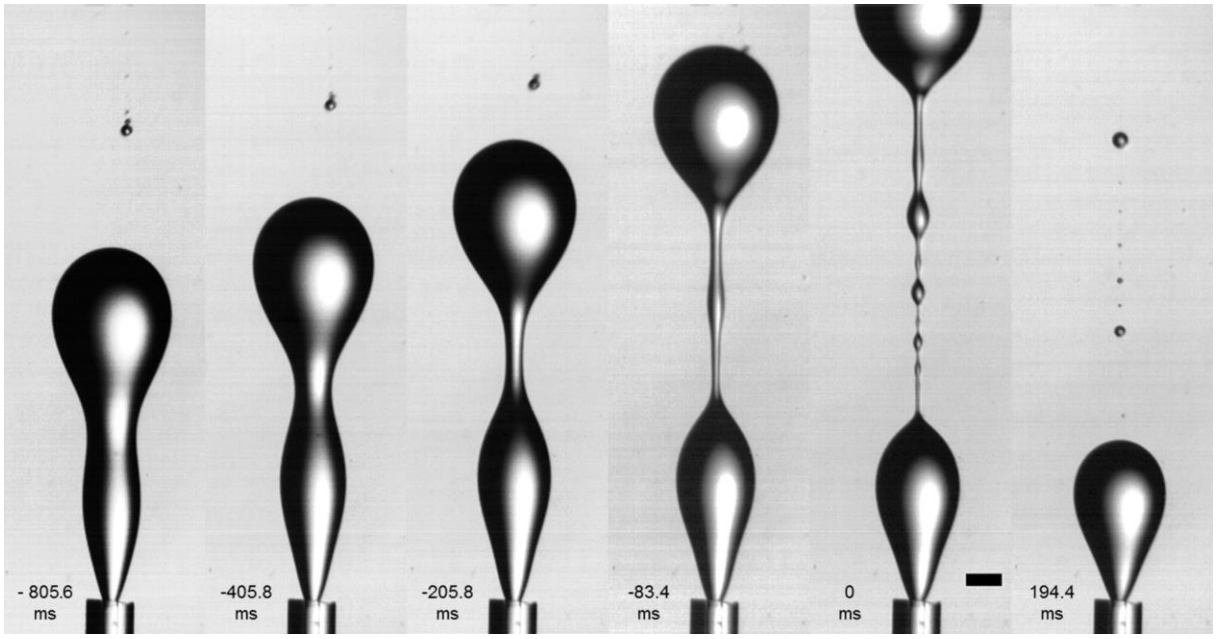

Figure 8. Snapshots of emulsifying sunflower oil in 0.1 M KOH in water at a flow rate of 0.067 µL/s; velocity v_0 of 4.4 mm/s. The round capillary has an inner radius of 50 µm. Cascades of liquid micro-threads and satellite droplets are observed. Scale bar is 250 µm.

In order to diminish the effect of buoyancy and to obtain much longer liquid threads we have matched the mass density of the oil and water (difference in density between inner and outer fluid is about 30-90 kg/m^3 for the high viscous oil) and a tilted set-up is used to decrease the effect of buoyancy (Figure 5B and 9).

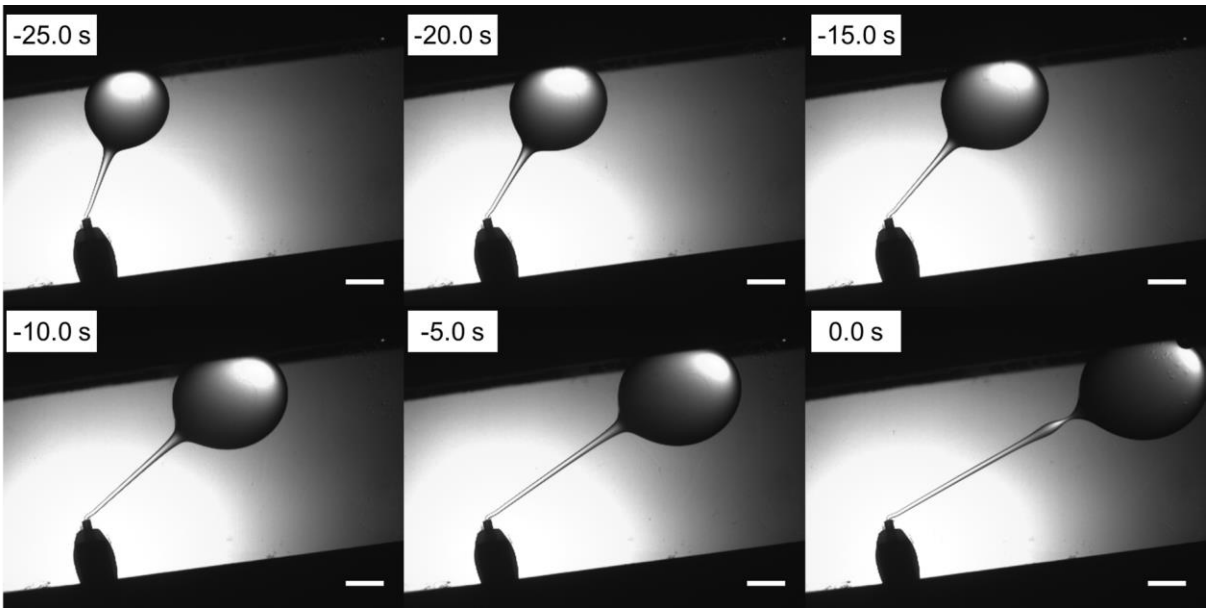

Figure 9. Snapshots of droplet and thread formation. The droplet has reached the tilted ceiling before breakup and moves further away from the capillary stretching the liquid thread. Silicone oil 350 is dispersed in 1% Tween20 in water at a velocity of 162.9 mm/s. Inner radius of the round capillary is 50 µm. Scale bar is 2000 µm.

3.2. Force balance between of droplet and liquid thread

Buoyancy force will lift the sufficient large droplet from the capillary and makes it possible to generate a liquid thread. The thread becomes longer when the droplet is pulled further away from the capillary. Its stability is remarkable, since non-spherical liquid shapes are considered to be instable. Probably another force contributes to the stability of the liquid thread. The lifting of the droplet happens when the interfacial tension force F_{st} (equation (3)) holding the droplet at the capillary mouth (van Rijn 2004) becomes smaller than the buoyancy force F_B (equation (4)). So, a droplet starts to go up when

$$F_{st} = 2\pi R_{thread}\gamma \tag{3}$$

is equal to

$$F_B = \frac{4}{3}\pi R_d^3 \Delta\rho g \tag{4}$$

The magnitude of buoyancy increases with increasing radius of the droplet, while the interfacial tension force remains constant as long as the liquid thread radius does not change. The interfacial tension force is in the order of 1.6 µN at a thread radius of 50 µm, which is equal to a buoyancy force of a droplet with a radius of 1.1 mm in our system with the high viscous oil (Table 1).

The buoyancy force can be tempered by applying a tilted ceiling in the module (figure 5B). When a droplet floats at the ceiling, the droplet floats nearly horizontally away from the nozzle. The force balance is depicted in figure 10 where the droplet applies force on the liquid thread from the tempered buoyancy.

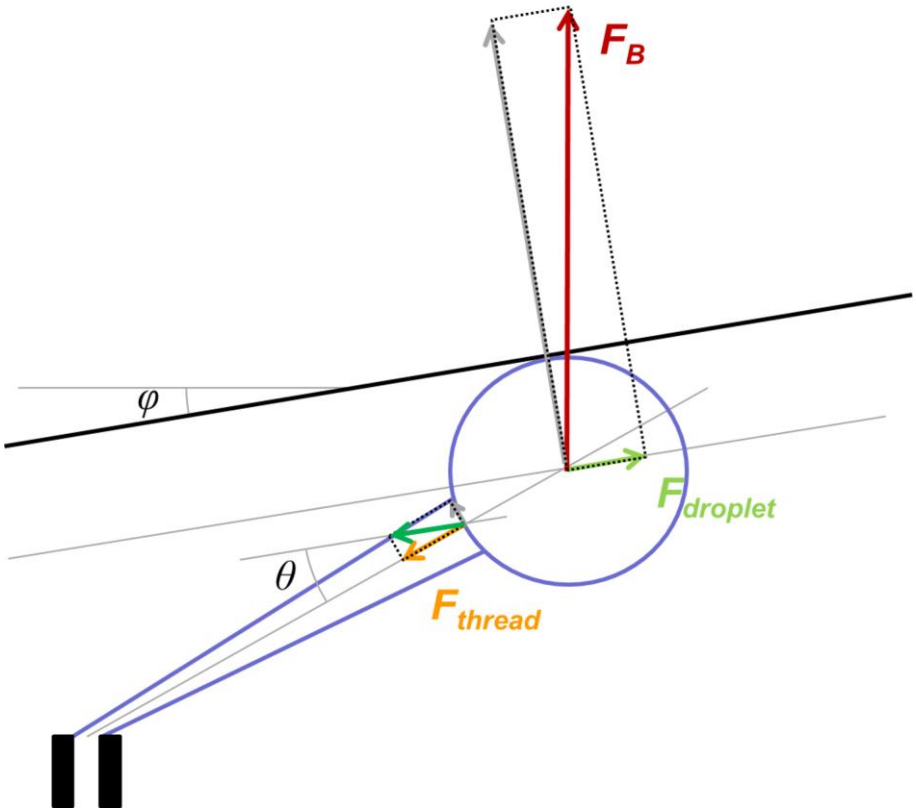

Figure 10. Schematic image of the force balance on the droplet and liquid thread (see Fig 5B).

Buoyancy force F_B has one component acting on the droplet $F_{droplet}$. That is opposed by the surface tension holding force F_{thread} of the liquid thread. The force $F_{droplet}$ on the droplet along the ceiling with angle φ is:

$$F_{droplet} = F_B \cos\varphi \tag{5}$$

The force on the thread F_{thread} changes in time, because at a longer thread the angle θ is decreasing, the force balance is:

$$F_{thread} = F_B \cos\varphi \cos\theta \tag{6}$$

Now return to the stability of the liquid thread by looking in particular at the viscous flow of the inner liquid depicted in figure 11. The viscous force $F_{viscous}$ is the shear acting on the inner fluid within the liquid thread that creates a viscous pressure, that is also directed outwards. The squeezing interfacial tension force $F_{interface}$ creates a Laplace pressure difference over the interface.

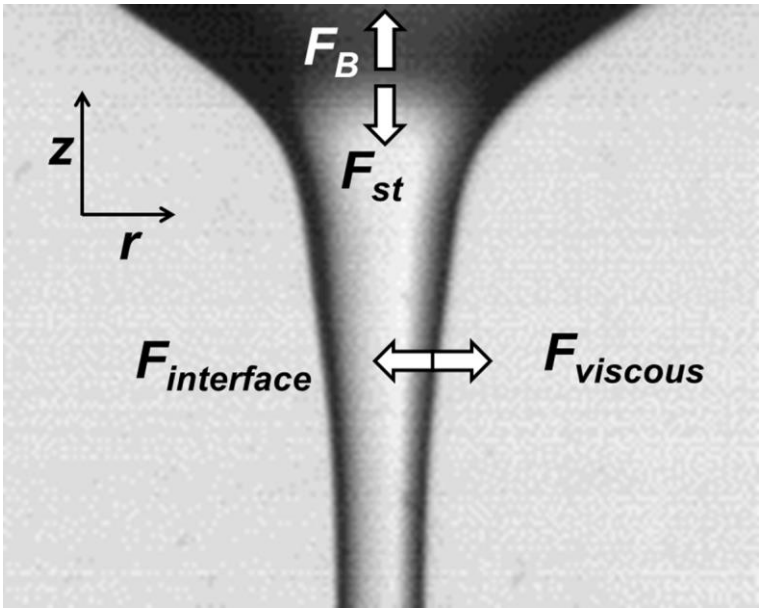

Figure 11. Image showing two force balances. The stretching of the liquid thread by buoyancy F_B is opposed by the axial surface tension force F_{st}. The viscous force $F_{viscous}$ creates a viscous pressure that is opposed by the squeezing interfacial tension force $F_{interface}$ creating a Laplace pressure difference over the interface.

The fluid dynamics of the system is operated in a laminar viscous flow regime in which inertial forces are small. A laminar flow profile is assumed in the thread relative to a moving interface. Reynolds numbers *Re* for silicone oil 350 are typically well below 1, here up to 0.01 as well as the Weber numbers *We* (0.06 – 0.07), which is significant higher than for auto breakup (chapter2 and 3). The capillary numbers *Ca* are much higher, up to 5, generating viscous forces to stabilise and keep the liquid thread open.

3.3. Model describing the shape of a widening liquid thread

The dynamical behaviour of the liquid thread is described by Navier-Stokes equations (section 1.3.). A highly useful expression for slender, axisymmetric liquid thread configurations has been derived from these Navier-Stokes equations (Eggers 2005). These equations form the basis for our analysis for the shape of a liquid thread in a form adapted to our liquid thread configuration.

$$\rho\partial_t v+\rho v\partial_z v = -\gamma\partial_z\left(\frac{1}{R}\right) + 3\eta\frac{\partial_z\left(R^2(\partial_z v)\right)}{R^2} + Q \tag{7a}$$

and

$$\partial_t(R^2) + \partial_z(v\,R^2) = 0 \tag{7b}$$

Here, z is the coordinate along the axis of symmetry, R is the radius of the thread, and v the axial velocity averaged over the cross section at z. Equation (7a) expresses conservation of impulse, and equation (7b) expresses conservation of mass. In equation (7a), three terms representing: inertia (terms with ρ), interfacial tension (term with γ), and viscosity (term with η) are recognised. The factor Q represents all remaining forces. Equation (7a) is written in the dimension of pressure gradient [N/m^3] along z. Equation (7b) is written in the dimension of acceleration [m/s^2].

The following scaling factors are applied to put equations 5 in dimensionless form:

$$v^* = \frac{v}{v_0},\quad R^* = \frac{R}{R_0},\quad z^* = \frac{z}{R_0},\quad t^* = \frac{v_0 t}{R_0},\quad Q^* = \frac{R_0 Q}{\rho v_0^2} \tag{8}$$

The asterisk '*' indexes the dimensionless form of the corresponding variable. Here, R_0 is the radius of the thread at a very small distance from the nozzle exit and v_0 is the velocity at R_0.

Linear terms describe the fluid dynamics adequately under the assumption that the liquid thread has a slender shape. The second principle curvature can be neglected in slender jet approximation in the interfacial tension term.

An important observation is that the shape and length of the thread as a whole change quite slowly. This implies that a quasi steady-state approach seems applicable. The time derivatives in equation (7) are set equal to zero by this approach. Steady state solutions of equation (7) satisfy in dimensionless form:

$$-v^* \, \partial_{z^*} v^* - 2 \, \alpha \, \frac{1}{R^{*2}} \partial_{z^*} R^* + \beta \, \frac{1}{R^{*2}} \, \partial_{z^*} \left(R^{*2} (\partial_{z^*} v^*) \right) + Q^* = 0 \tag{9a}$$

and

$$\partial_{z^*} (v^* \, R^{*2}) = 0 \tag{9b}$$

with dimensionless constants:

$$\alpha = \frac{\gamma}{2 \rho v_0^2 R_0} \quad and \quad \beta = \frac{3 \eta}{\rho v_0 R_0} \tag{10}$$

Equation (9b) is straightforwardly integrated and yields, in dimensionless form, the relation between velocity and liquid thread radius:

$$v^* = \frac{1}{R^{*2}} \tag{11}$$

So, the velocity v at z is inversely proportional to the area of the cross section at z, as is to be expected from the conservation of mass. After substituting this explicit expression for v in the impulse equation and working out the derivatives, we arrive at equation (12):

$$2 \frac{1}{R^{*5}} \, \partial_{z^*} R^* + 2 \, \alpha \, \frac{1}{R^{*2}} \partial_{z^*} R^* - 2 \, \beta \, \frac{1}{R^{*2}} \, \partial_{z^* z^*} (\ln R^*) + Q^* = 0 \tag{12}$$

Equations (13) can be rewritten by applying a transformation $y = 2 \ln(R^*)$, with R^* the dimensionless thread radius, leading to a second order differential equation for y:

$$\beta e^{-y}\partial_{z^*z^*}y - e^{-2y}\partial_{z^*}y - \alpha e^{-0.5y}\partial_{z^*}y = Q^* \quad (13)$$

An analytical solution for equations (12) has been obtained by (Clarke 1966) if the surface tension term can be neglected ($\alpha = 0$). For $\alpha \neq 0$ equation (12) can only be solved by a numerical approach. The two initial values needed to solve this second order differential equation are y and $\partial_z y$ at $z = 0$. The initial value of $R_0^* = 1$, and therefore, $y(0) = 0$. The slope of $y(0)$ is assumed to be $\partial_z y = 0$ because the thread hardly tapers close to the capillary.

The ordinary differential equation (13) was solved numerically with results shown in figures 12 and 13. Here, Q is fitted to the experimental data for several liquid threads per movie. Per plot, the last of the experimental data curves show effects of wobbles (see section 3.5) on the liquid thread shapes prior to breakup.

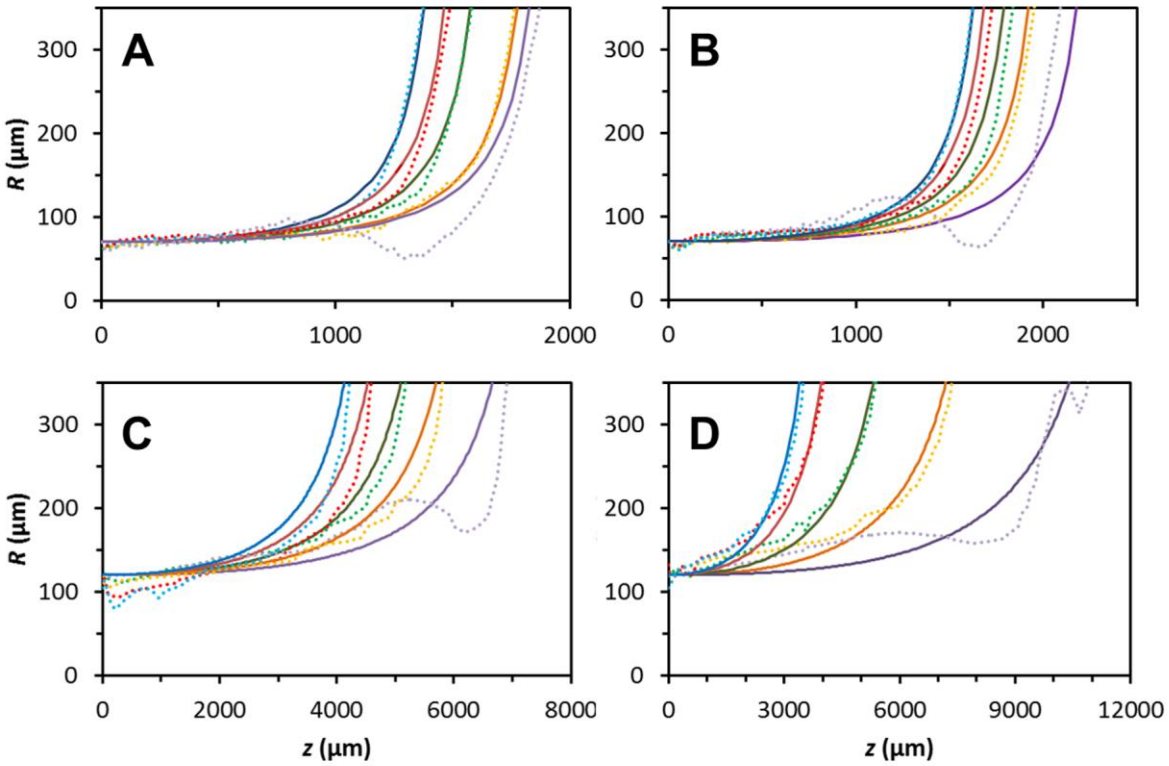

Figure 12. Graphs showing the radius of the liquid thread derived from equation (13) and experimental data with a tilted fluidic system figure 5B. Dashed lines are experimental data, and solid lines are calculations by equation (13). **A** at v_0 is 23.6 mm/s, **B** at v_0 is 27.7 mm/s, **C** at v_0 is 58.1 mm/s, and **D** at v_0 is 162.9 mm/s.

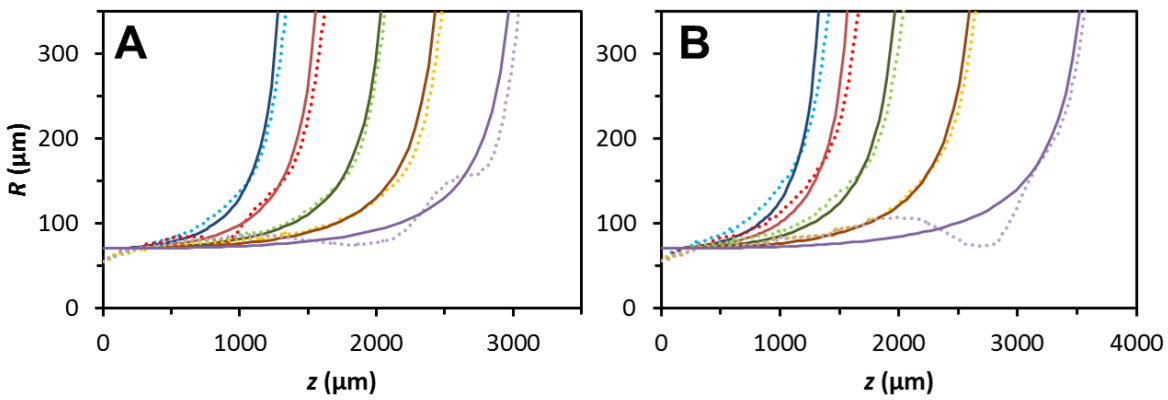

Figure 13. Graphs showing the radius of the liquid thread derived from equation (13) and experimental data with an upward fluidic system figure 5A. Dashed lines are experimental data, and solid lines are calculations by equation (13). **A** at v_0 is 33.8 mm/s, and **B** at v_0 is 45.4 mm/s.

Equation (13) with its initial conditions has for $Q = 0$ a solution $y = 0$ for all z, which corresponds with the straight cylinder with $R^* = 1$. For $Q > 0$ the solution is a profile with increasing R for increasing z.

For small values of z equation (13) has as approximate solution:

$$y \sim \frac{Q}{2\,\beta}\,z^2 \tag{14}$$

which corresponds with the dimensionful liquid thread profile:

$$R \sim R_0 + \frac{Q\,R_0}{12\,v_0\,\eta}\,z^2 \tag{15}$$

The shape of the liquid thread close to the nozzle, so for small z, fits nicely by this quadratic approximation (equation (15)) as shown in the log-log plot in figure 14. However, the fit deviates from this approximation when z is closer to the droplet.

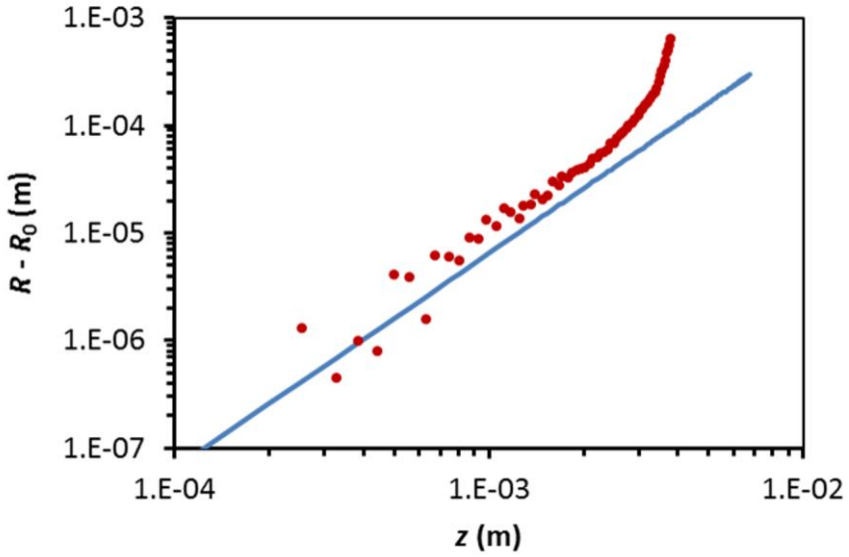

Figure 14. Log-log plot of shape of the liquid thread, and fit from equation (15). This example is a fit for snapshot 25.05 s before breakup (velocity v_0 is 162.9 mm/s).

3.3.1. Dependence of Q on thread length

As mentioned above, Q with the dimension of pressure gradient represents all other contributions than the ones related to inertia, interfacial tension, gravity and viscosity of the inner fluid. The two remaining pressure contributions to Q are therefore: the applied pressure at the exit of the capillary and possible energy dissipation via the interface of the liquid thread with the outer fluid.

The first of the two remaining pressures is due to the pressure difference between the exit of the capillary and the droplet. In fact this exit pressure is the main driving force that causes the inner fluid to flow and is essential for the thread and droplet to come into existence. The inner fluid will exit the capillary at a certain high pressure P_n, and flows via the liquid thread to low pressure in the droplet.

At the capillary exit also die swell is observed, which is an expansion of the fluid radius close to the exit of the capillary. Within a short distance the radius of the liquid thread becomes larger than the nozzle radius, and will consume part of the exit pressure (Tanner 2005). At the droplet side of the liquid thread the Laplace pressure is: $P_d = \frac{2\gamma}{R_d}$

(with R_d is radius of the droplet). A quasi-steady state pressure difference can therefore be defined as $Q_0 \equiv P_n - P_d$.

The second possible contribution to Q emerges from the viscous drag exerted on the outer fluid by the inner fluid flow. This enables movement of the outer fluid and energy dissipation. Moreover the existence of this outer fluid energy dissipation also implies an additional finite inner fluid energy dissipation that is not included in the above presented equations. We will denote this counteracting dissipative contribution as Q_1, and is explained further in section 3.3.2.

Q_0 and Q_1 scale differently with thread length L. The longer the thread, the smaller the gradient of the pressure difference Q_0 will be. This inverse scaling with thread length does not hold for Q_1 since the drag of the outer fluid on the inner fluid scales with the amount of dissipated energy transferred to the outer fluid and is proportional with the interface area, and thus with thread length L. These insights tell us that Q might be composed of the following terms:

$$Q = \frac{Q_0}{L} - Q_1 \tag{16}$$

Note that Q_0 is not completely constant during the thread forming process, since the viscous stress P_n at the capillary is kept constant, but the Laplace pressure P_d in the droplet will change slightly in view of its slowly increasing radius. Further, the dissipation factor Q_1 might somewhat vary along the thread, in view of the widening shape of the liquid thread.

3.3.2. Energy dissipation Q_1

The dissipation term Q_1 in equation (16) can be estimated by looking more closely to the energy dissipation at the interface of the liquid thread. The tapering of the thread profile will be neglected, for avoiding unnecessary complexity, and the thread surface is considered to be a cylinder. Further the flow is assumed to be laminar in the outer fluid. Equations (1 and 2) in (Eggers & Dupont 1994) in cylindrical coordinates have been derived, but for a thread with a free surface.

A boundary condition for the tangential force balance (see e.g. equation 5 in (Eggers & Dupont 1994)) is the expression:

$$\boldsymbol{n} \cdot \boldsymbol{\sigma} \cdot \boldsymbol{t} = 0 \tag{17}$$

$\boldsymbol{\sigma}$ is the stress tensor, $\boldsymbol{n}$ is the orthogonal unit vector, and $\boldsymbol{t}$ is the unit vectors tangential to the thread surface. The common Newtonian stress tensor is used for $\boldsymbol{\sigma}$.

The moving oil thread surface drags water with it and sets it into motion. This way energy is transferred, that is next dissipated in the outer fluid. So, the water exerts a slowing down force on the liquid thread. For a cylindrical thread the tangential force balance reads as:

$$\boldsymbol{n} \cdot \boldsymbol{\sigma} \cdot \boldsymbol{t} = \eta_{out} \dot{\gamma} \tag{18}$$

In this expression $\dot{\gamma}$ is the derivative of the longitudinal velocity in the surrounding aqueous solution with respect to the radial coordinate, take at the thread surface. η_{out} is the viscosity of the outer fluid, in this case water. If one uses expression (18) as boundary condition in the derivation in (Eggers & Dupont 1994) instead of equation (17), we get

$$Q_1 = \frac{2\,\eta_{out}\,\dot{\gamma}}{R_0} \tag{19}$$

in dimensionless form:

$$Q_1^* = \frac{2\,\eta_{out}\,\dot{\gamma}}{\rho\, v_0^2} \tag{20}$$

Equation (19) shows that energy dissipation as shown in the term Q_1 is dependent on the shear rate $\dot{\gamma}$ of the outer fluid. Shear rate $\dot{\gamma}$ can be estimated as shown in the following section.

3.3.3. Fitting of shear rate $\dot{\gamma}$ from outer fluid velocities

The shear rate of the outer fluid at the interface can be estimated from studying the velocity profile of the outer fluid by velocity tracking of particles present in the outer

fluid. These particles were followed throughout the last seconds before breakup. The measurements were performed in the area half way the liquid thread.

Here we assume that the velocity of the outer fluid v_{out} is inverse with the radial r to the liquid thread (equation (21)). The average velocity of the interface $v_{0.5L}$ is considered at the radius of the interface $R_{0.5L}$ at half the length of the liquid thread.

$$v_{out} = v_{0.5L} \frac{R_{0.5L}}{R_{0.5L} + r} \tag{21}$$

and its derivative to r is the shear rate:

$$\frac{\partial v}{\partial r} = -v_{0.5L} \frac{R_{0.5L}}{R_{0.5L} + r^2} \tag{22}$$

The absolute shear rate $\dot{\gamma}$ at the interface, or where r=0, can be calculated from equations (21 and 22):

$$\dot{\gamma} = \frac{\partial v}{\partial r} \Big|_{r=0} = \frac{v_{0.5L}}{R_{0.5L}} \tag{23}$$

Examples of outer fluid velocity data in the outer fluid are given in figure 15 and 16.

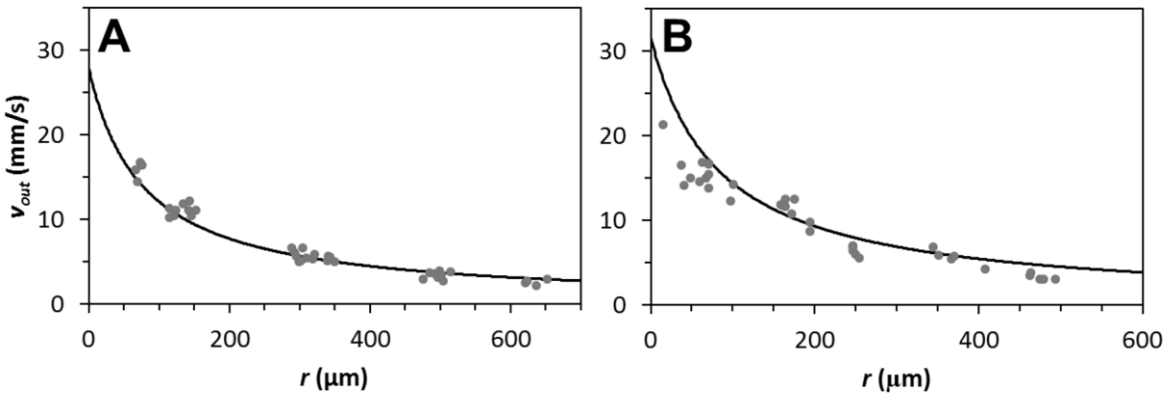

Figure 15. Two examples of velocity profiles of the outer fluid for experiments according to figure 5A. **A** at v_0 is 33.8 mm/s, and **B** at v_0 is 45.4 mm/s. The solid lines are fits according to equation (21).

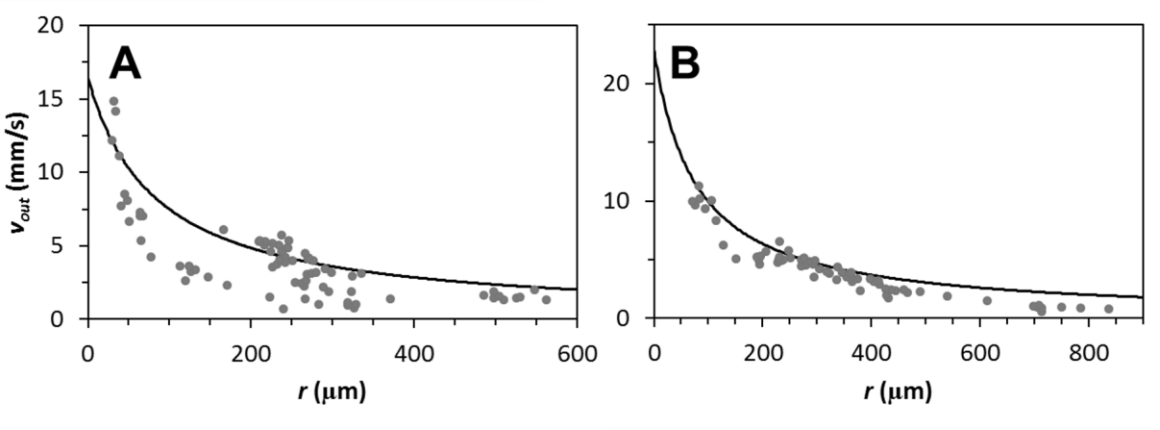

Figure 16. Two examples of velocity profiles of the outer fluid for experiments according to set-up figure 5B. **A** at v_0 is 23.6 mm/s, and **B** at v_0 is 27.7 mm/s. The solid lines are fits according to equation (21).

In figure 15 and 16 the velocity of the particles follows the theoretical v_{out} (solid lines) from equation (21). It is difficult to measure particles close to the interface, also the tracking particles are projected in snapshot images and may be below or in front of the plane of focus of the microscope focused on the liquid thread.

The velocity at the interface is always lower than the velocity v_0 at the nozzle due to the tapering of the liquid thread. The radius $R_{0.5L}$ of the liquid thread half way its full length is about 1.1 – 1.2 times R_0. The average velocity through the liquid thread results in a 1.21 – 1.44 times lower velocity $v_{out}(r=0)$ at the fluid interface.

The shear rate $\dot{\gamma}$ at the interface has been derived from equation (23) and is shown in table 2 for the examples in figures 15 and 16.

Table 2. Shear rate $\dot{\gamma}$, and Q_1 derived from figures 15 and 16. The two numbers for $\dot{\gamma}$ and Q_1 correspond for $R_{0.5L}$ is $1.2 \cdot R_0$ and $1.0 \cdot R_0$ respectively.

Experiment	With/without ceiling	v_0 (mm/s)	$\dot{\gamma}$ (s^{-1})	Q_1 (kN/m^3)
Experiment 1	With	23.6	196 – 338	5.6 – 9.7
Experiment 2	With	27.7	229 – 395	6.5 – 11.3
Experiment 3	Without	33.8	279 – 483	8.0 – 13.8
Experiment 4	Without	45.5	376 – 650	10.7 – 18.6

3.4. Length of liquid thread

The length of the liquid thread L can be predicted with equation (16). To verify if Q_0 and Q_1 are constant, plots of Q versus $1/L$ should show a straight line. The results are given in figure 17 and 18 for six threads obtained under different conditions. Apparently Q versus $1/L$ is in the cases with ceiling well represented by a linear fit. The constant values of the linear fits are Q_0 and Q_1 and are typical for the conditions of the system under consideration (Q_1 by equation (19)).

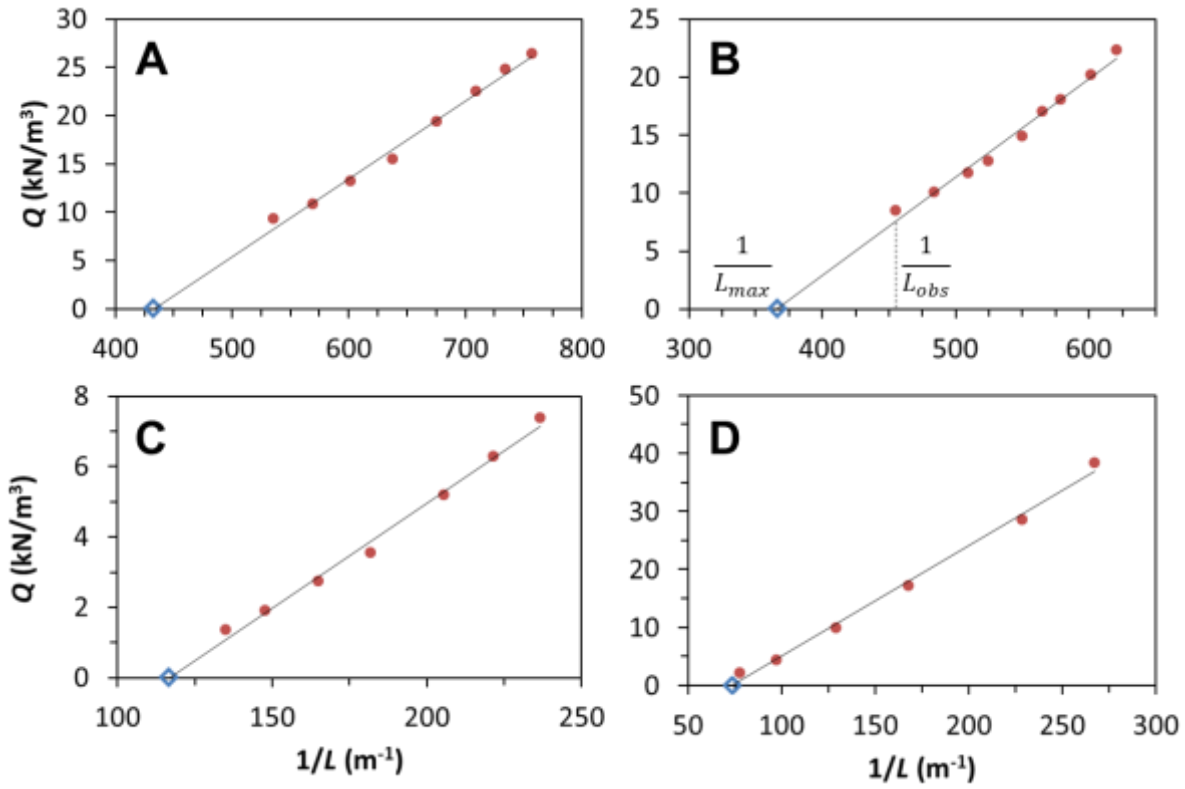

Figure 17. Graphs of Q as function of reciprocal length of the liquid thread $1/L$ of **A** at v_0 is 23.6 mm/s, **B** at v_0 is 27.7 mm/s, **C** at v_0 is 58.1 mm/s, and **D** at v_0 is 162.9 mm/s. The used set-up is the tilted microfluidic set-up according to figure 5B.

In figure 17, the pressure difference values Q form straight lines when plotted against $1/L$. This means that Q is based on a pressure gradient Q_0 that is equally distributed over the liquid thread.

With these straight line fits, the values of Q_0, Q_1 and L_{max} can be calculated for each movie (table 3). In the fits, the pressure Q_1 is the slope of the lines. The constant component Q_1 in equation (16), which appeared to adjust for loss of energy to the motion of the outer fluid, can be found from the fits by calculating $Q_1 = Q\ at\ \left(\frac{1}{L} = 0\right)$. Indeed Q_1 accounts for the dissipation of energy to the outer fluid, because the Q_1 derived in figure 17 and calculated by equation (19) have similar values.

The maximum length L_{max} could also be predicted from the plots in figure 17 (table 3). This L_{max} is the theoretical length for which Q goes towards zero. In the plots the inverse of L_{max} can be found where the straight line crosses the $1/L$-axe. The theoretical L_{max} is

slightly longer than the observed maximum length of the liquid thread L_{obs}. The breakup starts earlier than predicted, because probably the buoyancy force of the droplet and the retraction force on the liquid thread are large enough to destabilise the stabilising effect from the pressure gradient that decreases during the whole process.

For comparison to the results from figure 17, experimental data from a microfluidic set-up according to figure 5A is analysed in a similar way (figure 18).

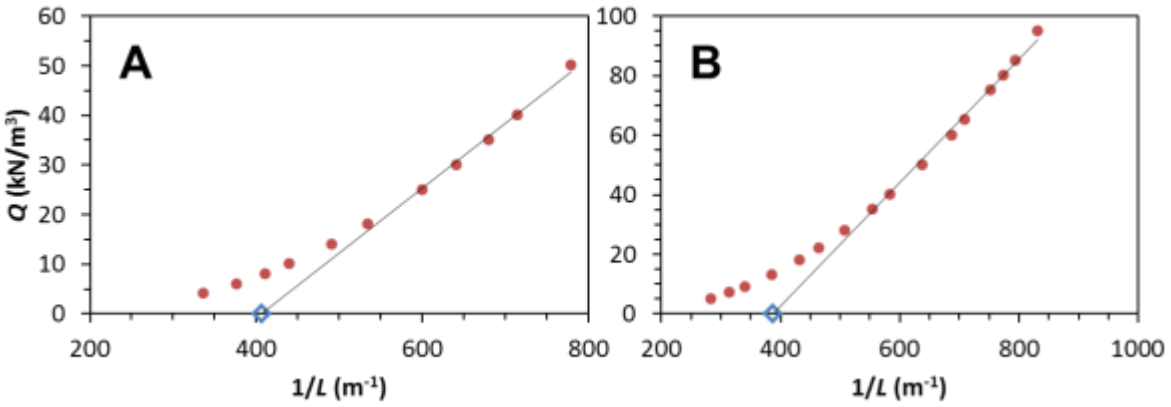

Figure 18. Graphs of Q as function of reciprocal length of the liquid thread $1/L$ of **A** at v_0 is 33.8 mm/s, and **B** at v_0 is 45.5 mm/s. The used set-up is the upward microfluidic set-up according to figure 5A.

In figure 18 is depicted that the fit of Q versus $1/L$ deviates from linear when the upward microfluidic set-up according to figure 5A is used. A linear part of the fit can still be seen in the first part of liquid thread formation when Q is still relatively large. Possibly buoyancy forces are contributing strongly in the second phase when the droplet becomes large; the breakup process is fast and quasi steady state cannot be reached.

In table 3 we summarize experimental, observed, and fitted parameter values for several experimental conditions with ceiling.

Table 3. Experimental, observed, and fitted parameter values for several experimental conditions with ceiling.

		Observed [a]	Predicted [a]	Derived [b]	Derived [b]	Derived [c]
R_0 (μm)	v_0 (mm/s)	L_{obs} (μm)	$L_{max} = Q_0/Q_1$ (μm)	Q_0 (N/m^2)	Q_1 (kN/m^3)	Q_1 (kN/m^3)
120	58.1	7490	8570	59.5	6.94	3.9 - 8.0
120	162.9	12800	13570	190.6	14.04	10.9 - 22.5
70	23.6	1920	2560	66.8	26.10	5.6 - 9.7
70	27.7	2200	2730	85.0	31.13	6.5 – 11.3

[a] Observed and predicted from figure 17.

[b] Derived from linear fit from figure 17.

[c] Derived from shear rate $\dot{\gamma}$ and equation (19).

3.5. Instabilities and oscillations of the liquid thread before breakup

During droplet formation, an instability occurs in the liquid thread close to the droplet. The moment, when those instabilities are visible, is related to the length of the liquid thread L and Q_0 and Q_1 in the value Q as described by equation (16). These instabilities have been observed as oscillations in the liquid thread, and start in our case typically when the liquid thread has reached a specific length. A moving wobble is shown in figure 19.

The oscillations become visible when the liquid thread has already reached a certain length, typically about ¾ of its maximum length, and are amplified close to the droplet (figure 20). The wobble seems to move in the liquid thread in the direction of the droplet. The wobbles travel from about half way the liquid thread towards the droplet, and look similar as travelling waves in fluid pipes (Hancock & Bush 2002). The process of breakup happens very fast during an instant of the last wobble. Also a micro-thread is formed just before pinch-off (see also chapter 6 and examples in figures 6 and 7).

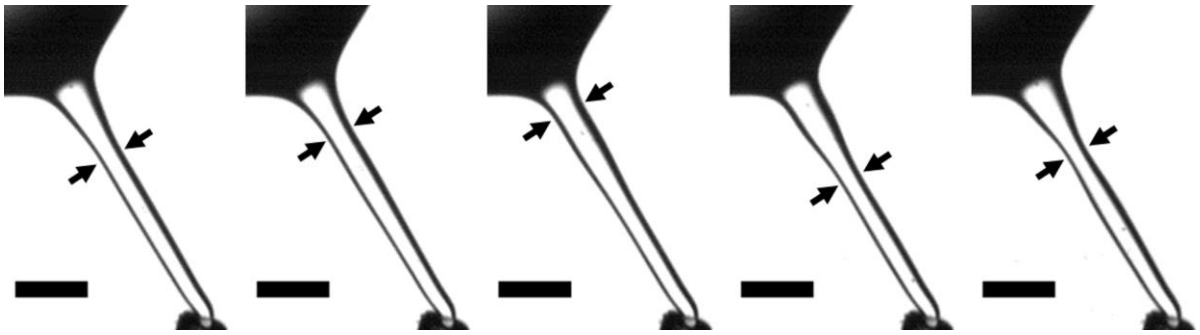

Figure 19. Snapshots zooming in on one period of oscillation in the thread. The thinnest part of the thread oscillates at this rate. The arrows mark the smallest parts of the wobbles. The time between two snapshots is 22 ms and one period is 169.8 ms. Inner radius of the round capillary is 50 µm. Velocity v_0 is 23.6 mm/s. scale bar is 500 µm.

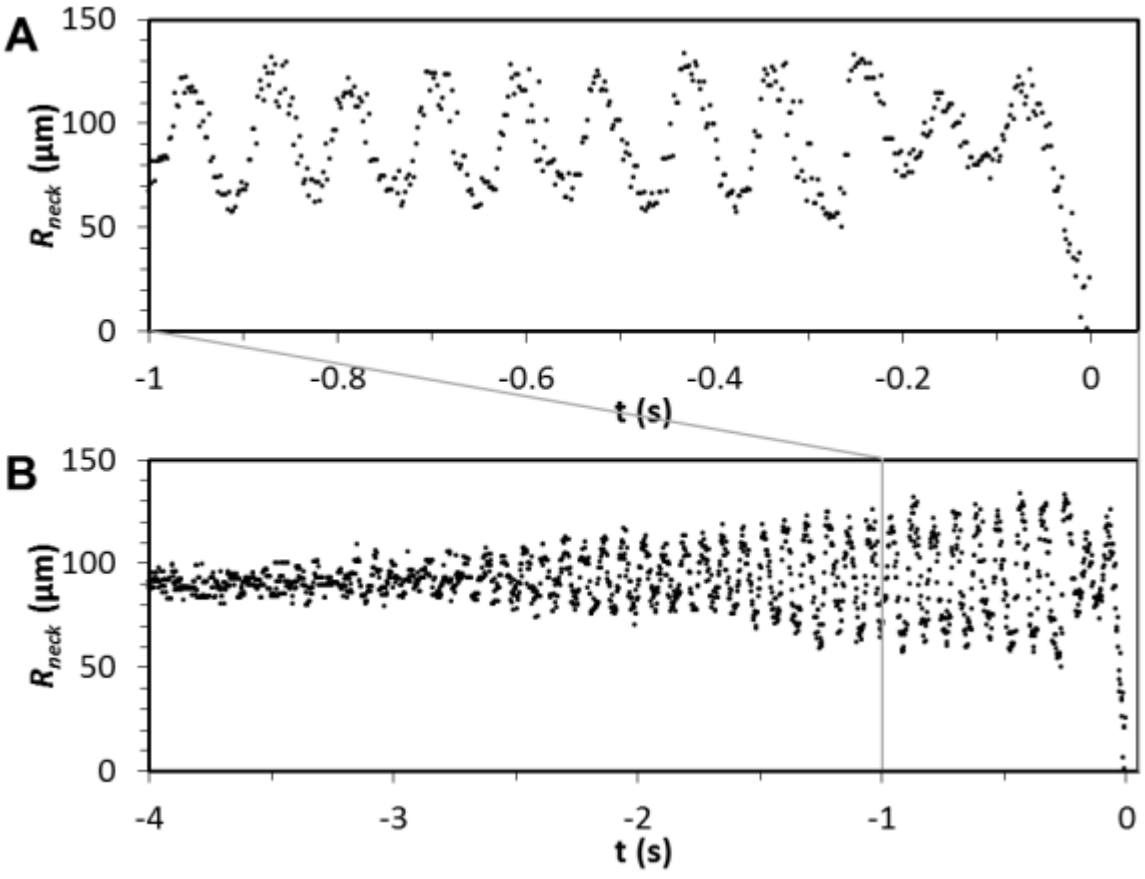

Figure 20. Radius of the thread at a fixed point with respect to the droplet in time. Data is from the same movie as the snapshots from figure 19. **A** Zoom in on the last second before breakup (at 0 s) of **B** the thread oscillating with increasing amplitude.. Velocity v_0 is 23.6 mm/s.

In the widening jet regime oscillations have been reported similar to our experiments (Utada et al. 2008, Zhou et al. 2006), or as fluctuations in a co-flow system with low interfacial tension (Sauret et al. 2012)

A clear difference between experiments with the upward or tilted microfluidic set-up is observed with respect to the amount of wobbles. More wobbles were observed in experiments with the tilted set-up (5 - 20 wobbles) than with the upward set-up (1 - 4 wobbles) and were observed typically more than 3 seconds, whereas the duration of one complete liquid thread event is typically 0.5 - 5 minutes. For the upward microfluidic setup only a few wobbles could be identified.

Figure 21 shows the frequencies of the wobbling liquid thread on a fixed point close to the droplet. Inner fluid viscosity was silicone oil 350 and outer fluid was 1% tween20. The data points are between 10 and 15 Hz, and indicate constant frequencies for different velocities v_0. These frequencies may depend on certain fluid properties, however probably not on viscous shear inside the fluid thread.

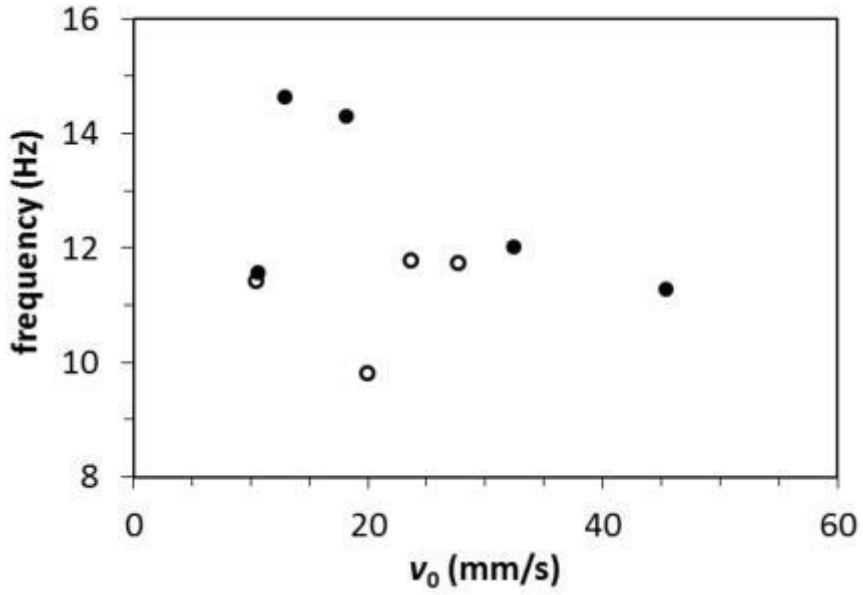

Figure 21. Frequencies of oscillations at different v_0 of the inner fluid though the liquid thread. (○) data from experiments with ceiling and (●) data from experiments without ceiling.

The wave lengths of the wobbles were measured and plotted in figure 22. A linear correlation is observed for the laminar flow regime. Viscous shear forces straighten the wobbles, because axial velocity is higher when the radius is smaller.

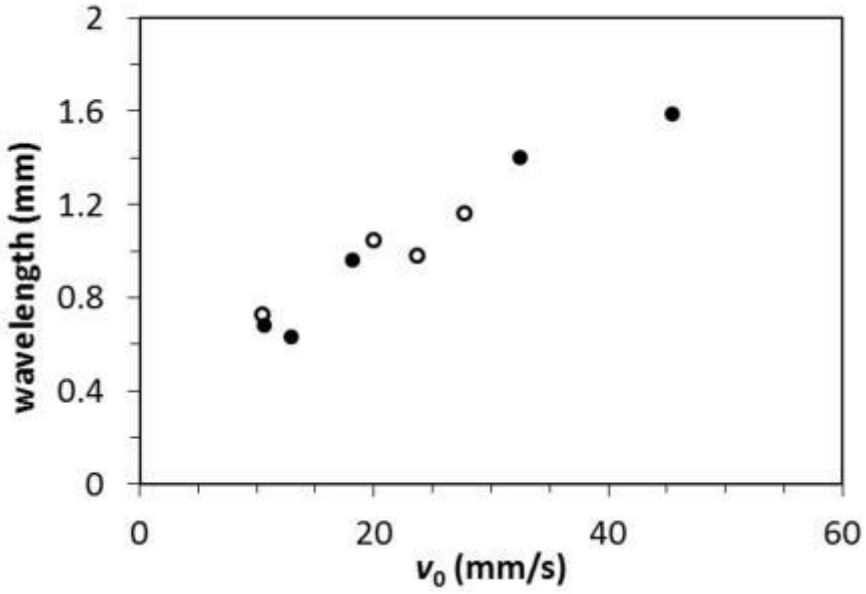

Figure 22. The wavelengths of oscillations at different v_0 of the inner fluid though the liquid thread. (○) data from experiments with ceiling and (●) data from experiments without ceiling.

The amplitude of the wobbles increases in time while looking at the thread at a fixed point from the droplet (figure 20).

The oscillation may be seen as instabilities, which grow towards the droplet. The velocities of the wobbles can be estimated from the frequencies (figure 20) and wavelengths (figure 22) and are about 1.3 – 2.5 times slower than the initial velocities v_0. However, the wobbles are observed closer to the droplet where the radius of the liquid thread is 1.2 – 1.5 times larger than R_0. The corresponding velocity in the liquid thread (and at the interface in free surface flow) is 1.5 – 2.3 times lower and thus in range of the velocities of the wobbles. The instability is assumed to be absolute since the

velocities of the wobbles move at similar velocities as the interface of in the liquid threads.

Breakup of a (confined) liquid thread is inhibited as seen chapter 2 and 3 due to the internal viscous shear stress. However when at the critical velocity a liquid thread is formed inside the capillary, this liquid thread is seemingly also in free surface flow condition and oscillations can also be observed. More research is needed to understand the potential similarities between auto breakup and breakup in free surface flow (see also chapter 6).

4. Conclusions

The shape of liquid threads, between a droplet and a nozzle, can be predicted accurately by a simplified Navier-Stokes based ordinary differential equation (ODE) assuming steady state, axisymmetric and fluid velocity averaged over the cross section. The driving force to stabilise the liquid thread is a pressure gradient $Q = Q_0/L - Q_1$, which includes the applied pressure gradient between droplet and nozzle Q_0 over thread length L and Q_1 as the dissipation of energy via shear at the interface to the outer fluid. The maximum thread length is predicted to be reached when Q goes towards 0 as the ratio Q_0/Q_1. Perturbations observed in the liquid thread as oscillations close to the droplet probably follow from an absolute instability.

Chapter 5

Emanating liquid jet after droplet impingement on a liquid surface

Abstract

The study on the phenomenon of a liquid jet, which appears after the impact of a droplet on a liquid surface, is presented. An inertial deceleration dependent Young-Laplace equation is introduced that was experimentally verified for different fluid viscosities and surface tension values. Droplets growing on the tip of these jets have an initial size related to the inertial deceleration of the jet. The shape of the jet can be derived from the inertial deceleration dependent Young-Laplace equation and seems universal.

1. Introduction

A droplet that drips in a deep water bath creates various interesting phenomena. The droplet can coalescence with the surface, or splash by forming a crown with in the middle an emanating jet (figure 1) (Worthington 1882, Worthington & Cole 1900). The droplets that are formed on the tip of the jet can detach from the jet from the first rise above the liquid surface up to the last moment of descend to the liquid surface (Rein 1993, 1996; Yarin 2006).

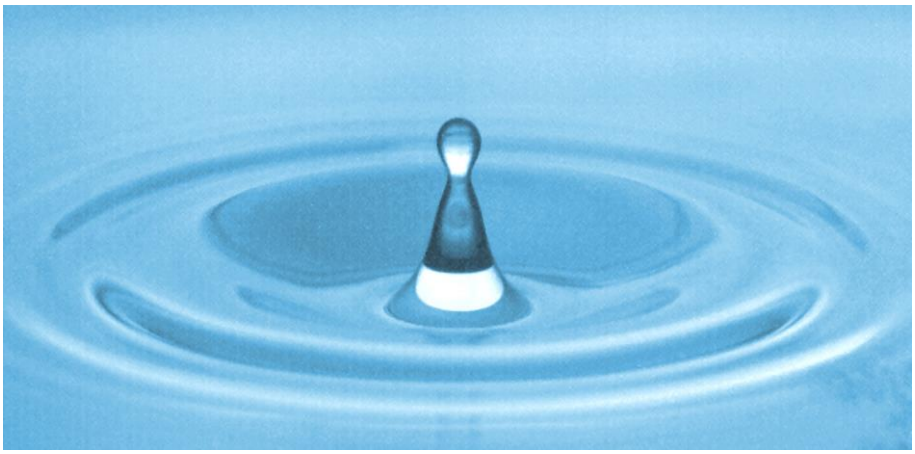

Figure 1. Snapshot of a water jet emanating from a water surface (FASTCAM miniUX100 with shutter time 25 μs). The base of the jet has a diameter of 5.5 mm, and the diameter of the droplet on top of the jet is 1.48 mm.

A short schematic description of an emanating liquid jet rising from a liquid surface is depicted in figure 2. A crater is formed in the liquid surface after droplet impact (figure 2B). Liquid walls fall back and collapse in the middle of the crater (figure 2C). A liquid jet rises from the surface (figure 2D).

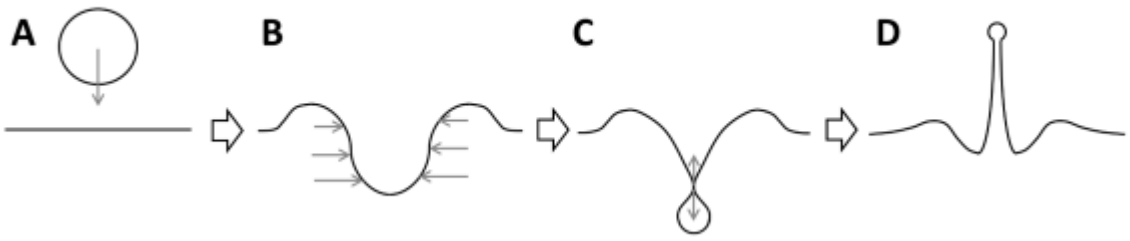

Figure 2. Schematic representation of different formation stages after impact of a droplet that lead to a liquid jet with a droplet on top rising from the water surface.

In this chapter in particular the shape of a rising jet after droplet impingement is studied. The liquid jet above the water surface immediately reshapes itself by a balance of two place dependent forces/pressures originating from surface tension only. These forces/pressures are manifested as a pressure from inertial deceleration of the liquid jet through retraction of the jet towards the liquid surface and an increasing Laplace pressure upward in the jet direction. The shape of the liquid jet is determined by the balance of these pressures and is verified by experimental data.

1.1. Coalescence and splash after impact of a droplet on a liquid surface

The impact of a droplet on a liquid surface can either result in coalescence or in a splash. Coalescence is when the droplet merges with the liquid surface. A splash is when the crater collapses and results in a liquid jet rising from the centre and/or crown of fluid spreading upwards and outwards from the crater. The transition from coalescence to a splash cane be defined as when droplets start to emit after impact (Rein 1993). Four splash regimes have been distinguished by the observed splash and central jet phenomena (Zhao et al. 2011). A threshold defines the transition between coalescence and a splash by the kinetic energy of impact (Manzello & Yang 2002, Rodriguez & Mesler 1985). Coalescence can be characterised by low kinetic energy and a splash by high kinetic energy. The threshold was modelled in empirical models by using several dimensionless parameters: Weber number *We*, Ohnesorge number *Oh*, Froude number *Fr*, and Reynolds number *Re* (Huang & Zhang 2008, Manzello & Yang 2002, Rein 1993).

These empirical models have been developed further and applied for fluids with different viscosity η, density ρ, and surface tension γ (Zhao et al. 2011).

The impact of a droplet on a liquid surface brings fluid in motion below the liquid surface. This fluid motion is observed as a vortex ring in which the motion is in the shape of a torus just below the crater. However, this vortex ring is not always observed. Either a central jet, or a vortex ring will occur (Rein 1993).

1.2. Liquid jet formation emanating from the liquid surface

The jet can be formed when a droplet impinges on a liquid surface. Another way to generate an emanating liquid jet is by pulling a plate from the surface of a liquid into the bulk fluid. The cylindrical shaped crater collapses in the middle with a hole below the surface where the liquid walls of the crater meets in the collapse. The collapse generates liquid jets both upwards and downwards in the entrained bubble (Gekle & Gordillo 2010, Gekle et al. 2009, Gordillo & Gekle 2010). The collapse of a crater can also be initiated from standing waves in a central point. An air bubble is entrained upon the collapse of the standing waves with an amplitude above a critical height of the standing waves. A singularity in the collapse of the waves was found in the bottom of the crater depending on its depth (Zeff et al. 2000). The acceleration in fluid displacement was calculated to exceed $10 \cdot g$ (Longuet-Higgins 2001).

Supersonic liquid jets, with speeds up to 850 m/s, can be generated by focussing a laser pulse on a liquid in a capillary. The experimental results could be accurately described by numerical simulations (Peters et al. 2013).

1.3. Droplet jetting and pinch-off from an emanating jet

An emanating liquid jet from a liquid surface has at its tip initially a spherical cap that might grow to a droplet, since that is the most favourable shape (see chapter 1). Low viscous fluids may form thin tiny jets which grow very fast in time, characterized by a high initial velocity more easily than by using high viscous fluids.

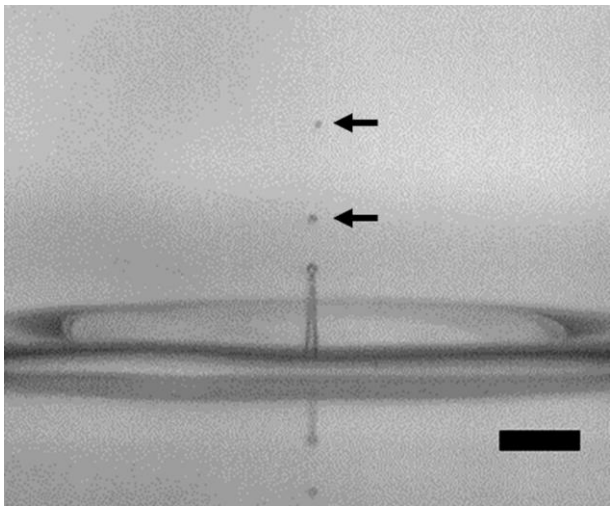

Figure 3. Snapshot of initial rise of a liquid jet (initial velocity is 0.96 ms after appearing above the surface) emitting small droplets. The arrows mark tiny droplets that are released from the liquid jet. Fluid is water and initial velocity is 2 m/s. Scale bar represents 2000 µm. The camera is a FASTCAM mini UX100.

Many droplets may detach from the liquid jet in the first moments of rising, as seen in Figure 3. (Rein 1996, Yarin 2006). These droplets are typically very small and are released from the liquid jet with high speed (Marston & Thoroddsen 2008). Breakup of these droplets are assumed to follow the Rayleigh breakup principle (Hogrefe et al. 1998), a convective mechanism based on downstream propagation of wavelengths in a cylindrical shaped fluid as explained in chapter 1.

In the further rise of the liquid jet, droplets emit from the liquid jet (see examples in Figures 4-7) and are assumed to follow a pinch-off mechanism (Gordillo & Gekle 2010), also denoted as a capillary pinch-off mechanism (Stone & Leal 1989). The trigger for breakup is found to be absolute due to the deceleration of the tip of the jet, which induce local corrugations on the liquid jet (Gordillo & Gekle 2010).

2. Materials and methods

Experiments were done at ambient atmosphere at 24 °C. A petri dish (diameter 146 mm, height 18 mm) was completely filled with an aqueous solution. Viscosities η, interfacial

tensions γ, and densities ρ of the different aqueous solutions are listed in table 1. A syringe was placed over the centre of the petri dish at a certain distance. From this syringe a droplet, of the same aqueous solution as in the petri dish, was generated with a radius of about 2.2 mm. The distance between syringe and surface defines the impact velocity of the droplet, which was in the range of 1.0 to 3.1 m/s.

The impact of the droplet on the liquid surface and resulting rise and fall of a jet was recorded with a high speed camera (FASTCAM Mini UX100) at a frame rate of 8000 fps (frames per second) and resolution of 1280 x 616 pixels. The recorded images were processed by computer software ImageJ and Matlab. The procedure of processing the images is more extensively described in appendix A.

Table 1. Physical properties, viscosity η, surface tension γ, and density ρ, of fluids used in experiments at 24 °C (Dorsey 1940, Gallant 1967).

	η (mPa·s)	γ (mN/m)	ρ (kg/m^3)
Water	0.9	72	998
60 (*wt*)% glycerol	9.1	67	1155
78 (*wt*)% glycerol	45	65	1204
~1 (*wt*)% tween20	1	34	998[a]

[a] The density is assumed to be very similar to water.

3. Results and discussion

3.1. Observations of a rising liquid jet

The fluids used for the experiments mainly differ in viscosity and interfacial tension (see table 1.). Series of snapshots in the figures 4, 5, 6, and 8 shows different shapes of the liquid jet. In general, the shape of the liquid jet is tapering with a concave profile. The tip of the liquid jet is capped with a growing droplet.

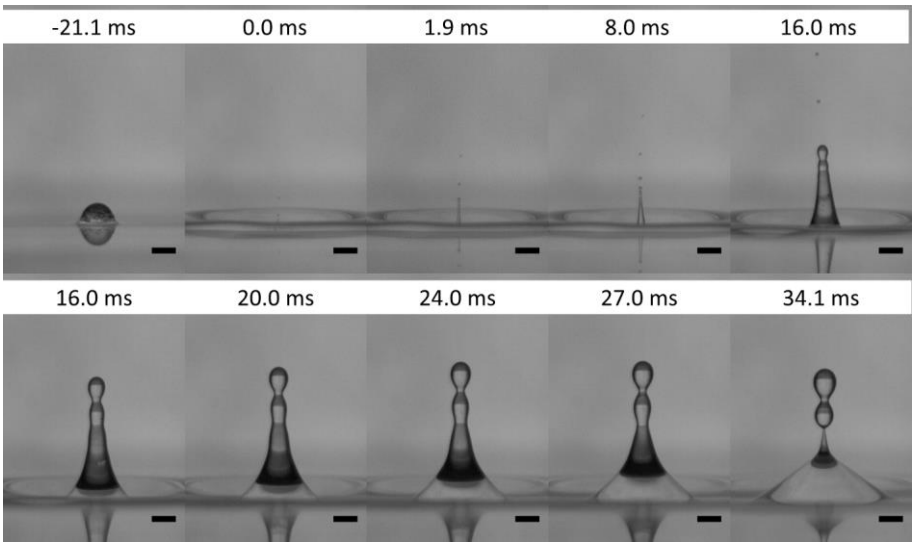

Figure 4. Snapshots of liquid jet formation after impact of a water droplet (high surface tension and low viscosity). Falling droplet has 1.30 mm radius with 2.16 m/s impact velocity. Scale bars are 2000 μm.

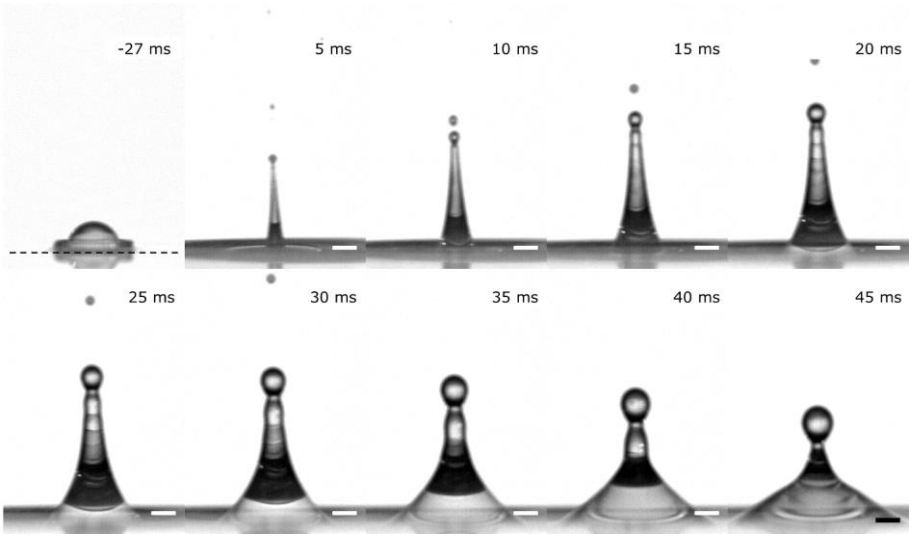

Figure 5. Snapshots of liquid jet formation after droplet impact for 60% glycerol in water (high surface tension and higher viscosity). The dashed line marks the initial position of the liquid surface. The jet is result of an impact of a droplet of 2.29 mm radius with 1.10 m/s impact velocity. Scale bars are 2000 μm.

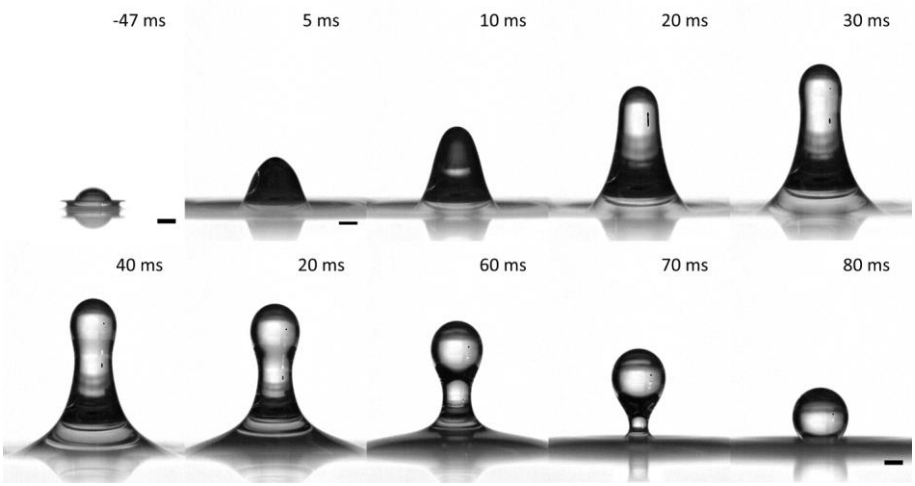

Figure 6. Snapshots of liquid jet formation after droplet impact for 78% glycerol (high surface tension and high viscosity). The jet is result of an impact of a droplet of 2.06 mm radius with 3.13 m/s impact velocity. Scale bars are 2000 µm.

In figures 5 and 6 is shown that viscous effects can be qualitative. Liquid emanating jets of water (0.9 mPa·s) (figure 4) seem thinner, followed by the jets of 60% glycerol (9.1 mPa·s) (figure 5). The emanating jets of 78% glycerol (45 mPa·s) (figure 6) are broader with a larger droplet on its tip than observed from the liquid jets of a lower viscosity. Furthermore, the surfaces of the 78% glycerol jets are smooth without fast growing instabilities in the jet itself.

A liquid jet with high viscosity is reaching a lower height H_{max} (apex) with similar impact energy than liquid jets with low viscosity (see figure 7). We assume that viscous shear hampers the formation of a thin initial jet with a high initial velocity rising from the surface. The speed of the collapse of the crater is determined by the viscosity of the fluid.

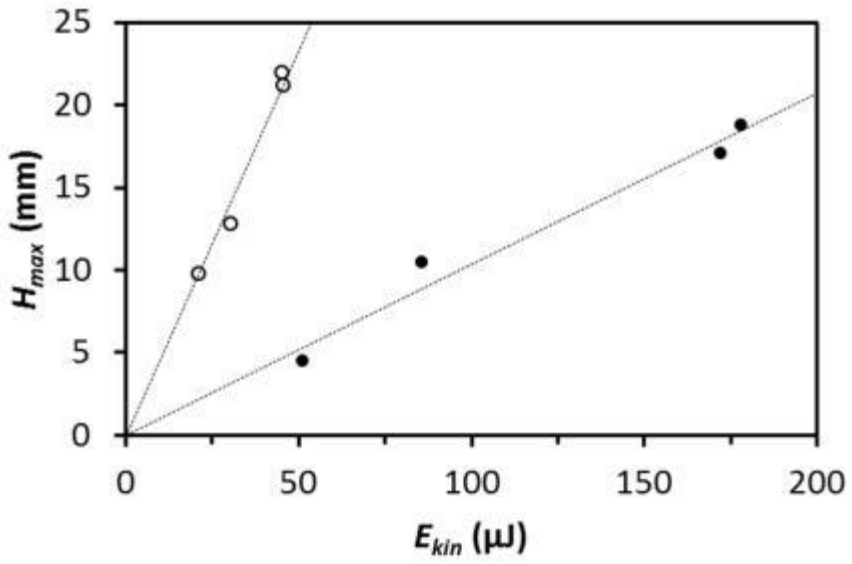

Figure 7. The height H_{max} of the liquid jet at the apex depends on the impact energy of a droplet on the liquid surface. (○) 60% glycerol and (●) 78% glycerol. Lines are linear guides to experimental data points. The slope of the lines suggests that more E_{kin} from the impact droplet is needed to generate a high liquid jet for more viscous fluids.

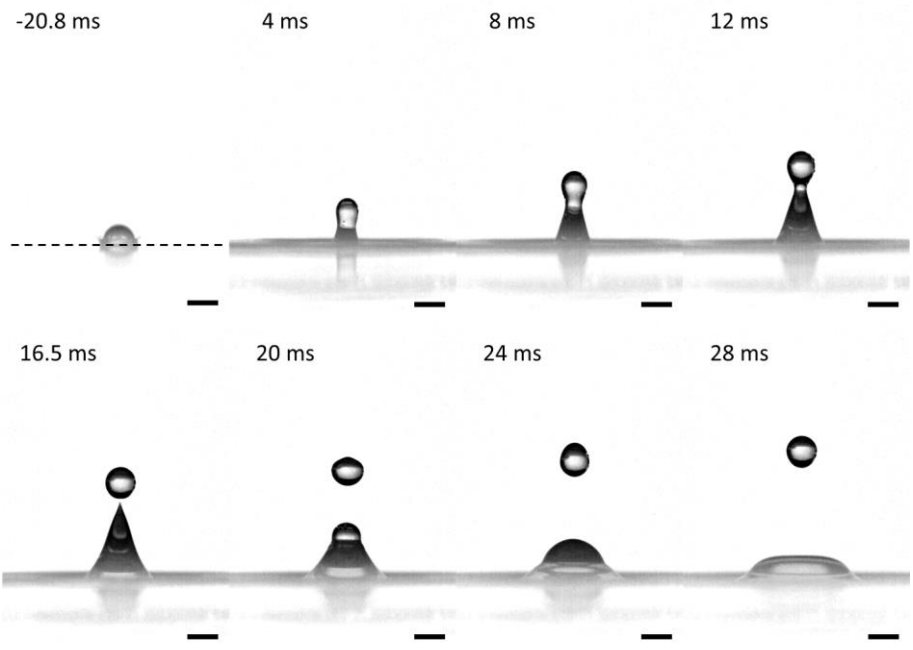

Figure 8. Snapshots of liquid jet formation after droplet impact for ~1% tween20 (low surface tension and low viscosity). The dashed line marks the initial position of the liquid surface. The jet is generated by the impact of a droplet of 1.0 mm radius with 2.25 m/s impact velocity of the liquid surface. Scale bars are 2000 μm.

The shape of the liquid jet seems to be close to a straight cone for an aqueous solution containing about 1% tween 20 (figure 8). The difference in shape, with respect to the other aqueous solutions, can be explained by a lower surface tension, and possibly also to an unequal distribution of surfactants on the surface of the emanating jet (Eastoe & Dalton 2000). Tween20 (1227.5 g/mol) is a relative large surfactant molecule and its redistribution on a fast changing surface is assumed to be slow. However, we have been able to fit also these jets with our model (see figure 13 in section 3.4.3), which suggests that the dynamic effects of the surface tension can be neglected for the shape of the liquid jet in figure 8.

3.2. Deceleration during rise of a liquid jet

The liquid jet that rises after droplet impact is still connected to the liquid surface at the base of the crater. The jet rises with an initial velocity v_0 in the order of m/s, but is assumed to be dependent on viscosity of the fluid and dimension of the collapsing crater; v_0 = 3 m/s in the example of figure 5.

The evolution of the emanating liquid jet can be determined by following the height of the tip $H(t)$ as depicted in figure 8A. During the rise of the liquid jet, droplets are released at t = 1.3 ms and 7.8 ms. The release of the droplet at t = 7.8 ms can be noticed in the $H(t)$ trajectory since the jet height drops after the release of the droplet (see figure 9A). During the fall of the liquid jet, at t = 51.0 ms a third droplet is released (see also figure 14).

The total deceleration $a(t)$ can be derived from this $H(t)$ trajectory by determining its second derivative and follows from:

$$H(t) = v_0 t - \int_0^t a(t) t \, dt \tag{1}$$

Here, v_0 is the initial velocity of the jet as recorded above the fluid surface.

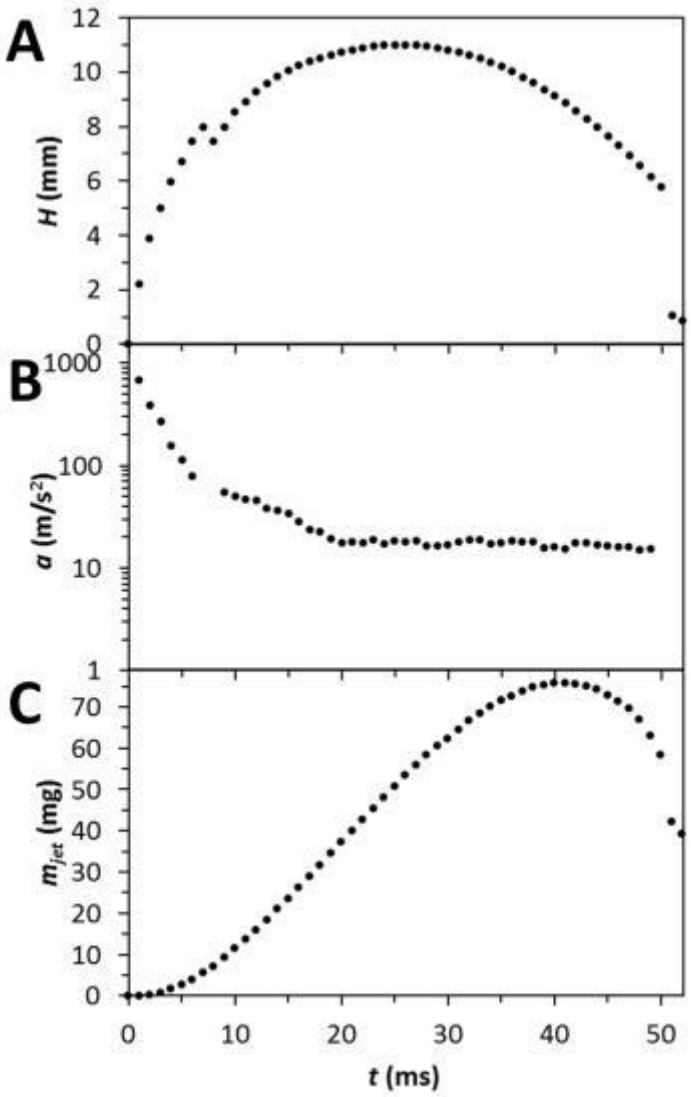

Figure 9. The evolution of a 60% glycerol jet is plotted in three plots as function of time. **A** The height of the jet $H(t)$ is plotted, Initial velocity v_0 is 3.0 m/s. **B** Plot of total deceleration $a(t)$ of the tip as derived from $H(t)$. After the apex point (time frame at 25.4 ms) $a(t)$ reaches a nearly constant value. **C** Plot of the total mass of the jet m_{jet} above the liquid surface.

The trajectory of $H(t)$ is an asymmetric parabolic curve. The values of $a(t)$ are determined from $H(t)$ via a numerical method and smoothened in order to compensate for amplified errors. The trajectory of $H(t)$ is asymmetric around the apex H_{max}. For $t >$ 25 ms the trajectory has a constant total deceleration of $a(t)$ = 17±2m/s^2. The obtained values of $a(t)$ are always more than g = 9.81 m/s^2.

The difference in the total deceleration $a(t)$ is denoted as:

$$d(t) = a(t) - g \tag{2}$$

The difference is the inertial deceleration $d(t)$ originating from the retraction of the liquid jet towards the liquid surface. The inertial deceleration $d(t)$ is not constant in time during rise and fall of the liquid jet. A fast decline in $d(t)$ is observed in the first ms, from more than 100 m/s^2, towards a nearly constant value after 20 ms of 8±2 m/s^2. Possibly quasi steady-state approximation can be assumed to be appropriate for at least the latter stage of the rise and fall of a liquid jet.

3.3. Physical origin of the deceleration of a liquid jet

Here, understanding the physical origin of $d(t)$ is approached by looking more closely at the surface tension based retraction of the jet towards the bath. The circumference of the jet at height h has value $2\pi R(h)$ and exerts a pulling surface tension force $F_{st}(h)$ with a force component directed along the axis of the jet: $F_{st}(h) = 2\pi R(h)\gamma \cos\big(\theta(h)\big)$, with $\theta(h)$ being the local inclination angle. $F_{ax}(h)$, the axial component of F_{st}, will act on all the mass of the jet between h and H including the droplet and with this induces a downward inertial deceleration $d(t)$. Although the liquid jet is continuously connected to the liquid surface, all m_{jet} (Figure 9C) above the fluid surface is subject to a free fall. Gravity plays therefore a minor role: if this jet mass would not be connected to the liquid it would reshape itself in a spherical droplet with a form not determined by gravity. Viscous effects can also be neglected. Initial jet velocities v_0 are typically considerable large (1-10 m/s), but the velocity field differences inside the fluid δv_i are small (up to 0.4 m/s). These δv_i indicate that viscous effects can be neglected in both axial and radial directions as shown in table 2.

Table 2. Axial and radial velocity field differences δv_i and corresponding viscous shear pressures $p_{viscous}$, jet radius at the base and tip, and corresponding approximated Laplace pressure $p_{Laplace}$ estimated from jets of different fluids.

Axial direction

	At base				At tip			
	R_{base} (mm)	δv_i (m/s)	$p_{viscous}$ (Pa)	$p_{Laplace}$ (Pa)	R_{tip} (mm)	δv_i (m/s)	$p_{viscous}$ (Pa)	$p_{Laplace}$ (Pa)
Water	2.6	0.21	0.08	28	0.45	0.20	0.45	160
60% glycerol	2.0	0.21	0.94	34	0.50	0.37	6.72	134
78% glycerol	5.0	0.11	0.97	13	2.1	0.12	2.47	31
~1% tween20	1.2	0.40	0.33	28	0.49	0.29	0.60	69

Radial direction

	At base				At tip			
	R_{base} (mm)	δv_i (m/s)	$p_{viscous}$ (Pa)	$p_{Laplace}$ (Pa)	R_{tip} (mm)	δv_i (m/s)	$p_{viscous}$ (Pa)	$p_{Laplace}$ (Pa)
Water	1.5 – 5.9	0.11	0.07	12 – 47	0.4 – 0.5	0.020	0.05	140 – 190
60% glycerol	2.7 – 6.2	0.11	0.38	11 – 25	0.3 – 0.5	0.016	0.56	140 – 240
78% glycerol	4.1 – 5.8	0.07	0.75	11 – 16	2.1 – 2.2	0.014	0.29	30 – 31
~1% tween20	0.8 – 2.5	0.08	0.10	14 – 42	0.3 – 0.5	0.019	0.07	71 – 120

The values for δv_i have been calculated in the radial direction as change in radius in time for both at the tip and at the base. The δv_i in axial direction are calculated from the flow rate through a cross section. From table 2 it can be seen that axial velocities are substantially larger than the radial velocities. The effect of viscosity is expressed in table 2 by viscous pressure $p_{viscous}$:

$$p_{viscous} = \frac{\eta v}{R} \tag{3}$$

Here, the radius of the liquid jet R can be R_{base}, at the base of the liquid jet or, R_{tip}, at the tip of the liquid jet. These $p_{viscous}$ are 10-100 times smaller than internal pressure from surface tension $p_{Laplace}$ as approximated by the relation:

$$p_{Laplace} = \frac{\gamma}{R} \tag{4}$$

The dominant force during the rise and fall of the liquid jet is therefore associated with the surface tension γ.

The axially oriented surface tension force F_{st} of a liquid thread with radius R is defined as the circumference of the connecting radius times the surface tension:

$$F_{st}(h) = 2\pi R(h)\gamma \cos\theta_{base} \tag{5}$$

θ_{base} is the inclination angle between the axe of the liquid jet and the liquid jet at the base. The tensile force F_{St} works against the formation of more surface area and will act on all the mass of the liquid jet m_{jet} (figure 9C) between its base and tip of the jet.

Equation (5) applies to the complete liquid jet. The force F_{St} pulls back the liquid jet to the liquid surface and is balanced by the inertial force according to Newton ($F = m_{jet}d(t)$):

$$d(t) = \frac{2\pi R_{base}\gamma \cos\theta_{base}}{m_{jet}} \tag{6}$$

with R_{base} is the radius of the base of the jet.

The $d(t)$ calculated according to equation (6) from experimental data is plotted (■) in figure 10.

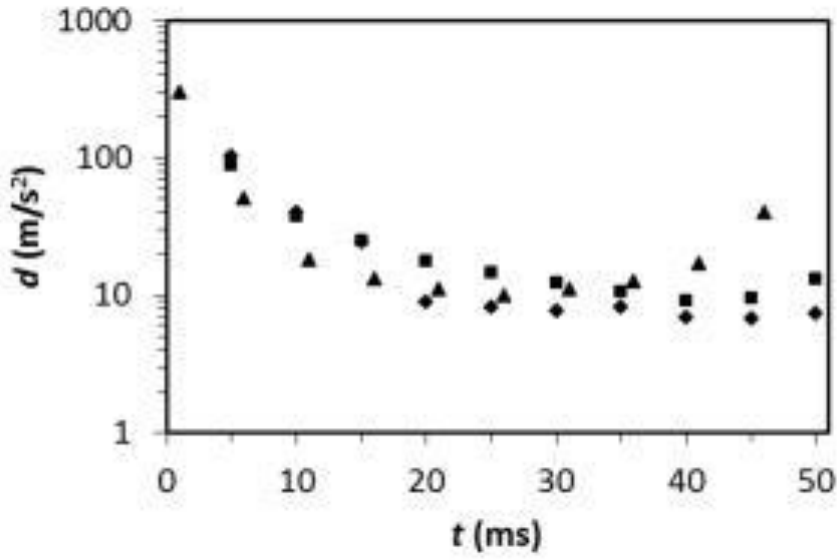

Figure 10. Threefold plot of deceleration $d(t)$. (♦) Deceleration $d(t)$ derived from trajectory $H(t)$. (■) $d(t)$ calculated from surface tension force on the liquid jet by equation (6). And (▲) $d(t)$ calculated from the shape of the liquid neck according to equation (11) and (12) (see section 3.4.).

3.4. Shape of the liquid jet

A liquid jet emanating from a liquid surface has a concave conical shape. The liquid jet keeps this shape up to the moment that the jet has reached its apex, and even thereafter. It can be thought that the shape of the liquid jet and its evolution is substantially determined by flow patterns in the liquid below the surface and crater prior to its rise (Manzello & Yang 2002, Rein 1996). However, it was demonstrated that fluid near the jet acquires an vertical upward momentum in a small acceleration zone located around the base of the liquid jet. Further, the shape of the liquid jet was predicted from the flow field at the base neglecting surface tension forces and making use of the slenderness of the jet (Gekle & Gordillo 2010, Gekle et al. 2009).

3.4.1. Theoretical approach of the shape of the liquid jet determined by the curvature of the surface

Here a new mechanism is introduced to explain the jet shape starting from the idea that the jet reshapes itself by forces acting on the inside and on the surface of the jet during its evolution. The effective deceleration $d(t)$ of the liquid jet by curvature of the surface and γ retracts the complete liquid jet towards the liquid surface. This leads to pressure build up at given height h:

$$p_{inertial} = \rho d(t) h \tag{7}$$

Here, $d(t)$ is assumed uniform along the liquid jet and thus h independent. This assumption can be valid since the fluids can be considered as Newtonian and incompressible. According to Pascal's law, a change in pressure in an enclosed fluidic system is transmitted to all fluid in this system. Therefore the change in $p_{inertial}$, by changes in h and in t (or $d(t)$), causes redistribution of fluid in the liquid jet restrained by the curvature of the surface and γ.

The local pressure $p_{Laplace}$ from the surface tension is determined by the curvature $2/R_c(h)$ according to Young-Laplace equation.

$$p_{laplace} = \frac{2\gamma}{R_c(h)} = \gamma\left(\frac{1}{R_1} + \frac{1}{R_2}\right) \tag{8}$$

The mean curvature consists of two principle curvatures: $1/R_1$ and $1/R_2$ (Wikipedia Contributors 2015). The two principle curvatures are the inverses of the two radii, R_1 and R_2, which describe circles that describe a local curvature as shown in figure 11. In axisymmetric systems these two principle curvatures can be described from the radius $R(h)$ of the local circumference described by differential equation (9).

$$\frac{2}{R_c(h)} \equiv \frac{1}{R_1} + \frac{1}{R_2} = \frac{1}{R(h)\sqrt{1+\left(\frac{\partial}{\partial h}(R(h))\right)^2}} - \frac{\frac{\partial^2}{\partial h^2}(R(h))}{\left(1+\left(\frac{\partial}{\partial h}(R(h))\right)^2\right)^{3/2}} \tag{9}$$

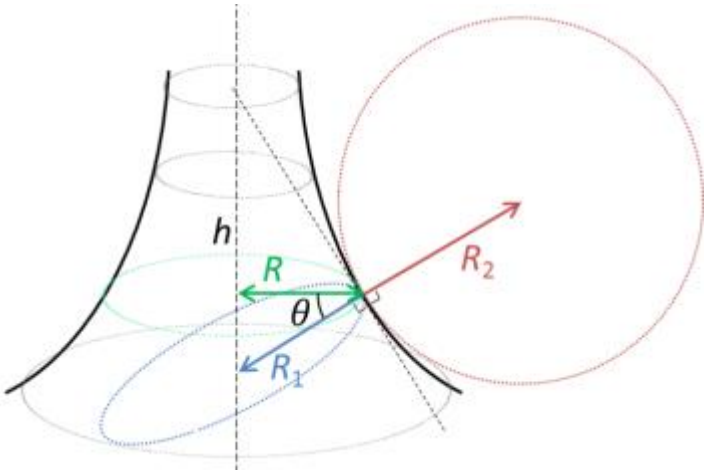

Figure 11. Schematic image of the radii of the two principal curvatures R_1 and R_2.

In steady state the sum of $p_{inertia}$ and $p_{Laplace}$ is zero for every point along h in the liquid jet.

$$\rho d(t)h - \frac{2\gamma}{R_c(h)} = 0 \qquad \text{or} \qquad \frac{R_c(h)}{2} = \frac{\gamma}{\rho d(t)}\frac{1}{h} \tag{10}$$

Equation (10) is mathematically related to the well-known time independent hydrostatic Young-Laplace equation ($\Delta P = \rho hg - 2\gamma/Rc(h)$) valid for the convex shape of sessile drops and is also related to a time independent equation describing the concave shape of the meniscus around a small circular cylinderis for which no analytical solution has been derived (Alimov & Kornev 2014, James 1974).

3.4.2. Approximations to the shape of the liquid jet

An approximate analytical function for equation (10) can be obtained by using a slender jet approximation. In this approximation, the radius of curvature is considered equal to the radius of the jet. The mean curvature $2/R_c$ of a slender liquid jet can thus be estimated as $1/R(h)$:

$$\rho d(t)h - \frac{\gamma}{R(h)} = 0 \qquad \text{or} \qquad R(h) = \frac{\gamma}{\rho d(t)}\frac{1}{h} \tag{11}$$

However, slender jet approximation for the complete jet in the case of a liquid jet emanating from a liquid surface could not be applied adequately.

A more accurate estimation can be obtained by numerically solving equation (10). A numerical inverse function to $R(h)$ is $h(R)$ and can be extended from the slender jet approximation with a polynomial inside an exponential function:

$$h(R) = B^2\frac{1}{R}\left[\mathrm{e}^{-\sum_{i=0}^{n} a_i \left(\frac{1}{B}R\right)^i}\right] \qquad \text{with} \qquad B = \sqrt{\frac{\gamma}{\rho d(t)}} \tag{12}$$

For n = 12 parameters a_i were determined: a_3 = 0.58, a_6 = -0.0265, a_9 = 0.0002, a_{12} = 0.0032, and with other a_i = 0. The parameters a_i are fit parameters, which are needed to fulfil equation (10) with the curvatures $1/R_c(h)$ according to differential equation (9). Equations (12) are time dependent via deceleration $d(t)$. In dimensionless form B = 1 in equation (12) the values are tabled in Appendix B.

3.4.3. Comparison of the shapes of the liquid jets

The shape of a liquid jet according to equation (12) is plotted in figure 12A by the green dashed line in dimensionless form. The shape of the liquid jet by the slender jet approximation (equation 11) is plotted as a red dotted line in figure 12A.

The approximations are validated by numerical calculating the left and right hand side of equation (10) by the values for R and h from the analytical approximations (equation (11), and equation (12)). The values of both sides are expected to be equal and are

plotted in the inset of figure 12A. The inclination of the straight line would be $\frac{1}{B^2} = \frac{\rho d(t)}{\gamma}$ (equation 12), which would be in the order of 10^5 m^{-2}.

For the slender jet approximation, the shape of the liquid jet is in good agreement at large *h*. At lower *h*, however, the jet shape is off as confirmed by the inset in figure 12A. where $h < 2$ the line does not fit to the curvature equation (10). Equation (12) includes a correction at lower *h* and show a better agreement with the curvature equation (10). The two curvatures and its sum could be numerically calculated from approximated $R(h)$ as plotted in figure 12B.

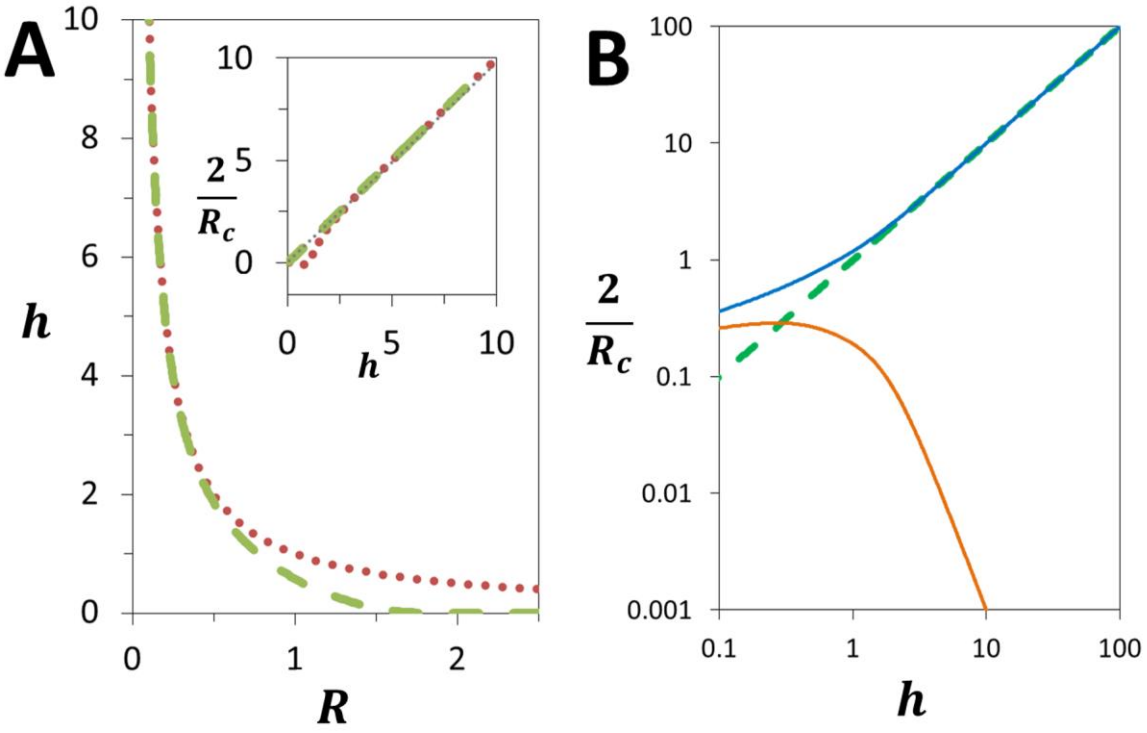

Figure 12. **A** Dimensionless curvature for shape of a liquid jet by (green dashed line) equation (12), and (red dotted line) slender jet appoximation (11). **B** Threefold plot showing curvatures (blue) $1/R_1$ (orange) $-1/R_2$ and (green dashed) the sum $1/R_c$.

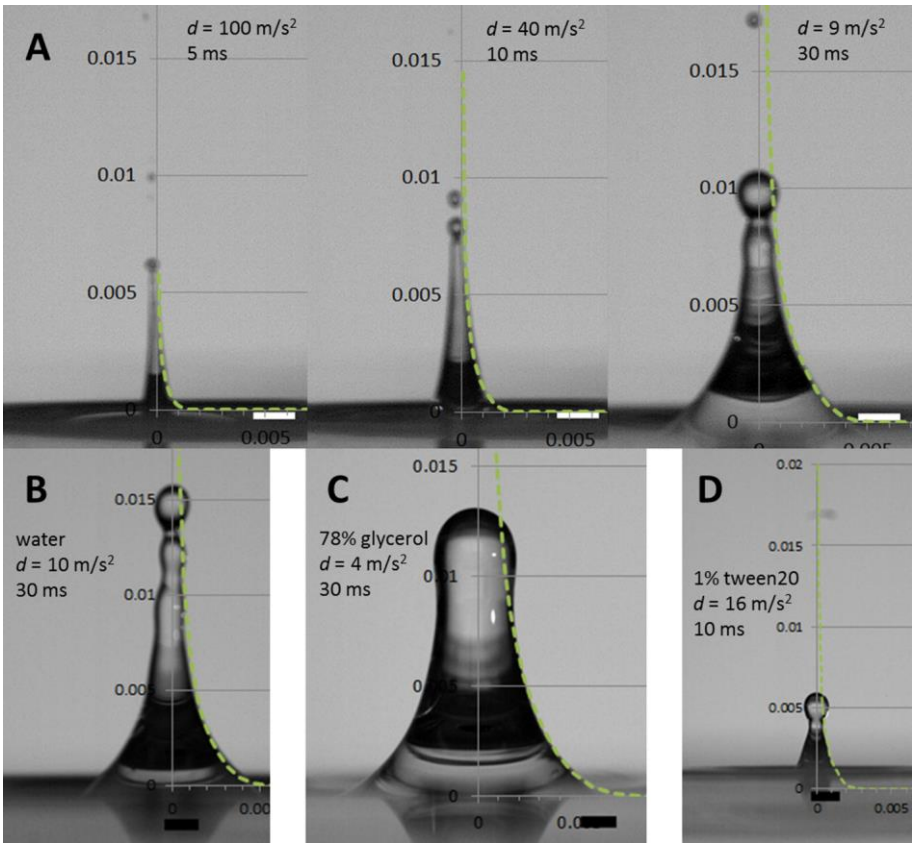

Figure 13. **A** Sequential snapshots with plotted values according to equation (9) for the jet taken from figure 5. 60% glycerol 67 mN/m, 1155 kg/m^3, and **B** snapshot of water, 72 mN/m, 998 kg/m^3 apex at 35.5 ms, **C** snapshot of 78% glycerol 65 mN/m, 1204 kg/m^3 apex at 40.5 ms, and **D** snapshot of 1% tween20, 34 mN/m, 998 kg/m^3 apex at 16.5 ms. Scale bars are 2000 µm.

The approximation of equation (12) has been compared with the experimental data. Equation (12) is fully determined by the physical parameters ρ, $d(t)$ and γ, so no other fitting parameters were needed to compare equation (12) with the experimental data. The parameters a_i are used to fit equation (12) to the differential equation (10) and not to experimental data. The obtained fits follow the shape of the liquid jets very well as depicted in figure 13 and indicate that our hypothesis seems correct.

Actually, $d(t)$ can also be calculated from equation (12) using $d(t)$ as fit parameter to calculate the shape of the liquid jet and to fit this shape to experimental data. Results are shown in figure 10 (▲) and are in good agreement with $d(t)$ derived from $H(t)$ trajectory up to 40 ms.

3.5. Droplet formation on the tip of a liquid jet

The tip of the liquid jet is capped with a half sphere at the start of the rise of the liquid jet. This half sphere becomes a droplet attached to the liquid jet via a neck. Sometimes the neck breaks up and a droplet is launched with the same upwards velocity as the liquid jet.

The droplet on the liquid jet has a radius R_d with a local Laplace pressure: $p_{Laplace} = \frac{2\gamma}{R_d}$. This pressure may be equal to the inertial pressure difference between the base and the tip of the jet. From this, the initial droplet size could be predicted:

$$\rho d H - \frac{2\gamma}{R_d} = 0 \qquad \text{or} \qquad R_d = \frac{2\gamma}{\rho d}\frac{1}{H} \tag{13}$$

The inertial pressure (equation (13) correlates to the Laplace pressure in the droplet as shown in figure 14.

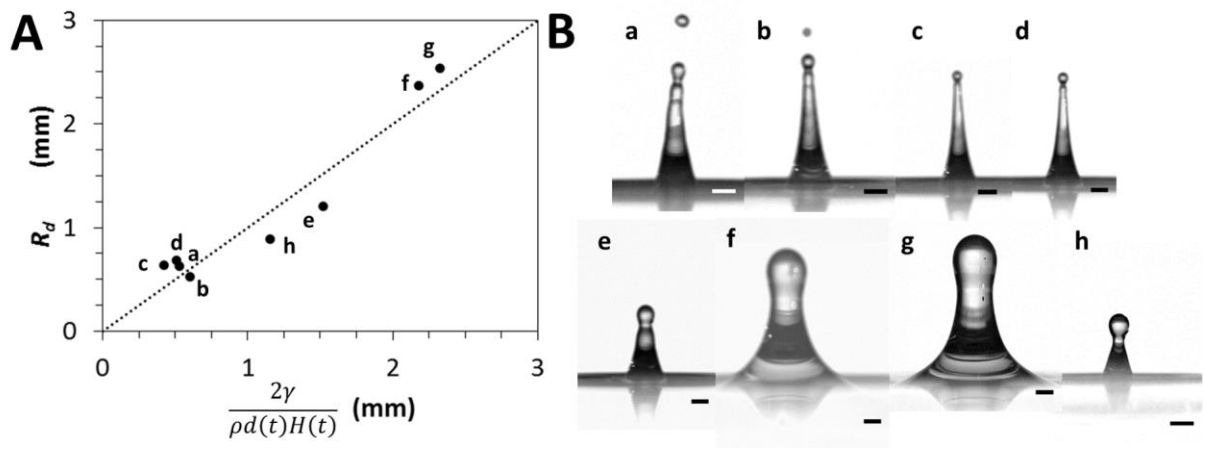

Figure 14. **A** Droplet radii R_d measured from snapshots and calculated from equation (13). The dashed line represents R_d calculated from equation (13). **B** snapshots of liquids jets from eight different movies, which correspond to letters in **A**. Properties of aqueous solutions **a** water, **b**-**e** 60% glycerol, **f**-**g** 78% glycerol, and **h** 1% tween20. Scale bars are 2000 μm.

Droplet breakup from the initial tip rise of the jet is also studied (figure 15). In the first ms of the rise of the jet above the surface, several tiny droplets are launched from the tip with high velocities (figure 3). Droplet radii on top of the liquid jet increase during the rise and fall of the liquid jet, thus these radii change in time.

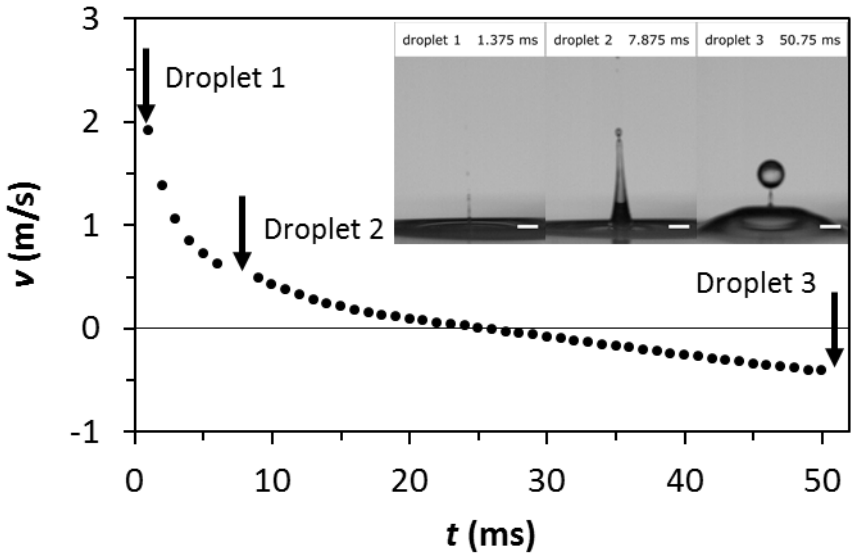

Figure 15. Velocity profile derived from $H(t)$ of the liquid jet. The arrows mark when droplets detach from liquid jet. Snapshots of three droplets on the tip of the liquid jet, just before breakup, were from the same movie as figure 5. Scale bars are 2000 μm.

The first droplet that was clearly recognised to breakup by pinch-off from the liquid jet was at 1.375 ms after rise of the jet above the surface. The second droplet pinched off from the jet was at 8.00 ms. And the third droplet was pinched off after apex at 51.00 ms. Snapshots of pinch-off of the three launched droplets are depicted in figure 14, and derived values are listed in table 3.

Table 3. Parameters of droplets launched from the tip of the jet.

	t_{emit} (ms)	$m_{droplet}$ (mg)	$R_{droplet}$ (µm)	R_{tip} (µm)	$v_{droplet}$ (m/s)	d [a] (m/s^2)
Droplet 1	1.38	0.010	134	80	1.90	39.8
Droplet 2	8.00	0.188	355	150	0.56	23.5
Droplet 3	51.0	11.85	1414	100	-0.40	17.4

[a] values of $d(t)$ have been derived from figure 9B.

Breakup of droplets is determined by the surface tension force F_{tip} (or earlier stated as F_{st} in equation (5)). This force is weakest at the smallest circumference with R_{tip} close to the tip and droplet of the liquid jet:

$$F_{tip} = 2\pi R_{tip}\gamma \tag{14}$$

A droplet with mass $m_{droplet}(t)$ is growing on top of the jet. The shape of the liquid jet is pulling the droplet by its deceleration $d(t)$.

$$F_{droplet} = m_{droplet}(t)d(t) \tag{15}$$

With these formulas (equations (14) and (15)) the minimal R_{tip} is calculated, that is needed to keep the droplet attached to the liquid jet.

$$R_{tip} = \frac{m_{droplet}(t)d(t)}{2\pi\gamma} \tag{16}$$

The R_{tip} derived from various experimental data is plotted in figure 16, as obtained from equation (16).

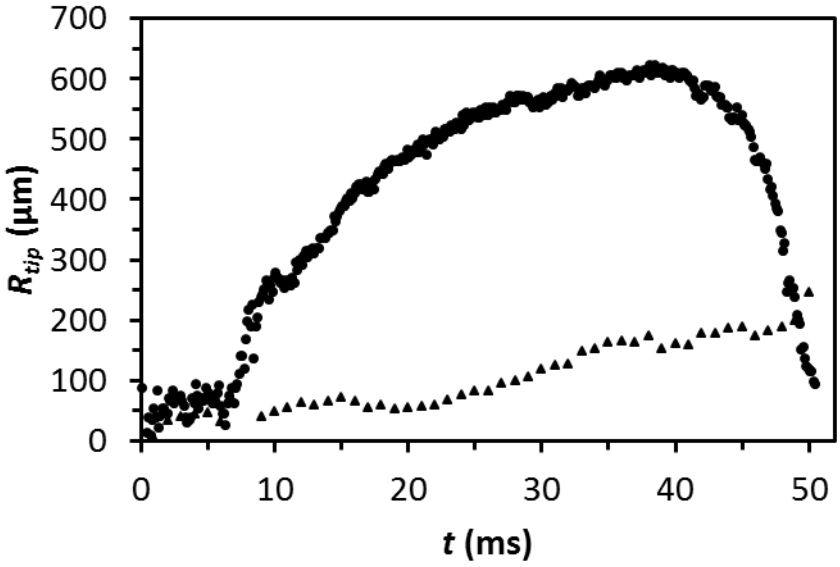

Figure 16. Tip radius R_{tip} in time. (●) Observed from experimental data, and (▲) according to equation (16). The R_{tip} from equation (16) is smaller than the R_{tip} observed until 46.5 ms; after that, the neck is pinched off.

The last stage of breakup is shown in figure 18. A small micro-thread (also denoted as collapsed tip or neck) is formed between droplet and liquid jet. The smallest neck radius R_{tip} is plotted in figure 17 by open circles. This steady decline in R_{tip} follows in the last stage before breakup (snapshots in figure 18) a linear behaviour. This linear behaviour is also seen in pinch-off (Gordillo & Gekle 2010, Stone & Leal 1989), and universal pinch-off (Eggers 1993) and developed further (Brenner et al. 1996) to one of the possible solutions.

$$R_{tip}(t) = S_{min}\frac{\gamma}{\eta}\left(t_{breakup} - t\right) \tag{17}$$

with, S_{min} a scaling function as solutions to a pair of ordinary differential equations in the last stages of universal pinch-off. The value of S_{min} was thought to be 0.0304, however, more solutions are possible by using the approximation by equation (18) (Brenner et al. 1996).

$$S_{min} = \frac{1}{60N - 27} \tag{18}$$

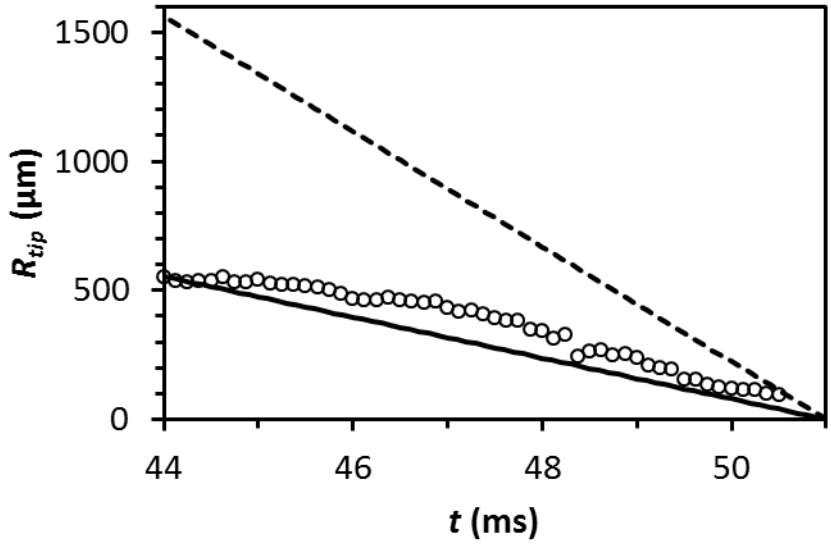

Figure 17. The radius of the tip R_{tip} during last stage of droplet formation. The (○) experimental data show a steady decline in R_{tip}. The theoretical R_{tip} according to equations (17) and (18) fitted by (solid line) N = 2, and (dashed line) N = 1 (Brenner et al. 1996, Eggers 1993).

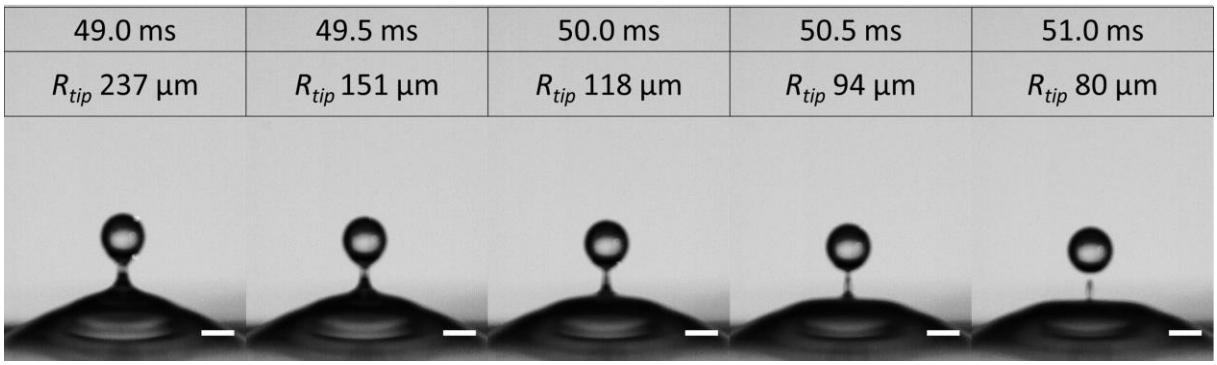

Figure 18. Evolution of tip radius 2 ms before last droplet snap off. A satellite droplet is formed from the micro-thread. Scale bars are 2000 µm.

The experimental R_{tip} gives the best fit (figure 17) when N = 2, and thus S_{min} is 0.0108, as derived from the experimental data from figure 16. In figure 17 the solid line (N = 2) follows the same slope as experimental data. However, to acquire a better fit to the experimental R_{tip}, the fitted time of breakup $t_{breakup}$ may be placed to a time point further than the actual breakup point.

3.6. Broadening of the base of the liquid jet during its descend

The fall of the liquid jet is not the inverse evolution with the rise of the jet. One of the aspects is that the base of the jet keeps broadening. Actually, from figure 9C it can be seen that at 15 ms after the apex point (t > 40 ms) the m_{jet} decreases and jet fluid flows back in the bulk below the liquid surface. The base of the liquid jet broadens influencing the fluid above from a concave cone to a straight cone at around 40 ms further to a convex cone from 45 ms until it disappears in the liquid surface (see figure 19).

The liquid jet is submitted to different fluid dynamics during its rising phase than during its descend phase. From t = 40 ms onwards the jet can be divided in an upper and a lower part. The upper part still has the concave conical shape, while the lower part forms a broad cone. Gravity can become an important parameter as the upper part of the liquid jet, which is still in free fall, is falling directly on the lower part and the liquid surface.

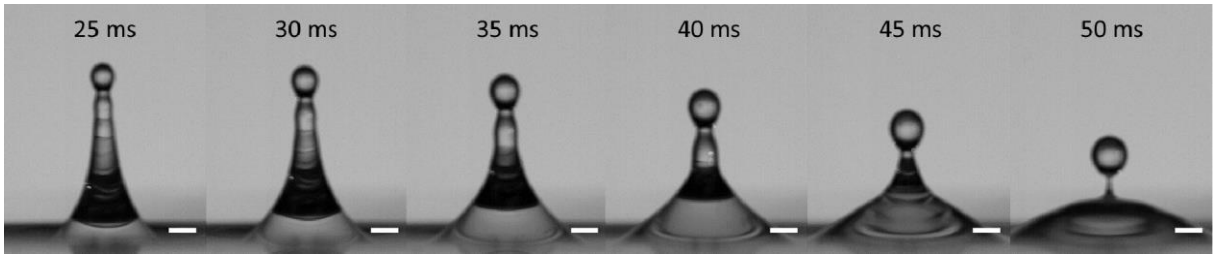

Figure 19. Evolution of the liquid jet after reaching the apex point. The jet experiences at the base a strong horizontally (radially) directed force $F_{ra}(h)$ to broaden the base of the jet. Scale bars are 2000 µm.

The lower part of the liquid jet may resemble a large fluid reservoir that is physically supported by the bulk fluid below the liquid surface. This lower part is then continuously filled with fluid coming from the descending upper part of the liquid jet. This fluid reservoir is concave shaped, which however, is energetically not favourable. Surface tension related forces can drive the shape of the reservoir from concave to

convex. The surface area remains roughly similar, however, holds more volume and is an inverse of the second curvature $1/R_2$.

The driving force for broadening the base of the jet and creating the reservoir can be partly the radial (horizontal) part $F_{ra}(h)$ of the surface tension force $\boldsymbol{F}_{st}(h)$, with value $F_{ra}(h) = 2\pi R(h)\gamma \cos\big(\theta(h)\big)$. The local inclination $\cos(\theta(h))$ between the surface of the jet and the principal axis of the jet increases strongly at the base of the jet. At the base of the jet the radial $F_{ra}(h)$ component becomes rapidly larger than the downward pulling $F_{ax}(h)$ component. Therefore, the uniformity of the inertial deceleration breaks down at the base in the descend phase. Another approach for fluid dynamics at the base of the jet in the descend phase to describe the shape of the fluid seems appropriate.

4. Conclusions

This study shows insight in rise and fall of a liquid jet after impact of a droplet in a deep liquid. The shape of the jet can be explained by surface tension based forces only. The retracting force acting on the jet towards the liquid surface generates an inertial deceleration pressure inside the jet that is balanced by the local Laplace pressure of the jet; these two pressures define the shape of the jet. Furthermore, breakup and size of droplets emitted from the tip can also be explained by this pressure balance. Last stage of breakup appeared to follow universal pinch-off, and micro-thread formation is observed between droplet and liquid jet.

Chapter 6

General discussion

A general overview and discussion of this thesis with a comparison of main results is given in this chapter.

Three fluidic systems with their own fluid dynamics were studied; auto breakup of droplets originating from a special designed capillary to confine a viscous liquid thread, formation of stable viscous liquid threads with the aid of a pressure gradient (viscous flow) along the liquid thread, and free surface emanating jets with accompanying drops.

A potential application is proposed: emulsion polymerisation to obtain uniformly sized particles from droplet formed in the auto breakup regime.

1. General overview of the thesis

The basic objective of this thesis is to provide a better understanding of the fluid dynamics in microfluidic devices for the formation of uniformly sized droplets. The general performance of droplet forming fluidic systems will benefit from methods to control the stability or instability of liquid threads and jets. Three fluidic systems with their own fluid dynamics were studied (figure 1);

- Auto breakup of droplets originating from a confined viscous liquid thread inside a micro-corrugated capillary, which enables passive inflow of the outer fluid, herewith facilitating breakup.
- Generation of stable viscous liquid threads with the aid of a pressure gradient (viscous flow) along the liquid thread to feed a large droplet.
- Free surface emanating jets with accompanying drops growing on top of these jets after impact of an object in a deep liquid.

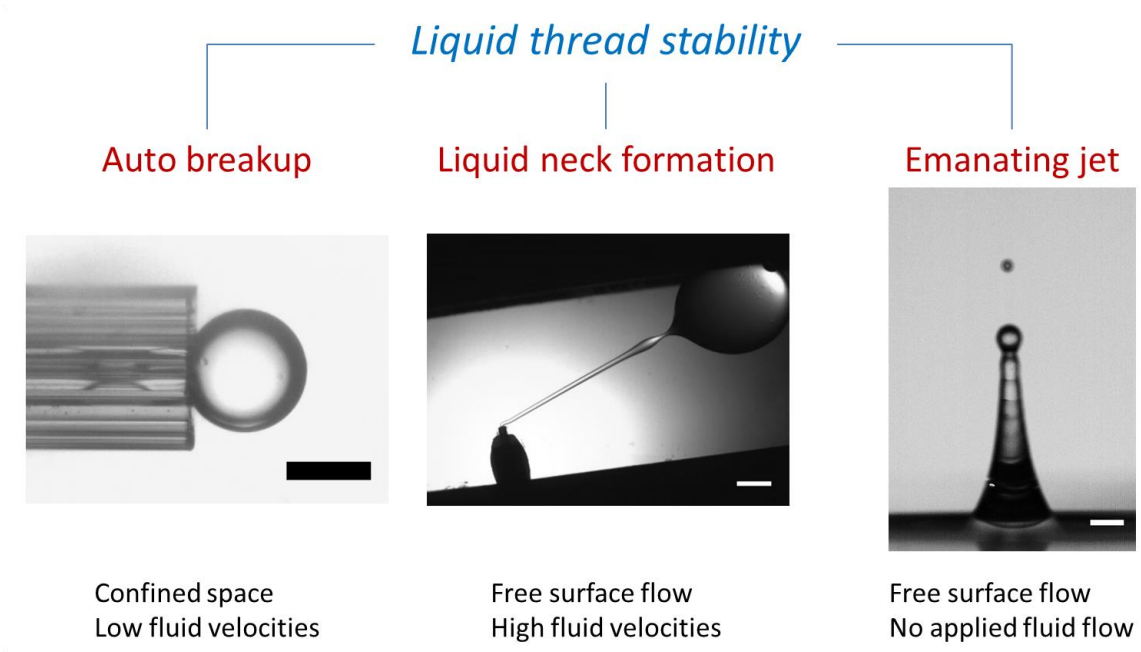

Figure 1. Schematic overview on the three fluidic systems used for the formation of uniformly sized droplets and studying the needed stability of the generated liquid threads and jets. Scale bars are from left to right 200 µm, 2000 µm and 2000 µm.

These three systems are all interlinked by the formation of droplets using a controlled stability or instability of a liquid thread or jet, but strongly differ in how these droplets are obtained (figure 1) with the generation of the corresponding liquid thread or jet.

In the first fluidic system the effect of the inner fluid velocity and its relation to viscous forces is discussed, which turns out to be important for the stability of a confined liquid thread. The liquid thread was found instable at low flow rates and stable at high flow rates. In the second fluidic system the stability and also the shape of a free surface liquid thread is explained, taking into consideration retraction forces, gravitational effects, and energy dissipation by the outer fluid. In the third fluidic system the formation of a free surface liquid is discussed together with the formation of accompanying droplets on top of the jet.

2. Liquid threads stabilised by inner fluid flow

Here we compare the results from the first and second fluidic microfluidic system that we consider. The microfluidic system is a micro-corrugated capillary (cross section depicted in figure 2) allowing the passive inflow of outer fluid inside the capillary. The increase of the inner fluid velocity alters strongly the process of droplet formation as shown in figure 3.

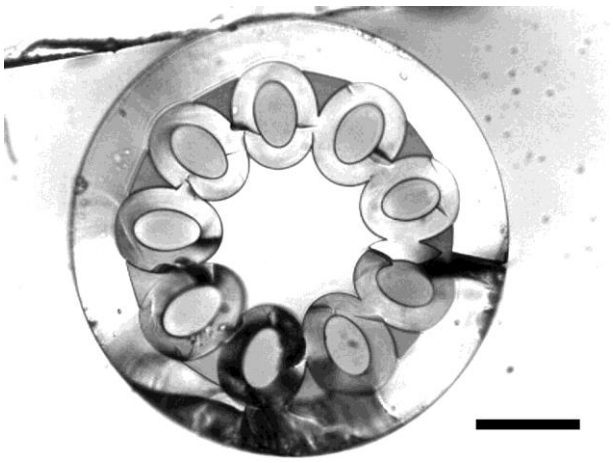

Figure 2. Optical microscopy image of a cross section of a micro-corrugated capillary. The inner radius of the capillary, marked with the dotted circle is 62 μm. Scale bar is 100 μm.

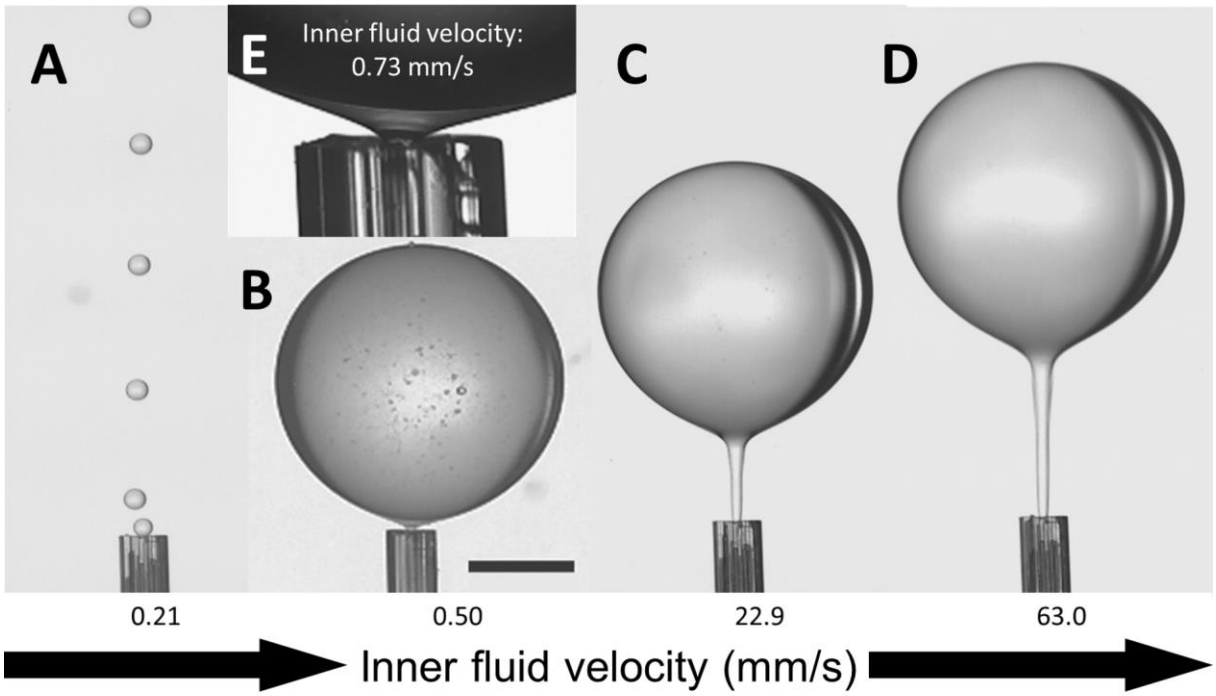

Figure 3. Droplet formation with a micro-corrugated capillary. **A** auto breakup of a confined liquid thread inside the capillary at slow inner fluid velocity (*Re* = $6.69 \cdot 10^{-5}$). **B** auto breakup is hampered and a stable collapsed but still open neck is formed in the liquid thread inside the capillary (*Re* = $1.18 \cdot 10^{-4}$). **C** (*Re* = $7.46 \cdot 10^{-3}$) and **D** at higher inner fluid velocities a stable free surface liquid thread is formed outside the capillary (*Re* = $2.06 \cdot 10^{-2}$). **E** Close-up on the stable collapsed neck with inner fluid velocity through this neck (*Re* = $1.53 \cdot 10^{-4}$). Inner fluid is silicone oil with viscosity 370 mPa·s; outer fluid 1% tween20 with interfacial tension 5 mN/m. Scale bar is 500 μm.

The flow of the inner fluid through the capillary is laminar, because Reynolds numbers are low and viscous forces dominate (*Re* <<10) (Sutera & Skalak 1993). These viscous forces will induce a pressure opposing the squeezing interfacial tension force. Each situation and transition as shown in figure 3 is explained below.

Auto breakup (figure 3A) of the confined liquid thread at the end of the capillary is caused by an interfacial tension driven instability. As long as the actual Laplace pressure of the droplet is higher than the Laplace pressure of the capillary then the inner liquid will be pressed against the corrugations of the capillary. At the moment that the droplet has a size twice the size of the capillary, than the liquid thread is not pressed anymore to

these corrugations near the exit of the capillary. The liquid thread may then become instable and may break up inside the capillary near the droplet provided that an inflow of outer fluid via the micro-corrugations is possible. The inner fluid will however induce along the capillary a viscous pressure difference that is proportional to the fluid velocity of the liquid thread. At a sufficiently low velocity the viscous pressure difference is small enough not to be able to hamper the break-up process. It is anticipated however that when the fluid velocity reaches a certain critical threshold value the breakup process will be prevented and the droplet will keep growing.

Auto breakup may happen thus only at low inner fluid velocities. The transition from the auto break-up regime of an instable liquid thread to a stable liquid thread occurs when the inner fluid velocity (figures 3A) increases, and is related to the acting viscous and surface tension forces. In dimensionless numbers this means that the transition is determined by capillary number Ca (chapter 1), a ratio between the generated viscous pressure and the interfacial tension pressure. A critical capillary number Ca_{cr} is $1/16$ (chapter 3) was derived and experimentally verified. Near the critical capillary number Ca_{cr} we saw that the confined liquid thread can collapse and that a stable neck (figure 2B inset) is formed that prevents further collapse due to a restored balance between the viscous and surface tension forces. The neck may counteract here the squeezing surface tension and will try to maintain a fluid passage.

Above Ca_{cr}, the liquid thread remains stable and fluid flow through the liquid thread keeps filling the droplet. Two other forces may then become significant: a drag force exerted by a possible co-flow of the outer fluid on the droplet, and a buoyancy force caused by a density difference between the inner and outer fluid. Buoyancy goes by the third power of the size of the droplet and the result is an increasing force to pull the droplet away from the nozzle. The only holding force that keeps the droplet arrested to the capillary is the interfacial tension based holding force (van Rijn 2004). Eventually the liquid thread will break-up giving the droplet a specific size, however much larger than twice the size of the inner capillary. The transition from figure 3B to figure 3C and 3D occurs when the capillary number is much higher than Ca_{cr}. The result is that the collapsed liquid neck inside the capillary disappears and the liquid thread is pulled out from the exit of the capillary and becomes a free surface liquid thread. This happens when the buoyancy force becomes larger than the interfacial tension based holding (also

denoted as retraction) force. We remarkably observe that the higher the inner fluid velocity the longer the liquid thread (figure 3C-D) can become before it breaks at its widest point near the droplet.

3. Interfacial tension driven retraction and breakup of liquid threads in free surface flow

It is difficult to judge if the system (figure 3C-D) has reached a force equilibrium, before the liquid thread breaks up outside the capillary. Quasi steady state approximations can only be considered when changes in time of the shape of a liquid thread are sufficiently slow, in that the surface tension forces can come into a (temporary) balance with other forces driving the system. In order to slow down the breakup process and a quasi steady state may be anticipated we have used a tilted ceiling to reduce the buoyancy force.

The axial retraction force F_{st} opposes elongation of the liquid thread (formation of interfacial area) has a magnitude of $F_{st} = 2\pi R\gamma$, with R the radius of the liquid thread near the capillary. When a droplet is formed this force keeps the droplet arrested to the exit of a capillary in the case of auto breakup. For the free surface liquid thread depicted in figures 3B-D, 4 and 7, the retraction force is opposed by the buoyancy force $F_{buoyancy} = \Delta\rho V_{droplet} g$. When the droplet $V_{droplet}$ is large enough the buoyancy force $F_{buoyancy}$ will be larger than the retraction force F_{st} and the droplet disattaches from the capillary and will go upwards to the ceiling. The liquid thread between the capillary exit and droplet will breakup (figure 3B) or grow (figures 3C-D) depending on the magnitude of the pressure gradient Q (chapter 4).

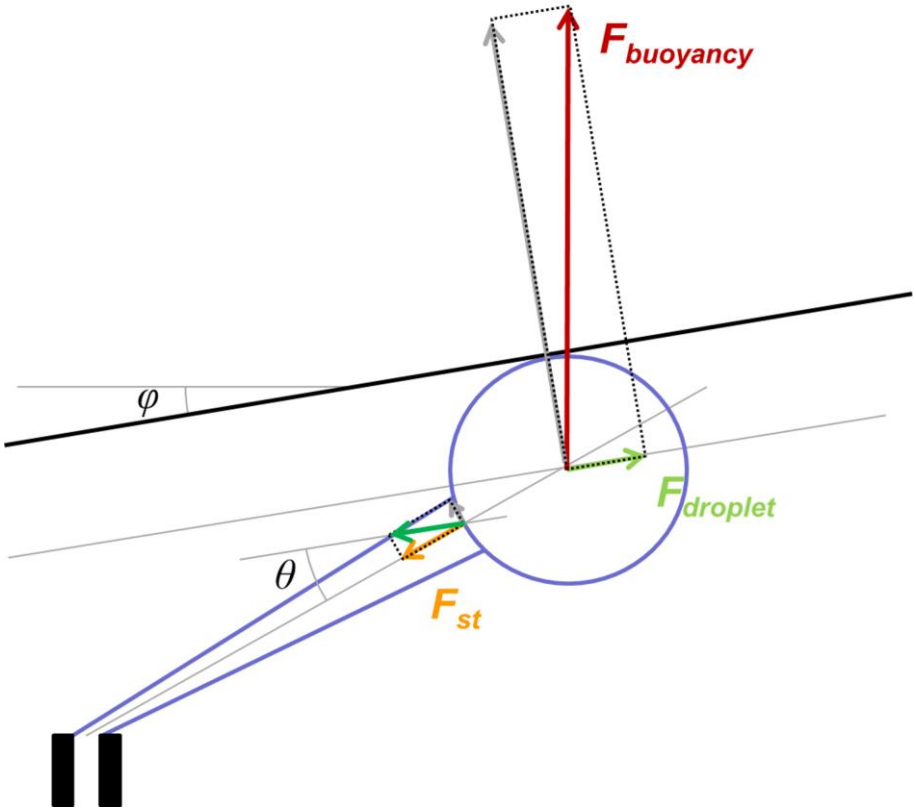

Figure 4. Schematic overview of the retraction force and the buoyancy force acting on the droplet and the liquid thread outside the capillary with a tilted ceiling (see also figure 7).

4. Shape of liquid threads

Interfacial tension may contribute twofold to shape (and stability) of fluids; 1) Interfacial tension defines a Laplace pressure related to local curvature of a liquid thread, 2) Interfacial tension creates an local axially oriented tensile retraction force that possibly also co-determines its shape.

The shape of an axial symmetric liquid thread can effectively be described by plotting the axial and radial curvature R_{ra} and R_{ax}. The curvature or bending also determines a Laplace pressure difference between the two sides of the surface (Laplace 1806, Young 1805). This means that shape of the liquid thread and pressure difference along the liquid thread are always interconnected.

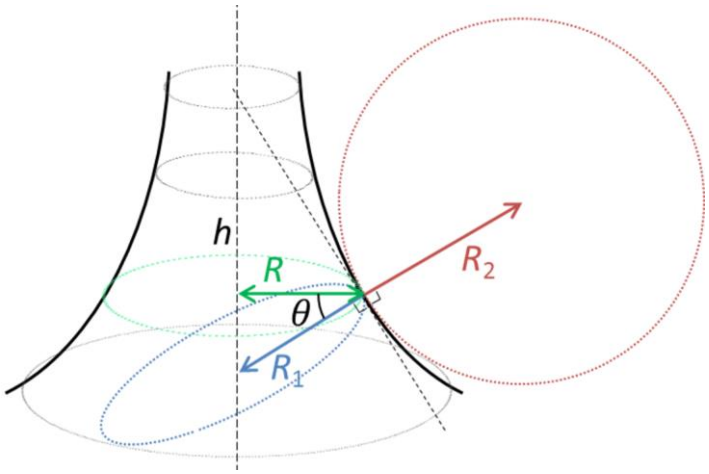

Figure 5. Schematic image showing the two local radii of curvatures for a tapering liquid thread.

The shape of the collapsed liquid thread having a neck near the exit of the capillary in the system of auto breakup is shown in figure 3E and 6.

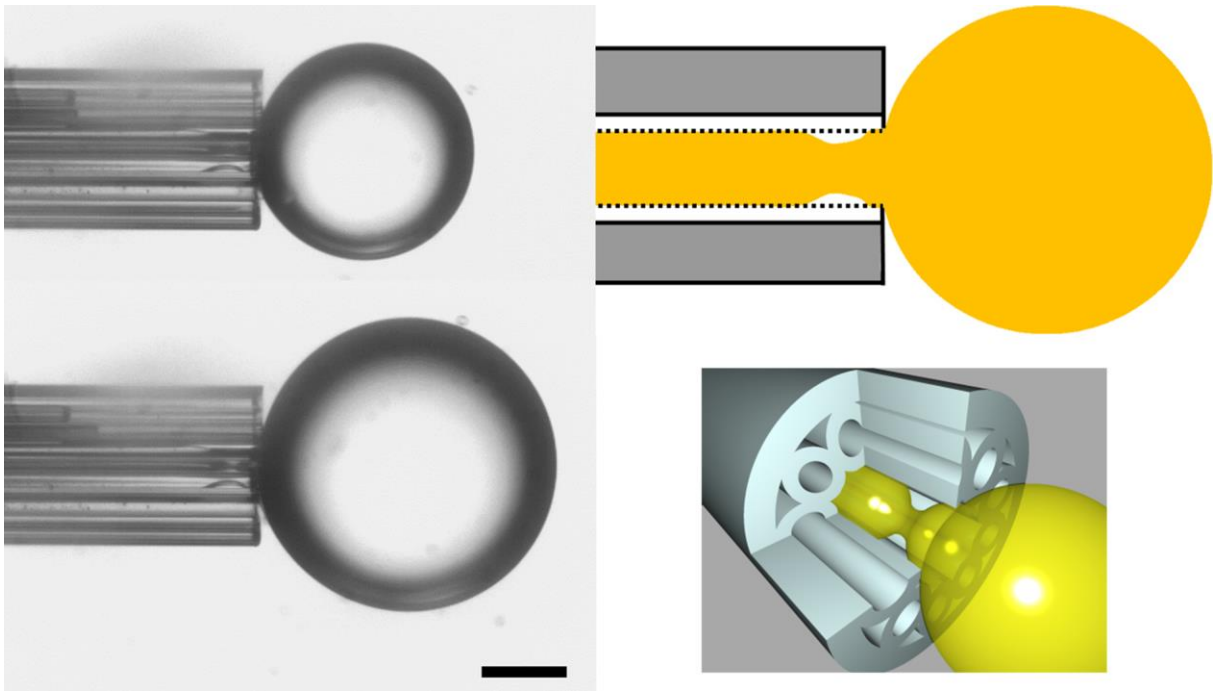

Figure 6. Two snapshots and two schematic images of a collapsed liquid thread with a stable liquid neck inside the capillary connected to a growing droplet. Scale bar is 200 µm.

A stable collapsed neck is formed inside the capillary around and above Ca_{cr}. The radius of this neck is smaller than the radius of the capillary. The shape of this short neck is strongly determined by a negative curvature $1/R_{ax}$ opposing the contribution of an increasing $1/R_{ra}$ to the Laplace pressure. This implies that a short collapsed neck can exist without a significant pressure drop over the neck. Practically this means that the total length of the short neck should be comparable with the diameter of the capillary or the liquid thread.

A tapering liquid thread in free surface flow has a much more elongated shape and here a pressure gradient is needed to keep it stable along the full length of the liquid thread (figure 7). The pressure is high at the narrow end of the liquid thread where the inner fluid is injected in the system and low near the droplet. The shape of the liquid thread in free surface flow is tapering towards the droplet, and seems related to the called widening jet (Utada et al. 2007).

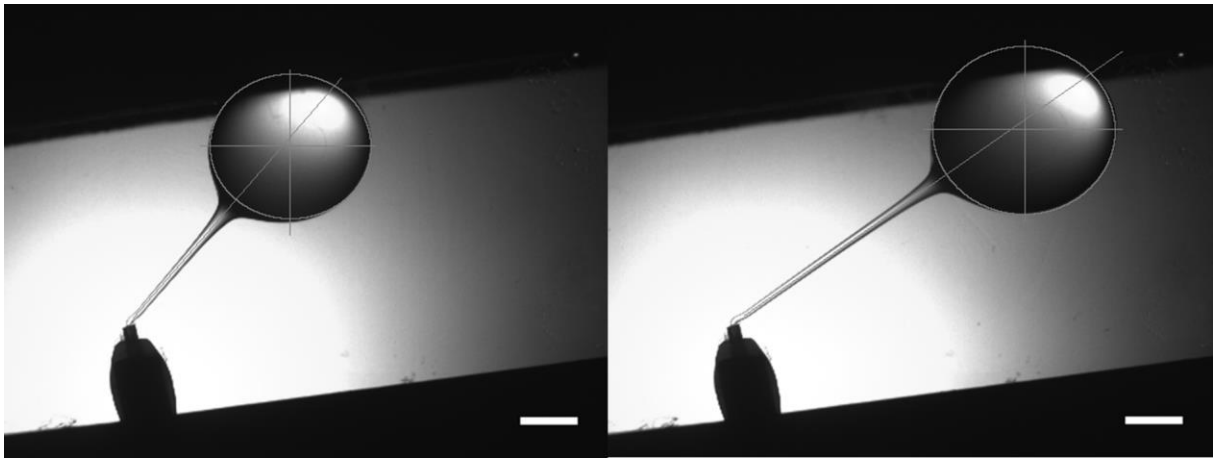

Figure 7. Snapshots of a liquid thread with timestamp before breakup. The droplet is slowly shifting upwards, due to the increasing buoyancy force on the liquid thread, stretching the liquid thread. Inner fluid is silicone oil (972 kg/m^3), and outer fluid is 1% tween20 (1002 kg/m^3). Scale bars are 2000 µm.

The shape of the liquid thread in free surface flow has been derived from an ordinary differential equation (ODE) based on simplified Navier-Stokes equations. A slender jet approximation has been applied and an analytical approximation for the shape of the

liquid thread was found $R \cong R_0 + \frac{QR_0}{12v_0\eta}z^2$, with R_0 and v_0 the radius and velocity at the nozzle respectively. The shape is dependent on the viscosity η and pressure gradient Q.

The shape of an emanating liquid jet was not found to be directly dependent on the viscosity. However an indirect effect of the viscosity is the decrease in inertial deceleration found for more viscous fluids. Viscous emanating jets have therefore a base with a broader appearance as can be seen in figure 7, especially for the high viscous jet.

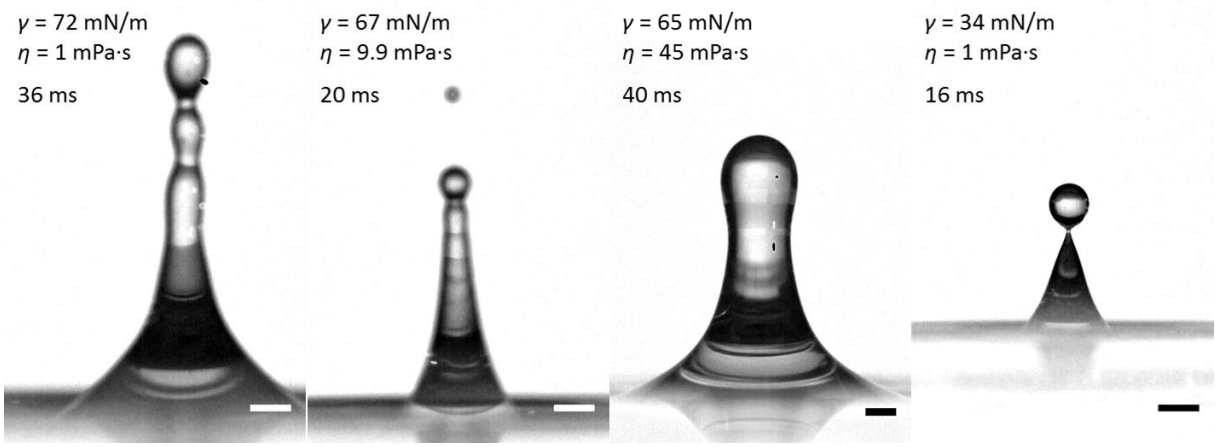

Figure 8. Emanating jets when reaching the highest point (apex) for different viscosities η and interfacial tensions γ. The zero point in time is set to the first moment that the jet becomes visible above the liquid surface. Scale bars are 2000 μm.

The shape of the liquid jet is defined by the local curvature from which the derived local Laplace pressure is in balance with a local pressure originating from the inertia of the liquid jet $p_{inertia} = \rho dh$, with d deceleration and h along the axisymmetric axe upwards. In contrast to the liquid thread from chapter 4, viscosity does not contribute to the shape of the emanating jet. Inner fluid velocities differences are too low to apply sufficient viscous shear forces to influence the shape of the liquid jet.

During the descend the shape of lower part of the liquid jet changes from a concave to a convex shape (see figure 8). The upper part of the liquid jet is still falling under gravity, whereas the lower part of the jet has already come down on the fluid bath resisting gravity. The lower part of the jet, which is continuously filled from the descending upper

part, resembles a large fluid reservoir physically supported by the bath below the liquid surface. The fluid reservoir of the lower part of the liquid jet is concave shaped and is energetically not favourable; surface tension forces will try to drive this concave reservoir into a convex one having a smaller surface area with increasing volume. Note that the total mass above the liquid surface increases (up to 40 ms, see figure 9) also after the liquid jet has reached its apex (at 25 ms). A more detailed approach for the fluid dynamics in the descend phase for the lower part of the liquid jet seems preferable in order to describe its shape.

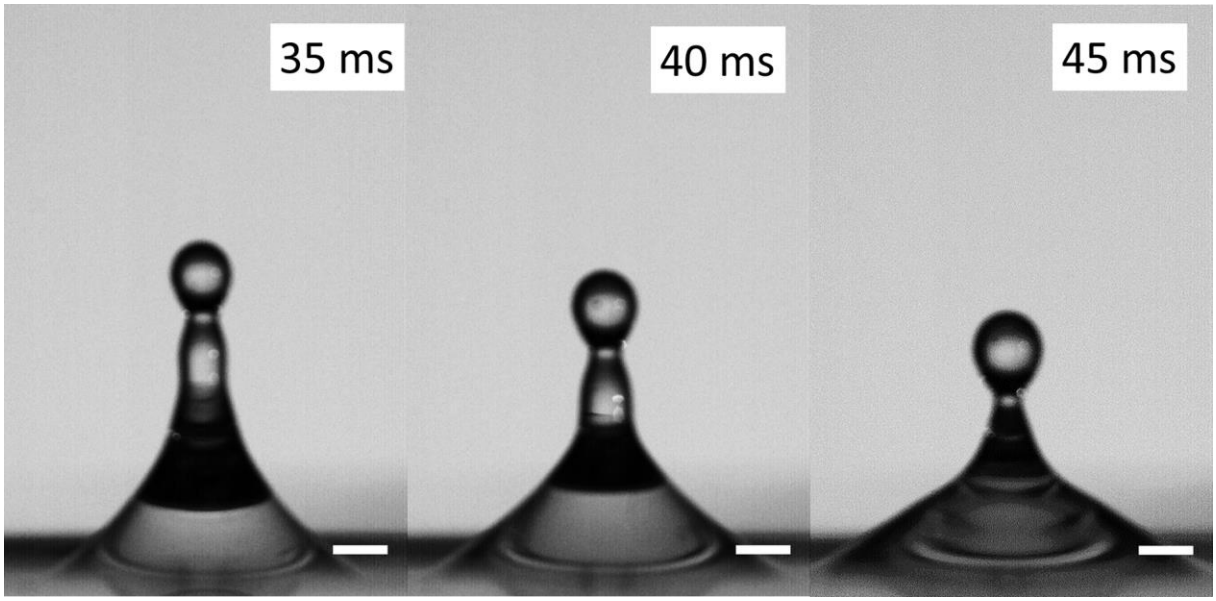

Figure 9. Snapshots of emanating liquid jet showing the transition from concave to convex shape of the lower part of the liquid jet. Scale bars are 2000 µm.

With respect to the liquid surface, an emanating liquid jet decelerates stronger than expected from gravity. The total deceleration a of the jet is the sum of the gravitational acceleration (g = 9.81 m/s^2) and the surface tension based inertial deceleration d of the jet. The deceleration d comes from the retraction force applied on the mass of the liquid jet. The gravitational deceleration g does not contribute to the shape of the liquid jet, because the liquid jet is essentially in free fall until mass flows back to the liquid bath (after 40 ms).

The model to describe emanating liquid jets presented in chapter 5 predicts to be valid in a broad range of dimensions and physical parameters. The existence of tiny water jets with a base radius of 10 μm having a deceleration of about 2 μm/μs^2 (is about $2 \cdot 10^5 \cdot g$) and a total mass of 1 ng. Large water jets can also be predicted with a base radius of 19 cm, having a deceleration of 0.0042 m/s^2 and a total inertial mass of about 13 kg. Such large jets can only be generated and observed in a gravitation free environment in view of the small inertial deceleration with respect to gravitational acceleration g.

5. Micro-threads during pinch-off

A micro-thread is a very thin fluidic thread, which from a surface energy standpoint seems unfavourable. Breakup is expected by reduction of the interfacial area. Micro-threads are therefore not stable and breakup occurs quickly via a universal pinch-off mechanism (Eggers 2005, Kowalewski 1996).

One of the findings of the emanating jets (chapter 5) may be linked to the liquid threads between a droplet and nozzle (chapter 4) by micro-threads (figures 6 and 7). A micro-thread is formed during breakup via a universal pinch-off mechanism (Eggers 2005). This pinch-off is asymmetric, because retraction of the liquid from the instable area is mainly contributed from liquid thread side and less from the droplet. A satellite droplet is formed when the micro-thread breaks up at both ends (Kowalewski 1996).

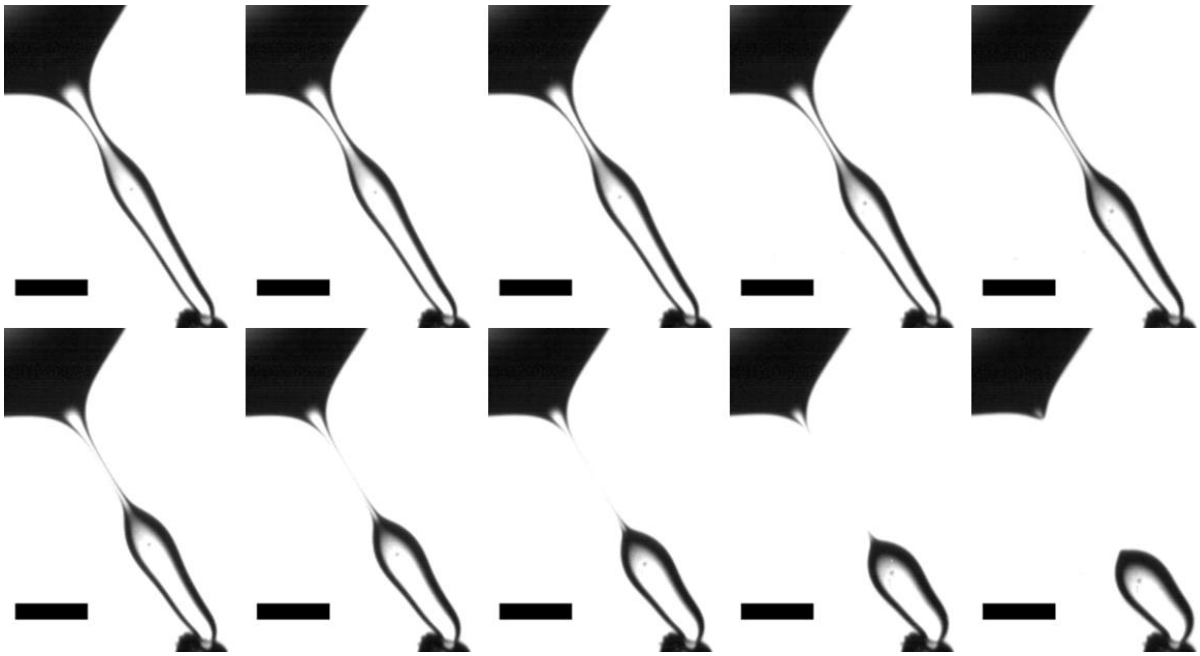

Figure 10. Pinch-off. Velocity v_0 is 23.6 mm/s. Time between each snapshot is 2 ms. Scale bars are 500 μm.

In figures 10 and 11 is shown that, after onset of the instability, a micro-thread is formed that quickly thins and elongates. The elongation is an effect from retraction of the side of the liquid thread towards a new forming droplet. A pressure gradient between the droplet and liquid neck could bring fluid in motion in the micro-thread and the inertia and/or viscous effects from the velocity of the inner fluid may counteract the squeezing surface tension force (Javadi et al. 2013).

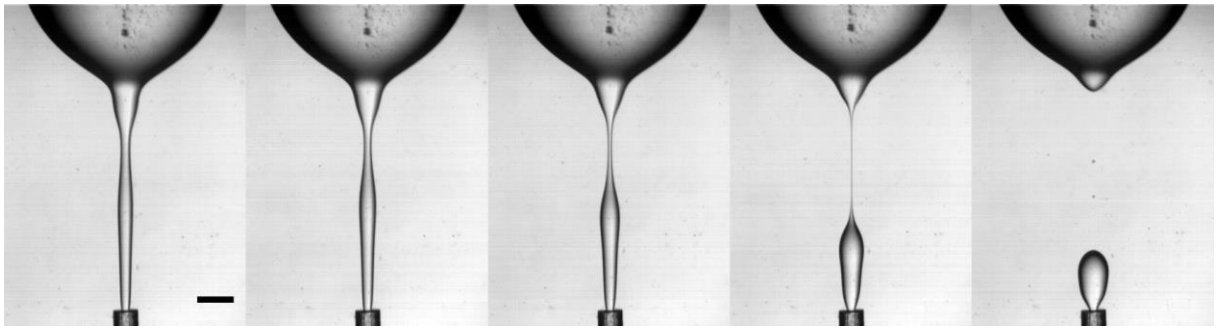

Figure 11. Pinch-off. Velocity v_0 is 63.7 mm/s. Time between each snapshot is 10 ms. Scale bar is 500 μm.

Often a droplet breaks up via pinch-off mechanism during the descend of an emanating liquid jet (figure 12) and a micro-thread is observed and is less elongated than observed from the liquid threads in free surface flow (figures 10 and 11), because of the short distance between bulk liquid and the droplet and the low pressure difference. The size of the droplet is predicted by a change in the pressure in the tip of the liquid jet (chapter 5).

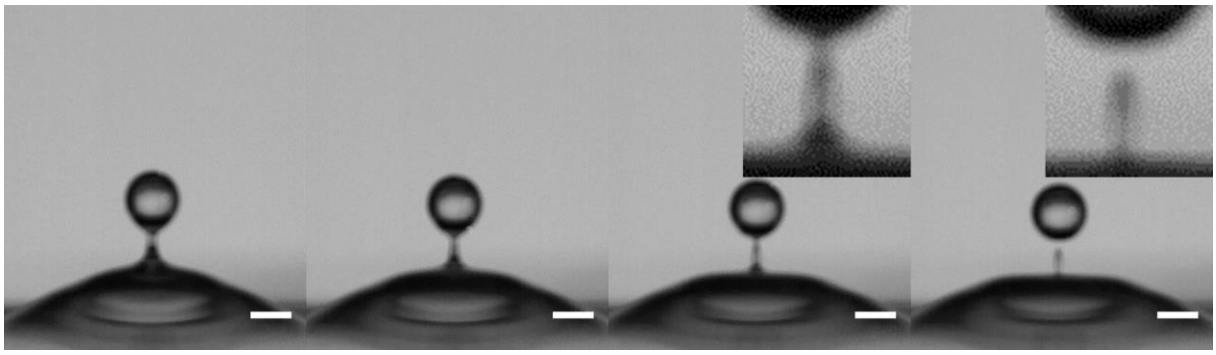

Figure 12. Pinch-off process of a droplet from an emanating liquid jet during its descend phase. The insets zoom in on the micro-thread just before and after breakup. Time between each snapshot is 0.5 ms. Scale bars are 2000 μm.

6. Vibrations in the liquid thread

Vibrations are often observed in liquid threads, especially close to the start of the breakup process. These vibrations occur close to the droplet and may be seen as perturbation steps towards further instability. The instability can be absolute or convective. Absolute instabilities start as perturbations which are amplified at the same position as where they start. Convective instabilities originate from perturbations that are amplified at a different position than started. The vibrations in the widening liquid thread close to the droplet have been observed as harmonic oscillations that end with a pinch-off mechanism (Sauter & Buggisch 2005, Utada et al. 2008, Zhou et al. 2006).

Vibrations in fluid interfaces have been observed in the three microfluidic systems: inside a capillary in the system of auto breakup (chapter 2 and 3), in long liquid threads close to the droplet in free surface flow (chapter 4), and in droplets on the tip of emanating liquid jets (chapter 5).

In auto breakup, vibrations are observed when actually breakup is hampered by viscous shear flow of the inner fluid. Actually, the instability is induced by change in pressure due to the growth of the droplet. Shear forces by the viscous flow of the fluid through the thread inhibits completion of the breakup process. The liquid thread remains stable with a certain shortest radius, but gets there via small vibrations around this radius. The narrow window in which these vibrations have been observed is just around the critical capillary number Ca_{cr} = 1/16 through the partly collapsed thread. This suggests that vibrations are only observed when the balance of pressures between viscous and surface tension forces is delicate.

In free surface flow, vibrations are observed in the liquid thread close to the droplet (see figure 13). The vibrations are observed as harmonic oscillations in a fixed point close to the droplet and end with breakup by pinch-off mechanism. It is unclear if the oscillations are following an absolute or convective instability, because it is unclear if the amplified instability moves along the liquid thread with the same velocity as the interface.

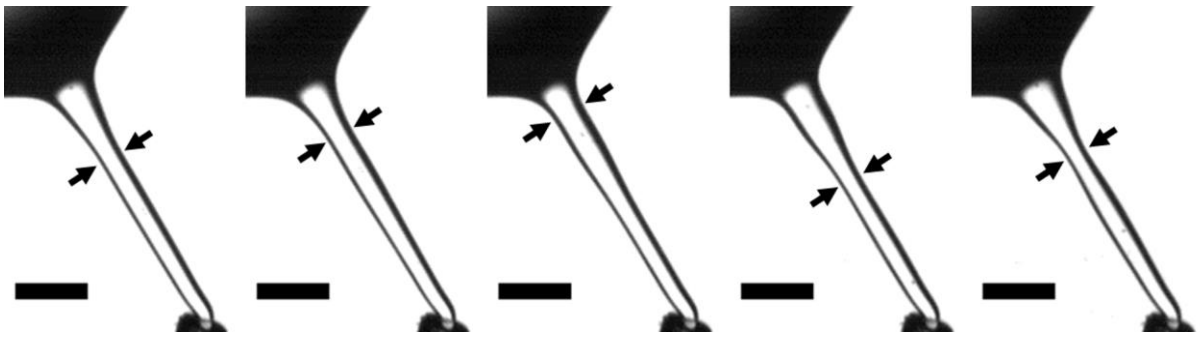

Figure 13. Snapshots depicting nearly one period of vibration in the neck. The thinnest part of the neck (marked arrows) oscillates at this rate. The time between two snapshots is 22 ms and one period is 170 ms. Velocity v_0 is 23.6 mm/s. scale bar is 500 μm.

The amount of visible vibrations in the liquid thread from a system with a ceiling (figure 13) is much more than in the system without a ceiling (figure 11). The ceiling is tilted and reduces the effect of buoyancy force of the droplet on the liquid jet, which probably slows down the whole process from a stable liquid thread to a liquid thread with a specific length that becomes instable.

Vibrations are difficult to observe in an emanating liquid jet, but small vibrations have been observed in the total height of the jet (including the droplet attached to the liquid jet) during its rise (chapter 5), indicating pressure changes in the tip of the jet (figure 14). The height of the liquid was fitted to experimental data H_{fit}, and the difference with experimental H shows an oscillation of two periods. The period of the vibrations in the droplet is about 2.1 ms, and the amplitude is constant at 70 μm for a number of periods.

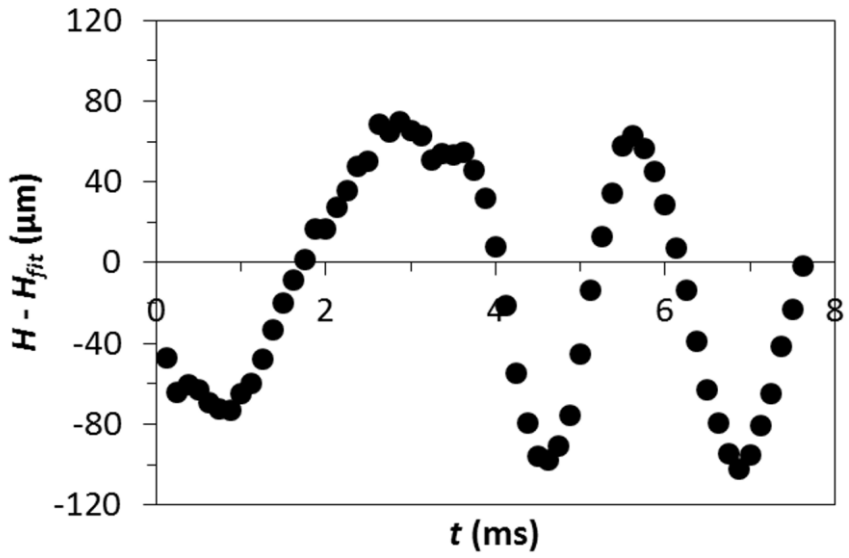

Figure 14. Vibrations of the tip height of a 60% glycerol jet.

7. Lessons learned

In the system of auto breakup a critical capillary number $Ca_{cr} = \frac{\eta v_{cr}}{\gamma} = 1/16$ was found that determines the regime of auto breakup. Also we determined that the breakup region where breakup happens inside the capillary is about twice the radius of the capillary. The critical capillary number is based only on the ratio between viscosity and interfacial tension of the inner fluid and determines by a maximum critical velocity the regime of auto breakup. From this we learn that the mechanism of auto breakup is applicable for a wide range of fluids, and can possibly also work for gas-in-liquid and liquid-in-gas systems. However there are some limitations: Wetting of the capillary inner wall should be considered. Wetting of the capillary inner wall by the inner fluid

hampers auto breakup and leads to non-uniform droplets. Also the viscosity of the outer fluid should be sufficiently low in order not to hamper the passive inflow of the outer fluid in the corrugations of the capillary.

One of the main learnings from the system with a stable free surface liquid thread is that an applied pressure gradient $Q = \frac{Q_0}{L} - Q_1$ determines the stability of the liquid thread. Here, Q_0 is the pressure difference over the liquid thread with length L and Q_1 was added to correct for energy transfer and dissipation to the outer fluid. During the elongation of the liquid thread Q decreases towards 0, and a prediction was obtained for the maximum length of the liquid thread $L_{max} = \frac{Q_0}{Q_1}$.

8. Potential applications with auto breakup

The system of auto breakup is robust because droplet sizes remain relatively uniform upon changes in flow rate up to the critical flow rate, which for the first time can be calculated using the relation for the critical capillary number Ca_{cr}. Because auto breakup only uses a passive flow of the outer fluid to enable breakup, in contrast to flow focusing techniques, upscaling of the auto break-up nozzles can be easily done with micro-machined membranes (figure 15).

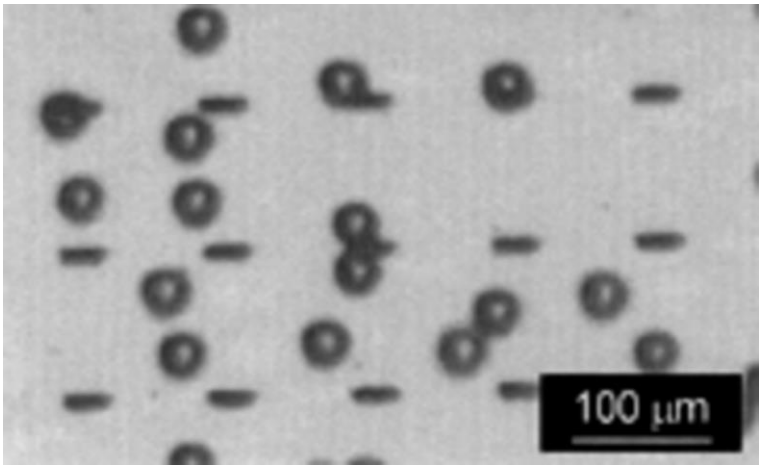

Figure 15. Snapshot of droplet formation from a membrane with rectangular pores (Kobayashi et al. 2002).

A disadvantage of the auto breakup mechanism is that the process is relatively slow, because above the critical capillary number Ca_{cr} breakup is blocked and droplets grow towards infinite. The maximum flow rate $\Phi = \pi(R_c)^2 v_{cr}$, with R_c defined as an effective radius of one (micro-corrugated) pore and the maximum velocity can be derived from $Ca_{cr} = \frac{\eta v_{cr}}{\gamma} = \frac{1}{16}$. For sunflower oil as inner fluid (68 mPa·s), 1% tween20 as outer fluid (4.5 mN/m), and R_c = 50 μm, a maximum flow rate Φ per pore is 0.12 mL/h. Scaling up by parallelisation of the pores in a membrane with an effective open porosity of 5% would increase the maximum flow rate with a 1 m^2 membrane surface to nearly 750 L/h/m^2. Lowering the viscosity to 1 mPa·s would increase the maximum flow rate to 50 m^3/h/m^2. Higher droplet formation rates in auto breakup can thus be obtained by lowering the viscosity of the inner fluid. The viscosity can be lowered by using an inner fluid with a lower viscosity and/or an increase of the operating temperature of the system. An example of auto breakup with an inner fluid with low viscosity is divinyl benzene is (η = 1 mPa·s at 20 °C) and as a low viscosity outer fluid water. A stream of droplets that move upwards is depicted in figure 16A.

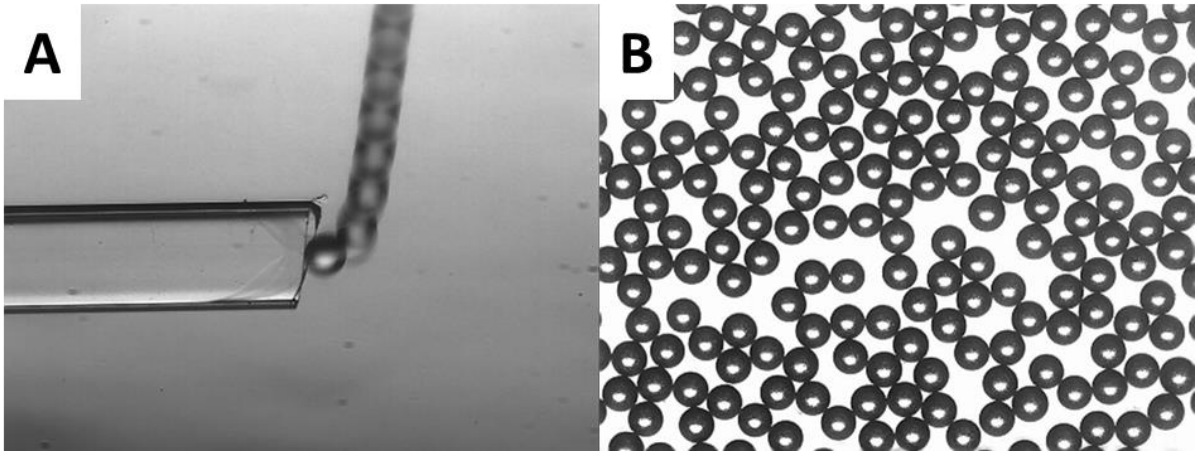

Figure 16. Snapshot of droplets formation of divinyl benzene in water. **A** Side view on the flat side of a rectangular capillary (inner dimensions of 20x200 μm) at droplet formation by auto breakup. The droplets move upwards because divinyl benzene is less dense than water ($\Delta\rho$ = 70 kg/m^3). Snapshot is taken with long shutter. **B** Top view on divinyl benzene droplets showing the uniformity of the droplet sizes (40 μm).

The mechanism of auto breakup could also be a useful tool at laboratory scale for particle formation from droplets by emulsion polymerisation (Shah et al. 2008). One way of making these particles from droplets is via ultra violet (UV) induced radical polymerisation of the monomers in the droplets. Uniform droplets of monomers, containing acrylate- or vinyl groups, and UV-initiator (hydroxy dimethyl acetophenone) have been made at our laboratory via auto breakup. After preparing a batch of droplets, or during droplet formation, an UV-lamp is switched on and droplets are polymerised to solid particles as shown in figure 17.

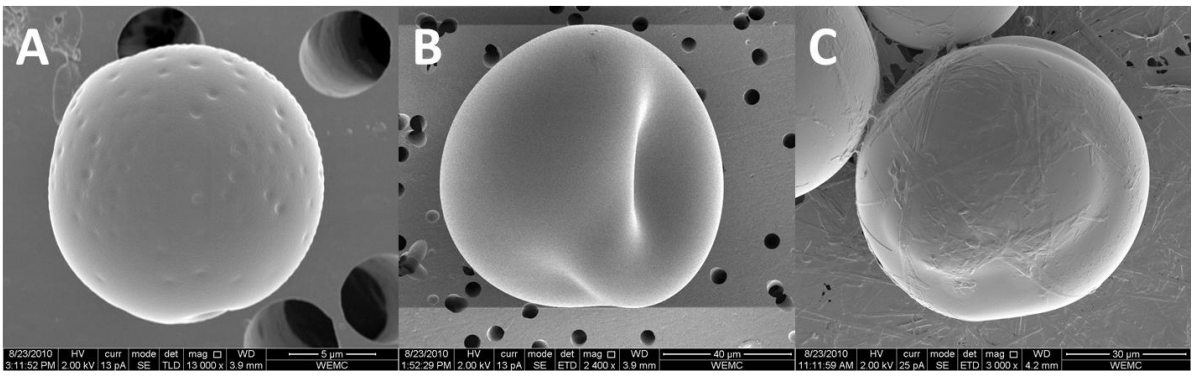

Figure 17. Scanning electron microscopy (SEM) images of particles of **A** poly(butylacrylate), **B** poly(1,6-hexanediol dimethacrylate), and **C** poly(butylacrylate)-copoly(1,6-hexanediol dimethacrylate) 1:1 mol ratio.

The principle of auto breakup could also be used as a platform to make special types of particles, for example Janus particles. A Janus particle is a solid anisotropic particle that has two sides with different properties, for example: charge, chemical loading, colour, density, or surface morphology. Additional techniques are required to have the two required compounds separated in the fluid droplet before the droplet is made solid into a Janus particle. These particles have been made by using a microfluidic device where two streams of different inner fluids were brought together forming one droplet in the co-flow of the outer fluid (Nisisako et al. 2006).

References

Ali M, Umemura A. 2009. Relaxation and breakup of a cylindrical liquid column. *J. Mech. Eng. Vol 39, No 2*

Alimov MM, Kornev KG. 2014. Meniscus on a shaped fibre: Singularities and hodograph formulation. *Proc R Soc A Math Phys Eng Sci*. 470(2168):

Ambravaneswaran B, Phillips SD, Basaran OA. 2000. Theoretical Analysis of a Dripping Faucet. *Phys. Rev. Lett.* 85(25):5332–35

Anna SL, Bontoux N, Stone HA. 2003. Formation of dispersions using "flow focusing" in microchannels. *Appl. Phys. Lett.* 82(3):364–66

Basaran OA. 2002. Small-scale free surface flows with breakup: Drop formation and emerging applications. *AIChE J.* 48(9):1842–48

Booty MR, Papageorgiou DT, Siegel M, Wang Q. 2013. Long-wave equations and direct simulations for the breakup of a viscous fluid thread surrounded by an immiscible viscous fluid. *IMA J. Appl. Math. (Institute Math. Its Appl.* 78(4):851–67

Brenner MP, Lister JR, Stone HA. 1996. Pinching threads, singularities and the number 0.0304... *Phys. Fluids*. 8(11):

Cai YK. 1989. Phenomena of a liquid drop falling to a liquid surface. *Exp. Fluids*. 7(6):388–94

Castro-Hernández E, Gundabala V, Fernández-Nieves A, Gordillo JM. 2009. Scaling the drop size in coflow experiments. *New J. Phys.* 11:

Christopher GF, Anna SL. 2007. Microfluidic methods for generating continuous droplet streams. *J. Phys. D. Appl. Phys.* 40(19):R319–36

Clanet C, Lasheras JC. 1999. Transition from dripping to jetting. *J. Fluid Mech.* 383:307–26

Clarke NS. 1966. A differential equation in fluid mechanics. *Mathematika*. 13(01):51–53

Cohen I, Brenner MP, Eggers J, Nagel SR. 1999. Two fluid drop snap-off problem: Experiments and theory. *Phys. Rev. Lett.* 83(6):1147–50

Colin T, Tancogne S. 2011. Stability of bifluid jets in microchannels. *Eur. J. Mech. B/Fluids*. 30(4):409–20

Cramer C, Fischer P, Windhab EJ. 2004. Drop formation in a co-flowing ambient fluid. *Chem. Eng. Sci.* 59(15):3045–58

Dorsey NE. 1940. *Properties of Ordinary Water-Substance in All Its Phases: Water Vapor, Water, and All the Ices;* New York: Reinhold Publishing Corporation

Doshi P, Cohen I, Zhang WW, Siegel M, Howell P, et al. 2003. Persistence of Memory in Drop Breakup: The Breakdown of Universality. *Science (80-.).* 302(5648):1185–88

Eastoe J, Dalton JS. 2000. Dynamic surface tension and adsorption mechanisms of surfactants at the air–water interface. *Adv Colloid Interface Sci*. 85(2–3):103–44

Eggers J. 1993. Universal pinching of 3D axisymmetric free-surface flow. *Phys. Rev. Lett.* 71(21):3458–60

Eggers J. 1997. Nonlinear dynamics and breakup of free-surface flows. *Rev. Mod. Phys.* 69(3):865–930

Eggers J. 2005. Drop formation - An overview. *Zeitschrift fur Angew. Math. und Mech.* 85(6):400–410

Eggers J. 2012. Stability of a viscous pinching thread. *Phys. Fluids*. 24(7):

Eggers J, Dupont TF. 1994. Drop formation in a one-dimensional approximation of the Navier-Stokes equation. *J. Fluid Mech.* 262:205–21

Eggers J, Villermaux E. 2008. Physics of liquid jets. *Reports Prog. Phys.* 71(3):

Fu T, Wu Y, Ma Y, Li HZ. 2012. Droplet formation and breakup dynamics in microfluidic flow-focusing devices: From dripping to jetting. *Chem. Eng. Sci.* 84(0):207–17

Gallant RW. 1967. Physical properties of hydrocarbons. Part 14. Propylene glycols and glycerine. *Hydrocarb Process*. 46(5):201–15

Gañán-Calvo AM. 1998. Generation of steady liquid microthreads and micron-sized monodisperse sprays in gas streams. *Phys. Rev. Lett.* 80(2):285–88

Gañán-Calvo AM, Gordillo JM. 2001. Perfectly monodisperse microbubbling by capillary flow focusing

Garstecki P, Stone HA, Whitesides GM. 2005. Mechanism for flow-rate controlled breakup in confined geometries: A route to monodisperse emulsions. *Phys. Rev. Lett.* 94(16):

Gekle S, Gordillo JM. 2010. Generation and breakup of Worthington jets after cavity collapse. Part 1. Jet formation. *J. Fluid Mech.* 663:293–330

Gekle S, Gordillo JM, van der Meer D, Lohse D. 2009. High-Speed Jet Formation after Solid Object Impact. *Phys. Rev. Lett.* 102(3):34502

Gijsbertsen-Abrahamse AJ, van der Padt A, Boom RM. 2004. Status of cross-flow membrane emulsification and outlook for industrial application. *J. Memb. Sci.* 230(1–2):149–59

Gordillo JM, Gekle S. 2010. Generation and breakup of Worthington jets after cavity collapse. Part 2. Tip breakup of stretched jets. *J. Fluid Mech.* 663:331–46

Guillot P, Colin A, Ajdari A. 2008. Stability of a jet in confined pressure-driven biphasic flows at low Reynolds number in various geometries. *Phys. Rev. E - Stat. Nonlinear, Soft Matter Phys.* 78(1):

Hancock MJ, Bush JWM. 2002. Fluid pipes. *J. Fluid Mech.* 466:285–304

Henderson DM, Pritchard WG, Smolka LB. 1997. On the pinch-off of a pendant drop of viscous fluid. *Phys. Fluids*. 9(11):

Hogrefe JE, Peffley NL, Goodridge CL, Shi WT, Hentschel HGE, Lathrop DP. 1998. Power-law singularities in gravity-capillary waves. *Phys. D Nonlinear Phenom.* 123(1-4):183–205

Hoppe J, Melin T. 2007. A new technology for producing mono-disperse macroemulsions. *J. Memb. Sci.* 303(1-2):100–111

Huang Q, Zhang H. 2008. A study of different fluid droplets impacting on a liquid film. *Pet. Sci.* 5(1):62–66

Huerre P, Monkewitz PA. 1990. Local and Global Instabilities in Spatially Developing Flows. *Annu. Rev. Fluid Mech.* 22(1):473–537

Humphry KJ, Ajdari A, Fernández-Nieves A, Stone HA, Weitz DA. 2009. Suppression of instabilities in multiphase flow by geometric confinement. *Phys. Rev. E - Stat. Nonlinear, Soft Matter Phys.* 79(5):

James DF. 1974. The meniscus on the outside of a small circular cylinder. *J Fluid Mech*. 63(04):657–64

Javadi A, Eggers J, Bonn D, Habibi M, Ribe NM. 2013. Delayed Capillary Breakup of Falling Viscous Jets. *Phys. Rev. Lett.* 110(14):144501

Kawakatsu T, Kikuchi Y, Nakajima M. 1997. Regular-sized cell creation in microchannel emulsification by visual microprocessing method. *J. Am. Oil Chem. Soc.* 74(3):317–21

Kobayashi I, Hirose S, Katoh T, Zhang Y, Uemura K, Nakajima M. 2008. High-aspect-ratio through-hole array microfabricated in a PMMA plate for monodisperse emulsion production. *Microsyst. Technol.* 14(9-11):1349–57

Kobayashi I, Lou X, Mukataka S, Nakajima M. 2005a. Preparation of monodisperse water-in-oil-in-water emulsions using microfluidization and straight-through microchannel emulsification. *JAOCS, J. Am. Oil Chem. Soc.* 82(1):65–71

Kobayashi I, Mukataka S, Nakajima M. 2004. Effect of slot aspect ratio on droplet formation from silicon straight-through microchannels. *J. Colloid Interface Sci.* 279(1):277–80

Kobayashi I, Mukataka S, Nakajima M. 2005b. Effects of type and physical properties of oil phase on oil-in-water emulsion droplet formation in straight-through microchannel emulsification, experimental and CFD studies. *Langmuir*. 21(13):5722–30

Kobayashi I, Nakajima M, Chun K, Kikuchi Y, Fujita H. 2002. Silicon array of elongated through-holes for monodisperse emulsion droplets. *AIChE J.* 48(8):1639–44

Kobayashi I, Neves MA, Yokota T, Uemura K, Nakajima M. 2009. Generation of geometrically confined droplets using microchannel arrays: Effects of channel and step structure. *Ind. Eng. Chem. Res.* 48(19):8848–55

Kobayashi I, Uemura K, Nakajima M. 2006a. Controlled generation of monodisperse discoid droplets using microchannel arrays. *Langmuir*. 22(26):10893–97

Kobayashi I, Uemura K, Nakajima M. 2006b. CFD study of the effect of a fluid flow in a channel on generation of oil-in-water emulsion droplets in straight-through microchannel emulsification. *J. Chem. Eng. Japan*. 39(8):855–63

Kobayashi I, Wada Y, Uemura K, Nakajima M. 2010. Microchannel emulsification for mass production of uniform fine droplets: Integration of microchannel arrays on a chip. *Microfluid. Nanofluidics*. 8(2):255–62

Kowalewski TA. 1996. On the separation of droplets from a liquid jet. *Fluid Dyn. Res.* 17(3):121–45

Laplace P-S de. 1806. *Supplément au dixième livre du Traité de mécanique céleste sur l'action capillaire.* Paris: Duprat

Lauga E, Stone HA. 2003. Effective slip in pressure-driven Stokes flow. *J. Fluid Mech.*, pp. 55–77

Li Z, Mak SY, Sauret A, Shum HC. 2014. Syringe-pump-induced fluctuation in all-aqueous microfluidic system implications for flow rate accuracy. *Lab Chip*. 14(4):744–49

Li J, Rossignol F, Macdonald J. 2015. Inkjet printing for biosensor fabrication: combining chemistry and technology for advanced manufacturing. *Lab Chip*. 15(12):2538–58

Lin SP, Reitz RD. 1998. Drop and spray formation from a liquid jet. *Annu. Rev. Fluid Mech.* 30(1):85–105

Longuet-Higgins MS. 2001. Vertical jets from standing waves. *Proc R Soc A Math Phys Eng Sci*. 457(2006):495–510

Manzello SL, Yang JC. 2002. An experimental study of a water droplet impinging on a liquid surface. *Exp. Fluids*. 32(5):580–89

Marston JO, Thoroddsen ST. 2008. Apex jets from impacting drops. *J. Fluid Mech.* 614:293–302

McKinley GH. 2005. Visco-Elasto-Capillary Thinning and Break-Up of Complex Fluids

Meyer RF, Crocker JC. 2009. Universal dripping and jetting in a transverse shear flow. *Phys. Rev. Lett.* 102(19):

Nakashima T, Shimizu M, Kukizaki M. 1991. Membrane emulsification by microporous glass. *Key Eng. Mater.* 61-62:513–16

Nie Z, Seo M, Xu S, Lewis PC, Mok M, et al. 2008. Emulsification in a microfluidic flow-focusing device: Effect of the viscosities of the liquids. *Microfluid. Nanofluidics*. 5(5):585–94

Nieuwland PJ, Segers R, Koch K, van Hest JCM, Rutjes FPJT. 2011. Fast Scale-Up Using Microreactors: Pyrrole Synthesis from Micro to Production Scale. *Org. Process Res. Dev.* 15(4):783–87

Nisisako T, Torii T. 2008. Microfluidic large-scale integration on a chip for mass production of monodisperse droplets and particles. *Lab a Chip - Miniaturisation Chem. Biol.* 8(2):287–93

Nisisako T, Torii T, Higuchi T. 2002. Droplet formation in a microchannel network. *Lab a Chip - Miniaturisation Chem. Biol.* 2(1):24–26

Papageorgiou DT. 1995. On the breakup of viscous liquid threads. *Phys. Fluids*. 7(7):1529–44

Peng SJ, Williams RA. 1998. Controlled production of emulsions using a crossflow membrane. Part I: Droplet formation from a single pore. *Chem. Eng. Res. Des.* 76(A8):894–901

Peters IR, Tagawa Y, Oudalov N, Sun C, Prosperetti A, et al. 2013. Highly focused supersonic microjets: Numerical simulations. *J Fluid Mech*. 719:587–605

Ray B, Biswas G, Sharma A. 2010. Generation of secondary droplets in coalescence of a drop at a liquid-liquid interface. *J. Fluid Mech.* 655:72–104

Rayleigh, Lord. 1878. On the instability of jets. *Proc. London Math. Soc.* 10(4):4–13

Rayleigh, Lord. 1892. XVI. On the instability of a cylinder of viscous liquid under capillary force. *Philos. Mag. Ser. 5*. 34(207):145–54

Rein M. 1993. Phenomena of liquid drop impact on solid and liquid surfaces. *Fluid Dyn. Res.* 12(2):61–93

Rein M. 1996. The transitional regime between coalescing and splashing drops. *J. Fluid Mech.* 306:145–65

Rodriguez F, Mesler R. 1985. Some drops don't splash. *J. Colloid Interface Sci.* 106(2):347–52

Sauret A, Spandagos C, Shum HC. 2012. Fluctuation-induced dynamics of multiphase liquid jets with ultra-low interfacial tension. *Lab a Chip - Miniaturisation Chem. Biol.* 12(18):3380–86

Sauter US, Buggisch HW. 2005. Stability of initially slow viscous jets driven by gravity. *J. Fluid Mech.* 533:237–57

Seemann R, Brinkmann M, Pfohl T, Herminghaus S. 2012. Droplet based microfluidics. *Reports Prog. Phys.* 75(1):

Shah R, Shum HC, Rowat A, Lee D, Agresti J, et al. 2008. Designer emulsions using microfluidics. *Mater. Today*. 11(4):18–27

Shaw R. 1984. The dripping faucet as a model chaotic system

Shen Y, Van Beek TA, Zuilhof H, Chen B. 2013. Hyphenation of optimized microfluidic sample preparation with nano liquid chromatography for faster and greener alkaloid analysis. *Anal. Chim. Acta*. 797:50–56

Shi XD, Brenner MP, Nagel SR. 1994. A cascade of structure in a drop falling from a faucet. *Science (80-.).* 265(5169):219–22

Shui L, Mugele F, Van Den Berg A, Eijkel JCT. 2008. Geometry-controlled droplet generation in head-on microfluidic devices. *Appl. Phys. Lett.* 93(15):

Spyropoulos F, Lloyd DM, Hancocks RD, Pawlik AK. 2014. Advances in membrane emulsification. Part A: Recent developments in processing aspects and microstructural design approaches. *J. Sci. Food Agric.* 94(4):613–27

Steegmans MLJ, De Ruiter J, Schroën KGPH, Boom RM. 2010. A descriptive force-balance model for droplet formation at microfluidic Y-junctions. *AIChE J.* 56(10):2641–49

Steegmans MLJ, Schroën CGPH, Boom RM. 2009. Generalised insights in droplet formation at T-junctions through statistical analysis. *Chem. Eng. Sci.* 64(13):3042–50

Stone HA, Leal LG. 1989. Relaxation and breakup of an initially extended drop in an otherwise quiescent fluid. *J. Fluid Mech.* 198:399

Sugiura S, Nakajima M, Iwamoto S, Seki M. 2001. Interfacial tension driven monodispersed droplet formation from microfabricated channel array. *Langmuir*. 17(18):5562–66

Sugiura S, Nakajima M, Seki M. 2002. Effect of channel structure on microchannel emulsification. *Langmuir*. 18(15):5708–12

Subramani HJ, Yeoh HK, Suryo R, Xu Q, Ambravaneswaran B, Basaran OA. 2006. Simplicity and complexity in a dripping faucet. *Phys. Fluids*. 18(3):

Suryo R, Basaran OA. 2006. Tip streaming from a liquid drop forming from a tube in a co-flowing outer fluid. *Phys. Fluids*. 18(8):

Sutera SP, Skalak R. 1993. The History of Poiseuille's Law. *Annu. Rev. Fluid Mech.* 25(1):1–20

Tanner RI. 2005. A theory of die-swell revisited. *J. Nonnewton. Fluid Mech.* 129(2):85–87

Thorsen T, Roberts RW, Arnold FH, Quake SR. 2001. Dynamic pattern formation in a vesicle-generating microfluidic device. *Phys. Rev. Lett.* 86(18):4163–66

Ushikubo FY, Birribilli FS, Oliveira DRB, Cunha RL. 2014. Y- and T-junction microfluidic devices: effect of fluids and interface properties and operating conditions. *Microfluid. Nanofluidics*. 17(4):711–20

Utada AS, Fernández-Nieves A, Gordillo JM, Weitz DA. 2008. Absolute instability of a liquid jet in a coflowing stream. *Phys. Rev. Lett.* 100(1):014502

Utada AS, Fernández-Nieves A, Stone HA, Weitz DA. 2007. Dripping to jetting transitions in coflowing liquid streams. *Phys. Rev. Lett.* 99(9):094502

Van der Zwan EA, Schroën K, Boom RM. 2009. A geometric model for the dynamics of microchannel emulsification. *Langmuir*. 25(13):7320–27

Van Dijke KC, de Ruiter R, Schroën K, Boom RM. 2010a. The mechanism of droplet formation in microfluidic EDGE systems. *Soft Matter*. 6(2):321–30

Van Dijke KC, Schroën KCPGH, Boom RM. 2008. Microchannel emulsification: From computational fluid dynamics to predictive analytical model. *Langmuir*. 24(18):10107–15

Van Dijke KC, Veldhuis G, Schroën K, Boom RM. 2010b. Simultaneous formation of many droplets in a single microfluidic droplet formation unit. *AIChE J.* 56(3):833–36

Van Rijn CJM. 2004. *Nano and Micro Engineered Membrane Technology*. Elsevier Amsterdam. ISBN: 0.444-51489-9

Wang W, Ngan KH, Gong J, Angeli P. 2009. Observations on single drop formation from a capillary tube at low flow rates. *Colloids Surfaces A Physicochem. Eng. Asp.* 334(1-3):197–202

Whitesides GM. 2006. The origins and the future of microfluidics. *Nature*. 442(7101):368–73

Wilkes ED, Phillips SD, Basaran OA. 1999. Computational and experimental analysis of dynamics of drop formation. *Phys. Fluids*. 11(12):3577–98

Wikipedia Contributors. 2015. *Curvature*. Wikipedia, The Free Encyclopedia,. https://en.wikipedia.org/w/index.php?title=Curvature&oldid=663144210

Worthington AM. 1882. On Impact with a Liquid Surface. *Proc R Soc London* . 34 (220-223):217–30

Worthington AM, Cole RS. 1900. Impact with a Liquid Surface Studied by the Aid of Instantaneous Photography. Paper II. *Philos Trans R Soc London Ser A, Contain Pap a Math or Phys Character* . 194 (252-261):175–99

Yarin AL. 2006. Drop impact dynamics: Splashing, spreading, receding, bouncing... *Annu. Rev. Fluid Mech.* 38:159–92

Young T. 1805. An Essay on the Cohesion of Fluids. *Philos. Trans. R. Soc. London*. 95:65–87

Yuan Q, Williams RA. 2014. Precision emulsification for droplet and capsule production. *Adv. Powder Technol.* 25(1):122–35

Zeff BW, Kleber B, Fineberg J, Lathrop DP. 2000. Singularity dynamics in curvature collapse and jet eruption on a fluid surface. *Nature*. 403(6768):401–4

Zhao H, Brunsvold A, Munkejord ST. 2011. Investigation of droplets impinging on a deep pool: Transition from coalescence to jetting. *Exp. Fluids*. 50(3):621–35

Zhao Y, Chen G, Yuan Q. 2006. Liquid-liquid two-phase flow patterns in a rectangular MicroChannel. *AIChE J.* 52(12):4052–60

Zhou C, Yue P, Feng JJ. 2006. Formation of simple and compound drops in microfluidic devices. *Phys. Fluids*. 18(9):

List of Symbols

Latin symbols

symbol	*Description*	*Unit/value*
A	Surface area	m^2
Ca_{cr}	Critical Capillary number	1/16
Ca	Capillary number	-
D	Diameter liquid thread, droplet or jet	m
d	Deceleration of liquid jet	m/s^2
g	Acceleration due to gravity	9.81 m/s^2
H	Distance between point of breakup and end of capillary; or height of the tip of the liquid jet above the surface	m
h	Distance along the axis of the liquid jet	m
k	Ratio periodicity of longitudinal corrugations and free surface	-
L	Length of the liquid thread	m
p	Pressure	Pa (or N/m^2)
Δp	Pressure difference	Pa (or N/m^2)
Q	Pressure gradient	N/m^3
R	Radius liquid thread or jet	m
Re	Reynold's number	-
We	Weber number	-

Greek symbols

symbol	*Description*	*Unit*
η	Viscosity	Pa.s
γ	Interfacial tension	N/m
$\dot{\gamma}$	Shear rate	s^{-1}
δ	Fraction of slip area with respect to total area	m
η	Viscosity	Pa·s
θ	Angle between liquid neck and ceiling	° or rad
λ	Slip length	m
ρ	Density	kg/m^3
Φ	Flow rate of the inner fluid	m^3/s

Appendix A

Processing images from the movies

Images were processed by ImageJ software to retrieve the coordinates of the outline of the droplet and liquid neck. The resolution of the image provides pixel size and frame rate (fps) the time dependence between frames. The coordinates of the interface were processed by scripts in Matlab software to obtain the flow rate and droplet radius.

Process a movie by ImageJ

In ImageJ, the steps explained below have been applied to the snapshots of the movies. The commands to execute the step are taken from the menu and are written below the images

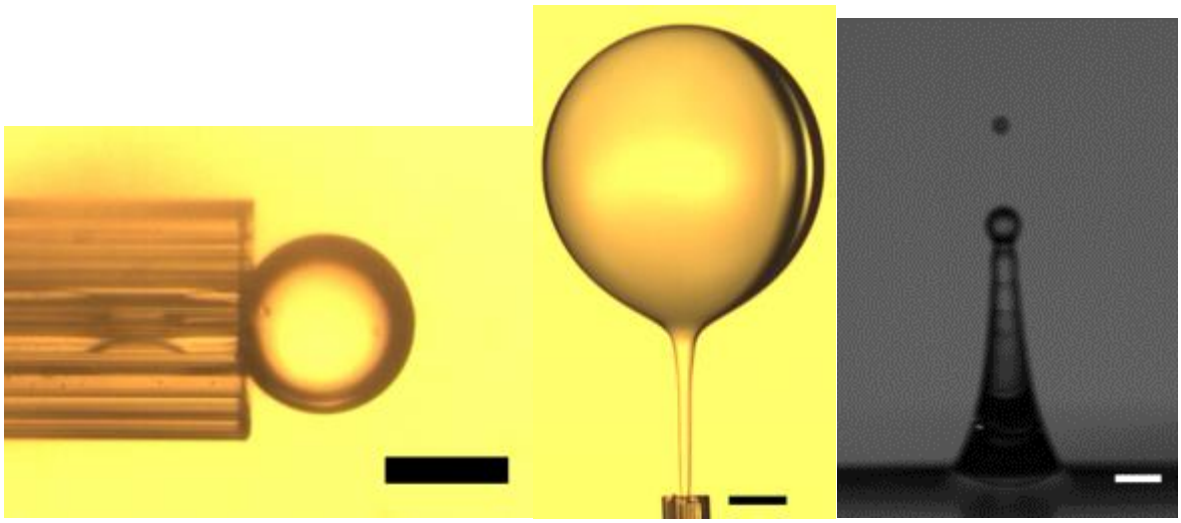

Original example snapshots (including scale bars; from left to right, 200 μm, 500 μm, 2000 μm). The right image is recorded in grey scale.

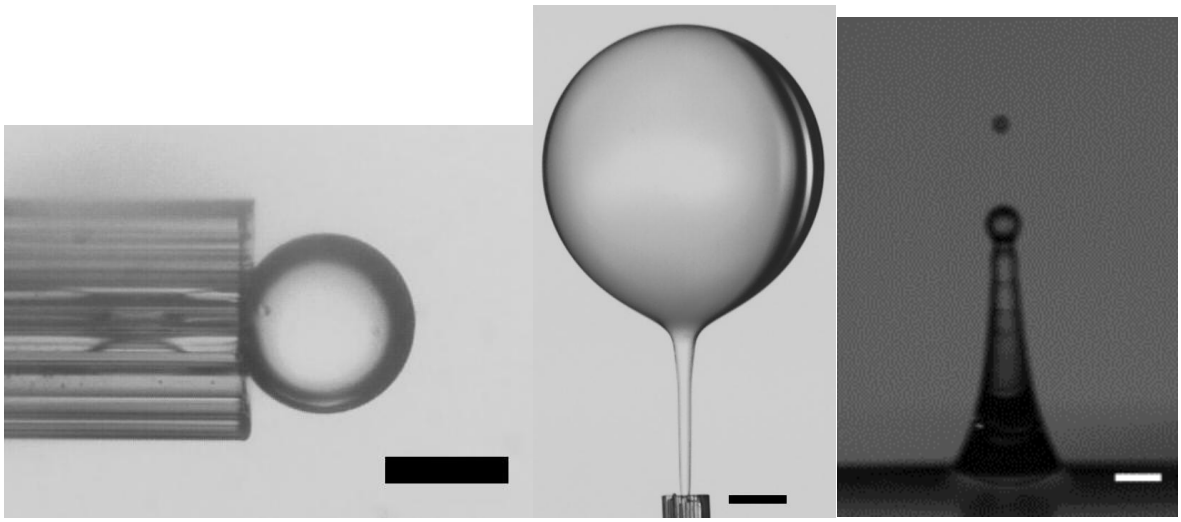

Convert to grey scale: Image – Type – 8-bit

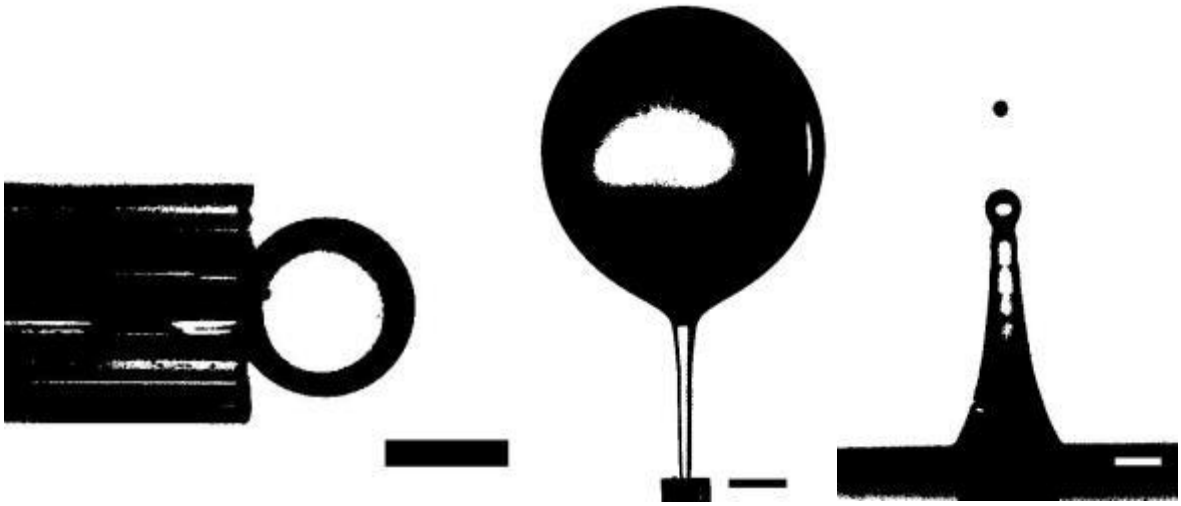

Apply threshold: Image – Adjust – Threshold... Choose threshold method: "Default" or "Huang"

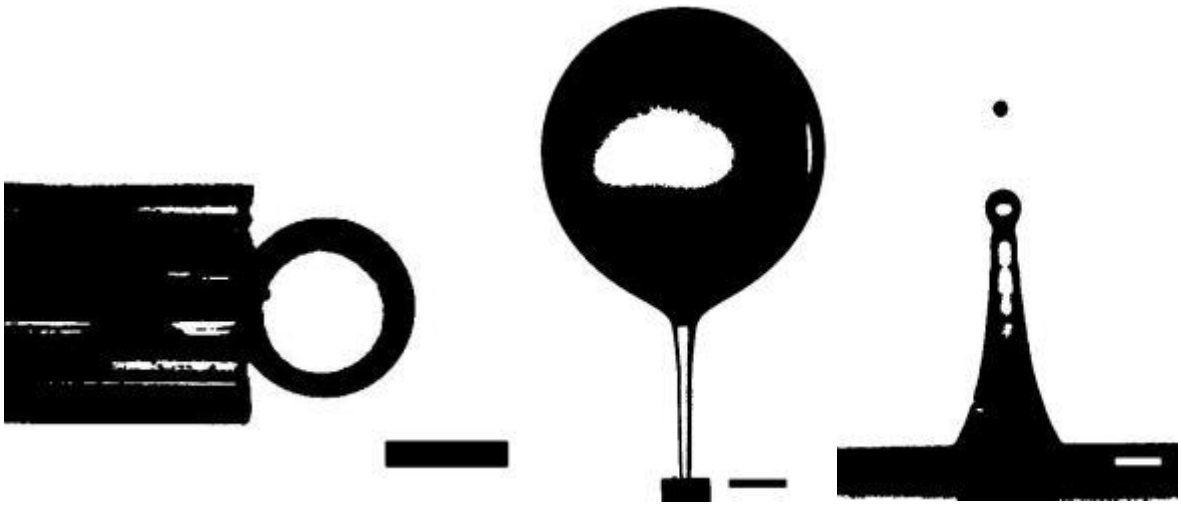

Remove noise: Process – Noise – Despeckle

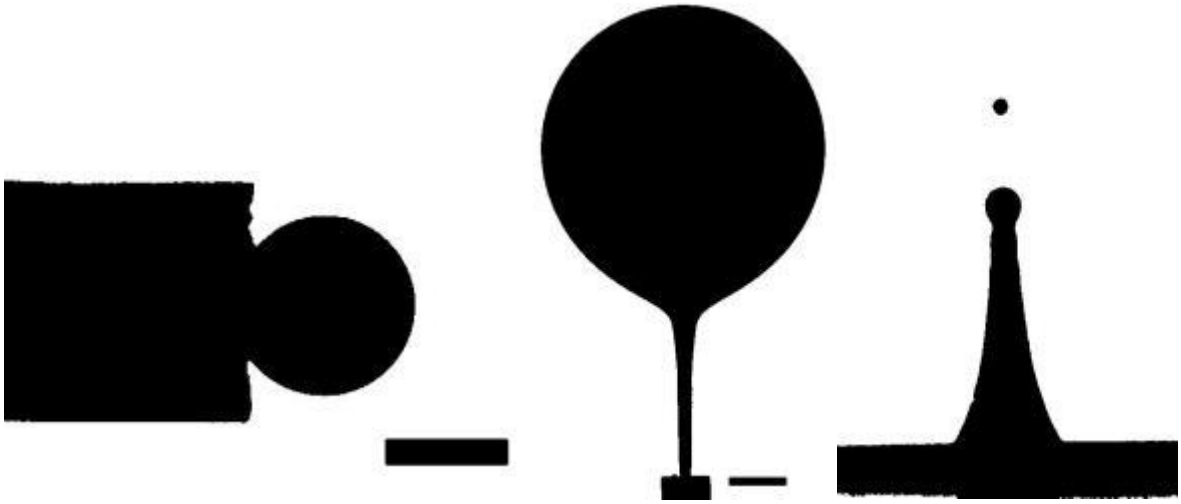

Fill holes: Process – Binary – Fill Holes

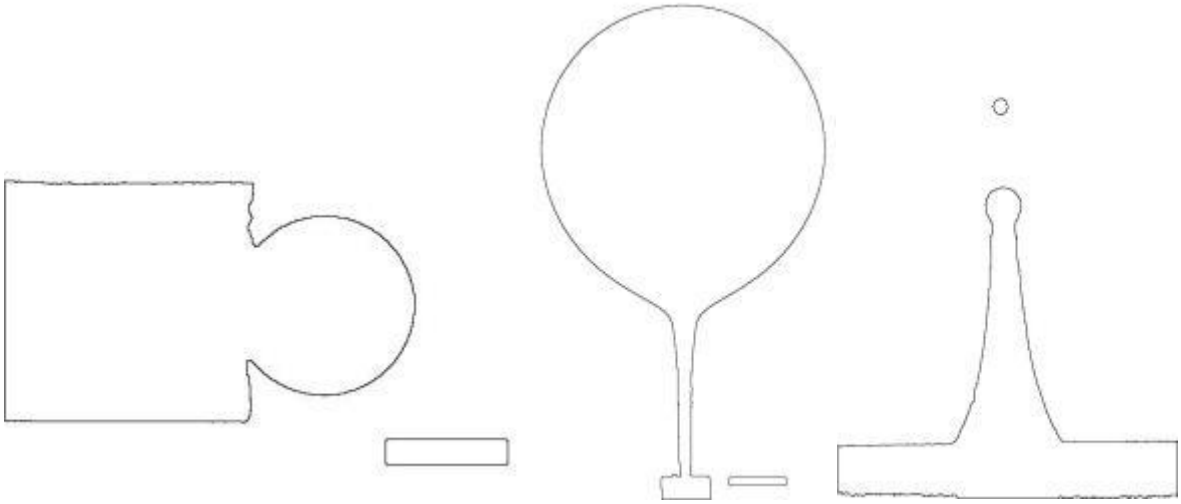

Retrieve the outline: Process – Binary – Outline

Save the coordinates of the pixels of the outline:

Analyze – Tools – Save XY Coordinates... The coordinates are saved in a ".txt"–file with in the first column, the x-coordinate, in the second column, the y-coordinate, and third column, slice number.

Processing coordinates by Matlab

- Load the coordinates in Matlab
- Define the axisymmetric axe
- Calculate the radius of the shapes
- Write data to excel and text document

Further processing is done in MS Excel

- Calculate flow rates, velocities, deceleration, volumes, surface areas, etc.
- Graphical images have been made in MS excel

Appendix B

Table 1. Dimensionless values for h, R, $2/R_c$, of equation (12) of Chapter 5 and relative error *RE.* The dimensionless volume of the jet above h is defined as $V_{jet}(h) = \int_h^\infty \pi R^2(h)dh$. The total volume of the jet above h=0 is bounded and estimated to be 6.67.

h	R	$1/R_c$	m_{jet}	RE (%)
~0	~1.66	~0	~6.67	
0.1000	1.4645	0.1013	5.9198	1.29
0.2000	1.3279	0.1992	5.3098	-0.44
0.3000	1.2198	0.2975	4.7995	-0.86
0.4000	1.1293	0.4002	4.3649	0.04
0.5000	1.0514	0.5034	3.9897	0.68
0.6000	0.9831	0.6048	3.6632	0.81
0.7000	0.9222	0.7042	3.3765	0.60
0.8000	0.8672	0.8021	3.1234	0.27
0.9000	0.8173	0.8994	2.8992	-0.06
1.0000	0.7715	0.9968	2.6994	-0.32
1.1000	0.7296	1.0946	2.5213	-0.49
1.2000	0.6910	1.1932	2.3617	-0.56
1.3000	0.6554	1.2927	2.2183	-0.56
1.4000	0.6225	1.3929	2.0891	-0.51
1.5000	0.5922	1.4938	1.9724	-0.42
1.6000	0.5641	1.5951	1.8667	-0.31
1.7000	0.5381	1.6968	1.7707	-0.19
1.8000	0.5140	1.8100	1.6833	0.55
1.9000	0.4917	1.9005	1.6033	0.03
2.0000	0.4709	2.0024	1.5301	0.12
2.1000	0.4517	2.1042	1.4629	0.20
2.2000	0.4337	2.2058	1.4009	0.26
2.3000	0.4171	2.3072	1.3438	0.32
2.4000	0.4015	2.4085	1.2908	0.36
2.5000	0.3869	2.5096	1.2417	0.39
2.6000	0.3733	2.6106	1.1961	0.41
2.7000	0.3605	2.7114	1.1536	0.42
2.8000	0.3486	2.8121	1.1139	0.43
2.9000	0.3373	2.9126	1.0767	0.43
3.0000	0.3267	3.0130	1.0419	0.43
3.1000	0.3167	3.1132	1.0092	0.43
3.2000	0.3073	3.2135	0.9785	0.42
3.3000	0.2984	3.3136	0.9495	0.41
3.4000	0.2900	3.4137	0.9222	0.40
3.5000	0.2821	3.5137	0.8963	0.39
3.6000	0.2745	3.6137	0.8719	0.38
3.7000	0.2673	3.7136	0.8487	0.37
3.8000	0.2605	3.8135	0.8267	0.36
3.9000	0.2540	3.9134	0.8058	0.34
4.0000	0.2478	4.0132	0.7859	0.33
5.0000	0.1991	5.0112	0.6301	0.22
6.0000	0.1662	6.0091	0.5255	0.15
7.0000	0.1426	7.0074	0.4507	0.11
8.0000	0.1249	8.0061	0.3945	0.08
9.0000	0.1110	9.0051	0.3507	0.06
10.0000	0.0999	10.0042	0.3157	0.04

Table 2. Relation between the radius R_{base} of the jet at the base, the total mass of the jet (without droplet formation at the tip) and the induced deceleration according to our model for water as a liquid at 24ºC. The jet is visible rising out of the water surface with a dimensionless base radius $R(h{\sim}0.1)$ defined as $R_{base} \equiv 1.5$. The total mass of the jet is calculated using the dimensionless volume V_{jet} starting from h=0 (see table 1).

R_{base} (µm)	d (µm/µs²)	m_{jet} (pg)
1.5	100	3.58
3.0	22	34.6
R_{base} (µm)	d (µm/µs²)	m_{jet} (ng)
6.0	6.0	0.24
12	1.3	2.41
24	0.35	17.3
R_{base} (µm)	d (mm/ms²)	m_{jet} (µg)
48	90	0.13
96	23	1.03
192	6.0	7.9
384	1.3	76.3
768	0.35	546
R_{base} (mm)	d (m/s²)	m_{jet} (mg)
1.5	100	3.58
3.0	22	34.7
6.0	6.0	243
12	1.3	2410
R_{base} (mm)	d (m/s²)	m_{jet} (g)
24	0.4	13.0
48	0.09	132.5
96	0.023	1025
192	0.0058	7900

Appendix C

Towers of Liquid

Authors: Cees J.M. van Rijn[1] and Willem G.N. van Heugten[1]

[1] Micro Fluidics and Nano Technology, Wageningen University,
Laboratory of Organic Chemistry, Dreijenplein 8,
6703HB Wageningen, The Netherlands.

A drop splashing in a deep liquid may reappear as a small tower of liquid with on top a new forming drop. This tower, often referred as a liquid jet, emanates from the middle of a cavity that is created by the splashing drop. It is well accepted that collapse of the cavity is the main driver for upward liquid motion and that specific flow field patterns around the base of the liquid jet will determine its shape. Here we show that the liquid tower or jet has a universal concave shape above its base and that it continuously reshapes itself due to a pressure equilibrium between inertial and surface tension forces. An inertial deceleration dependent Young-Laplace equation is introduced to describe the jet shape and is experimentally verified for different fluid viscosities and surface tension values. Drops growing on these liquid jets have an initial size related to the inertial deceleration of the jet. We predict the existence of very large sized, but very slow decelerating jets, that best can be observed in a gravitation free environment. Like the Young-Laplace equation is known to describe the convex shape of sessile drops experiencing gravity, we here postulate that the Young-Laplace equation can be used to exactly describe the concave shape of liquid jets experiencing inertial deceleration, herewith mathematically connecting drops with towers of liquid.

Overlooking a nearby surface of a pool when it is raining is a good place to observe the phenomenon; small jets and accompanying drops emanate from the surface a short while after raindrops have hit the surface. The whole duration including impact of the raindrop, the outburst with rise and fall of a jet is typically less than one hundred ms. An event may become imprinted on our retina; a conical shaped tower of liquid with a droplet on top. All the manifold appearances of such liquid towers and drops have inspired artists and photographers, and slow motion versions are known through commercials. That a new drop really comes from the original falling drop is easy to proof by a simple experiment: let a drop of milk fall in black coffee from a height of about 5-10 cm. Newly formed droplets coming from the jet will be nearly as white as milk. The history of the description of the phenomenon starts in the late 19th century[1,2] when A.M. Worthington observed that a small jet may emanate from the water surface a short while after impact of a small falling object. Numerous studies on this phenomenon have been carried out since then[3-7] focusing mainly on different fluid responses, such as coalescence or splashing and central jet formation[3,6,8-12], that can be distinguished when a small object or droplet hits the water surface from a given height. In the case of coalescence the falling object is just absorbed by the surface. In the case of splashing the impacting object first creates a cavity in the fluid surface; a round crown will next form around the cavity and either a jet may arise at the centre, and/or the crown might rupture in many tiny fragments[8,12]. If the impact energy is moderate to high, the jet rising to its apex may emit one or more droplets[5], whereas the last droplet having not sufficient energy to escape may rest and grow on the tip. The jet and especially the emitted droplets can reach significant heights[6,7], higher than the starting position from which the object or droplet falls in the water surface to create the cavity.

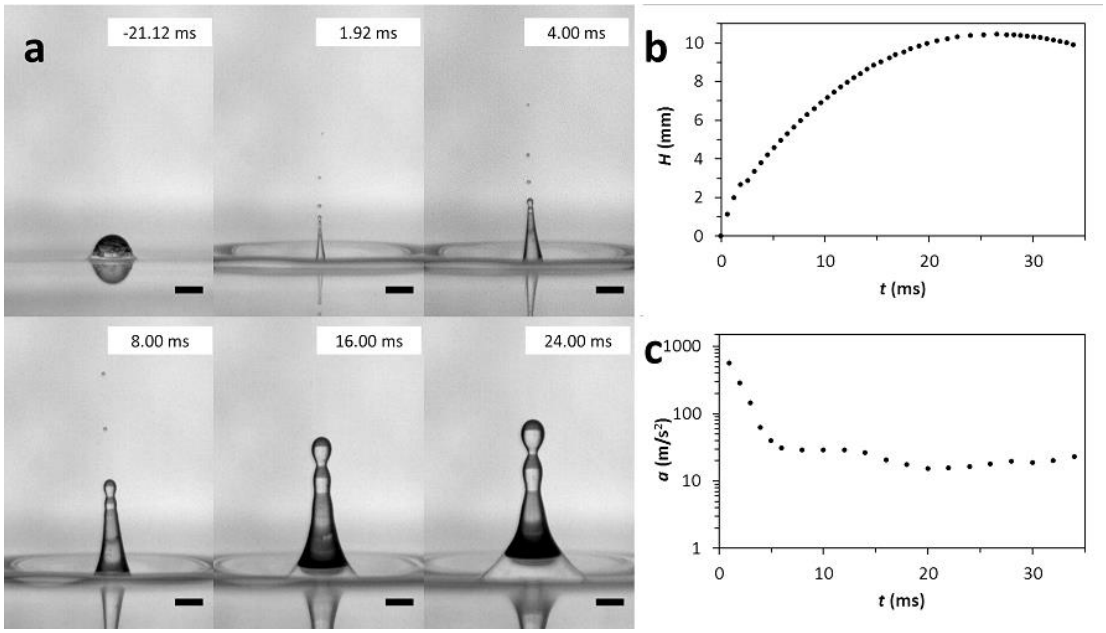

Figure 1 The rise of a pure water jet at 24ºC . **a** Sequential snapshots after impact of a 3.4 mm sized droplet. Scale bars are 2000 μm. **b** The height H of the tip grows to 10.6 mm in 24.0 ms. **c** Time dependent deceleration $a(t)$ as derived from the time plot of $H(t)$. The initial deceleration is estimated to be more than 500 m/s^2, but after 16 ms the total deceleration becomes nearly constant a = 20±2 m/s^2. Please note that the measured $a(t)$ of the tip is always higher than the contribution from gravity g (9.81 m/s^2).

Jets emanating from deep liquid have a typical concave conical shape, which keeps this form up to the moment that the jet has reached its apex, and even thereafter. A general shape for a rising jet has to our knowledge never been proposed, possibly because jet shape and evolution seemed always substantially determined by complex and case specific flow conditions during cavity collapse prior to its rise. Gekle et al. demonstrated that fluid near the jet acquires a vertical upward momentum in a small acceleration zone located around the jet base[4,10], and that jet evolution can be obtained from the flow field at the base. In principle this model[10] of jet formation can possibly be used for predicting the shape of the jet itself. Here an added mechanism is introduced to describe the jet shape: the jet will reshape itself above the fluid surface by surface tension forces acting directly on the surface of the jet, and through inertial deceleration of the inner fluid, due to the surface tension based retraction of the jet towards the deep liquid. Are other forces relevant? Gravity plays a minor role: realize that although the jet is continuously connected to the deep liquid surface all the mass ejected above the surface is essentially in a free fall. If this mass would not be connected to the bath it would reshape itself into a spherical droplet with a form not determined by gravity. Here the mass is still connected to the deep liquid surface and will therefore experience an inertial deceleration originating from the surface tension trying to pull back the mass to the deep liquid. What about viscous forces?. Although the liquid mass launched from the bath has a considerable initial velocity (typical 1-10 m/s) we show in SI 1 that velocity field differences (denoted as δv_i) both in axial and radial direction inside the rising jet and corresponding viscous pressures will not contribute much to jet shape, at least for low viscosity fluids up to 45 mPa·s, in accordance with current findings[4,10]. According to our hypothesis inside the jet therefore mainly a time dependent inertial deceleration $d(t)$ of the local jet fluid due to the surface tension based retraction of the jet towards the fluid surface exists. Its value along the jet with respect to the fluid surface at a given height h and time t is: $P_{inertial} = \rho h d(t)$. This deceleration can be considered in a first approximation constant along the jet (there is no h dependence in $d(t)$ itself), implying that the inertial pressure difference between the base and the tip of the jet is equally distributed. However the value of $P_{inertial}$ is h dependent; thus the higher the jet with tip height $H(t)$ at time t, the higher the deceleration pressure difference ($= \rho H(t) d(t)$) between the tip and base of the jet. Fig. 1c shows deceleration $a(t)$, and note that $d(t) = a(t) - g$.

The tip of the jet is closed by a spherical cap, which normally evolves rapidly to a droplet with radius R_d (with Laplace pressure $2\gamma/R_d$). A prediction for R_d can be derived, by stating that the Laplace pressure of a just or nearly formed droplet will match the inertial deceleration pressure $P_{inertial}$:

$$2\gamma / R_d = \rho H d \quad \text{or} \quad R_d = 2\gamma / \rho H d \qquad (1)$$

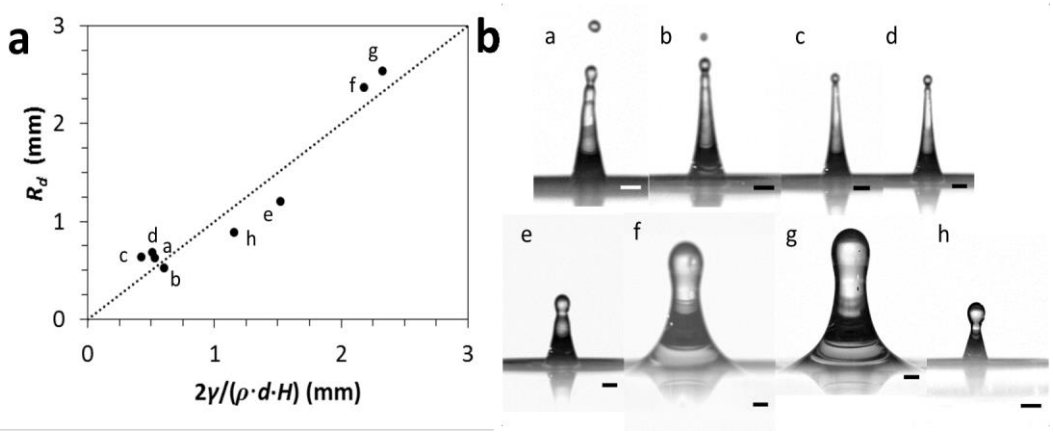

Figure 2 a Plot of droplet radius R_d versus $2\gamma/\rho Hd$ for a nearly formed droplet on top of the jet. Drawn line corresponds with equation (1). **b** Corresponding snapshots of the points depicted in **a** for different fluids (η = 1-45 mPa·s and γ = 34-72 mN/m). Fluid labels: a water, b-e 60% glycerol, f-g 78% glycerol, and h 1% tween 20.

The inertial pressure at the tip seems indeed to correlate well with the Laplace pressure inside the droplet (Fig.2). The just formed droplet at the tip can be viewed as an 'on board' inertial pressure meter (cf. the inertial pressure difference of the air between front and back of a cabin of an airplane when it is accelerating; this is actually $\rho hd(t)$, with ρ the density of air, h the length measured from the front of the cabin, and $d(t)$ the actual acceleration/deceleration of the airplane).

We now focus on the interplay between the droplet and the jet. During the rise of the jet in the first 4 ms the inertial pressure at the tip starts large (>500 m/s^2), but declines very rapidly (~20 m/s^2, Fig. 1c). In this first stage droplets will be emitted from the tip due to high deceleration forces, because the formed droplets acquire (inertial) mass and will be easily launched[5]. The deceleration of the tip however becomes smaller and from 4 ms onwards a spherical cap evolves towards a still connected droplet having about a size being twice the size of the tip radius. The Laplace pressure of the droplet $P_{drop} = 2\gamma/ R_d$ and of the tip $P_{tip} = \gamma/ R_{tip}$ will then match, hence creating a quasi-stable pressure equilibrium. However, a further rise of the tip height H will enlarge the inertial pressure $\rho Hd(t)$ and the droplet will experience an influx of liquid, will grow, lower its Laplace pressure, herewith destabilizing the pressure equilibrium. During the further rise and descent of the tip accompanied by the droplet this situation will not alter, the Laplace pressure of the droplet has become and remains smaller than the Laplace pressure of the tip and the droplet continues to grow with liquid flowing upward through the tip. Although this growing droplet phenomenon is often observed, breakup mechanisms, such as Rayleigh breakup[18] and Eggers universal pinching[19] can still prematurely interrupt the interplay between the growing droplet and the jet tip[5] (see also SI 2).

Now we return to the time dependent shape of the jet. The surface tension is the main force acting on the liquid jet above the fluid surface and will try to counteract any other force by keeping the total surface area of the jet as small as possible. Also the formed jet will experience a downward deceleration force $d(t)$ originating from the same surface tension force to bring back the liquid to the deep liquid. We also know that the transformation of the surface energy stored in the bended cavity and its subsequent collapse is the main driving force to emanate the liquid, and that a very thin upward acceleration zone around and just outside the base of the jet exists to fuel the jet[4,10], making the jet mass larger in time during its rise. However as stated earlier all the liquid that exists above this thin upward acceleration zone will be subject to the surface tension force acting on the liquid jet above the fluid surface and will try to keep the total surface area of the jet as small as possible. We assume therefore that inside the jet above the fluid surface the main force balance is determined by the inertial

pressure $P_{inertial}$ build-up along the jet (originating from the retraction of the jet) and the Laplace pressure with value $P_{Laplace} = \gamma / R_c(t,h)$ with $R_c(t,h)$ the reciprocal curvature of the jet at height h at time t and thus postulate:

$$\rho h d(t) = \gamma / R_c(t,h) \qquad (2)$$

Equation (2) is mathematically related to the well-known (time independent) hydrostatic Young-Laplace equation ($\Delta P = \rho h g - \gamma / R_c(h)$) valid for the convex shape of sessile drops and is also related to a (time independent) equation describing the concave shape of the meniscus around a small circular cylinder[20,21]. Equation (2) is a modified Young-Laplace equation describing the concave shape of a jet experiencing a time dependent inertial deceleration/acceleration. We have solved numerically equation (2) and have derived an analytical approximation for the inverse function (of $R(h)$ being the height) $h(R)$ as a function of the jet radius R for our fluid regime:

$$h(R) = \left[e^{-\sum_{i=0}^{n} a_i \left(\sqrt{\frac{\rho d}{\gamma}} \mathrm{R} \right)^i} \right] \frac{\gamma}{\rho d(t)} \frac{1}{\mathrm{R}} \qquad (3)$$

Constants a_i in the polynomial expansion for n = 12 are: a_3 = 0.58, a_6 = -0.0265, a_9 = 0.002, a_{12} = 0.0032, with other a_i = 0 (Fig. 3e and SI 3).
In a slender jet approximation the axial contribution to the local curvature can be neglected in equation (2) and we get $R_c(h) = R(h)$ yielding:

$$R(h) = \gamma / \rho d(t) h \qquad (4)$$

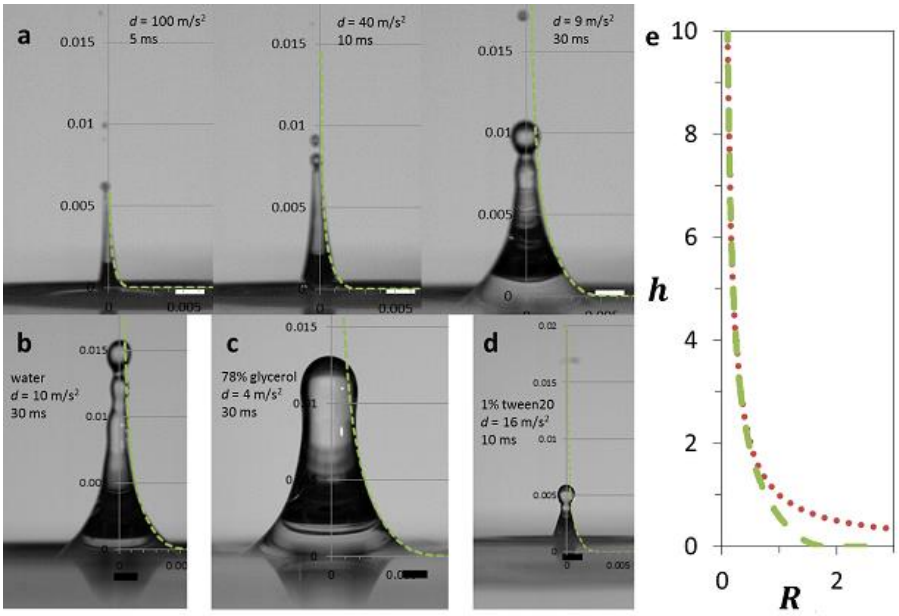

Figure 3 Sequential snapshots of different jets just before reaching the apex. **a** three time frames of a 60% glycerol jet, **b** water **c** 78% glycerol, **d** 1% tween20, **a-e** Plotted values according to solution eq. 3, (green dashed line), and **e** also depicted the slender jet approximation eq.4 (red dotted line), valid for dimensionless h values larger than *2*.

Based on analysis of the experimental results we notice that our hypothesis seems correct (see Fig.3). Please note that the Eiffel tower shaped green dotted line (solution eq. 3) is fully and solely determined by the physical measurable parameters ρ, $d(t)$ and γ. Also the dimensionless value of the jet radius $R(h)$ is almost zero at R= 1.5 with corresponding h values smaller than 0.1. About 90% of all liquid is confined between $0<R(h)<1.5$. We have therefore defined a dimensionless value of the radius for the jet base $R(h<0.1) \equiv R_{base} \equiv 1.5$ (see also SI 3).
Next we focus on the origin of $d(t)$ by looking more closely at the surface tension based retraction of the jet towards the bath. The circumference of the jet at height h has value $2\pi R(h)$ and it exerts a

pulling surface tension force $\boldsymbol{F}_{st}(h)$ with a force component directed along the axis of the jet: $F_{ax}(h) = 2\pi R(h)\gamma\cos(\theta)$, with θ being the local inclination angle with respect to the h axis of the jet. $F_{ax}(h)$ will act on all the mass of the jet between h and H including the drop and herewith induces a downward deceleration $d(t)$:

$$2\pi R(h)\gamma\cos(\theta) = d(t)\left(m_{jet}(h) + m_{drop}\right) = d(t)\left[\int_h^H \rho\pi R^2(h)dh + m_{drop}\right] \qquad (5)$$

with $m_{jet}(h)$ the mass of the jet between h and H, and m_{drop} the mass of the drop on the tip of the jet.

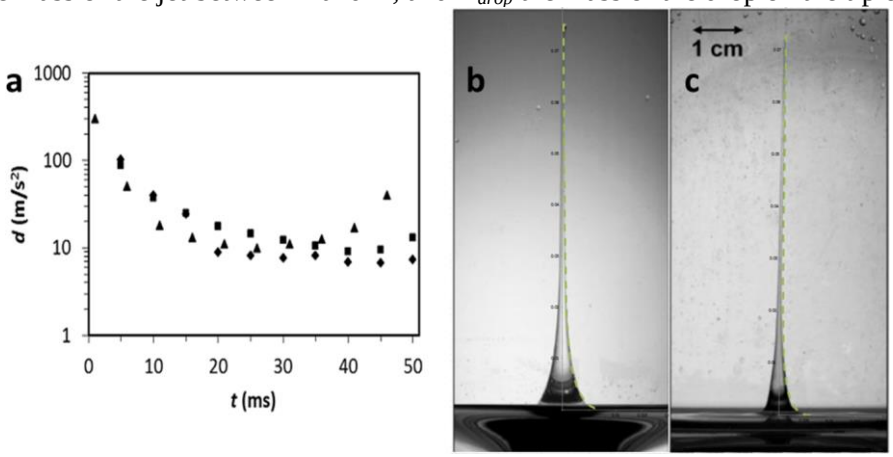

Figure 4 Measured and fitted deceleration $d(t)$ values for glycerol jets. **a** Threefold plot of $d(t)$ for a 60% glycerol solution. (♦) Derived from the rise of the tip height $H(t)$ corrected with the contribution from gravity $d(t) = a(t) - g$. (▲) According to best $d(t)$ fit of solution eq. 3 to the experimental curve. (■) According to eq. 5 with the integral taken from h=0 to the apex point H and including a mass contribution from the connected droplet, **b,c** Fitted jet shapes according to eq. 3 (green dotted line) for a glycerol jet from reference[17]. Here a tall standing wave is generated in a tank producing a deep depression, which collapses to a singularity herewith forming a jet.

The deceleration $d(t)$ of the jet according to eq. 5 has been calculated from the experimental data (from photographs only and taking the integral from 0 to H), see the (■) symbols depicted in Fig. 4a. Also plotted here the other two methods to estimate $d(t)$: as derived from the (time dependent) rise of the tip corrected for the gravitational motion (♦) , and as derived by fitting the shape of the jet according to eq.2 and its proposed solution eq.3 with symbols (▲). All three methods seem to match with the found $d(t)$ values, especially all three methods give very high deceleration values at the initial rise of the jet. We find thus supporting evidence that the origin of the measured deceleration (corrected with gravity) of the jet as soon as it appears above the cavity surface is the surface tension based retraction of the jet towards the bath as expressed in eq. 5, and has a shape as proposed by eq.2 and 3. There is also supporting evidence from literature[17] (see Fig.4b,c); we have taken physical parameters (mass density and surface tension) and have fitted the dimensionfull jet shape according to model (eq.3, green dotted line) using deceleration as fit parameter. For Fig.4b we find a deceleration value of 4±0.3 m/s^2, which gives according to eq.3 an R_{base} of 5.8 ±0.5 mm and a m_{jet} of 360 ±20 mg, and for Fig. 4c with a deceleration value of 7±0.5 m/s^2, we find an R_{base} of 4.4 ±0.4 mm and a m_{jet} of 160±20 mg. Both the derived R_{base} and m_{jet} values of both jets acc. to eq.3 match within error margin with the direct dimensional analysis of the photographs. This implies that the model describes quite accurately the shape of a liquid jet (solution eq.3) even at quite large values of h (green dotted lines in Fig.4b,c), and that the model seems valid for jets generated other than by a falling droplet.

We now continue with the descent phase of the 60% glycerol jet, see Fig. 5 (and Fig.3a). From the apex at t = 25.0 ms onwards the base of the jet broadens gradually to a straight cone with on top as it seems part of the original jet up to about t = 40 ms. At about t = 45 ms the original slender part of the jet has seemingly disappeared.

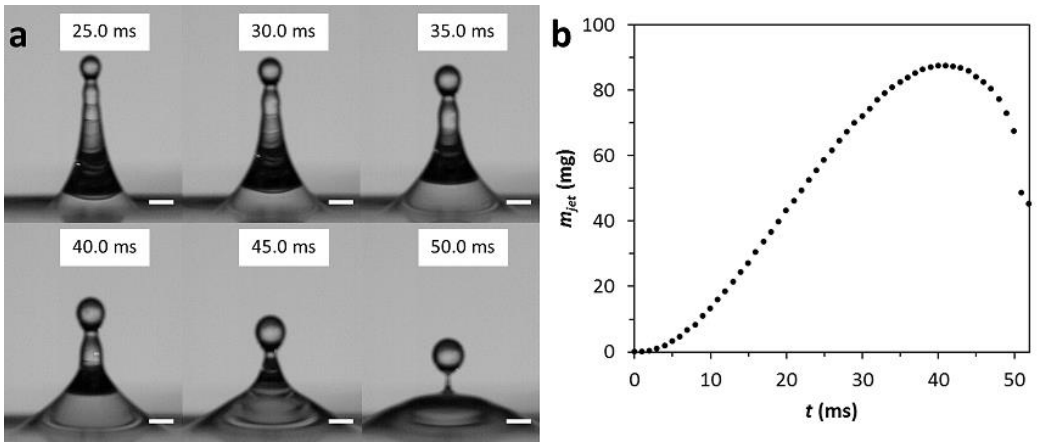

Figure 5 Evolution after reaching the apex point. **a** The jet experiences at the base a strong radially directed force to broaden the base of the jet (see also SI2). **b** Total mass of the jet is plotted in time and includes the mass of the droplet attached to the jet.

.

Is the lower part of the jet here following another fluid dynamics? Remember that all the fluid above the fluid surface originates form a thin upward acceleration zone around its base[4,10]. Are here the downward decelerating jet and the still upward acceleration zone meeting each other? Please note that the total mass above the liquid surface still increases (up to 40 ms, see Fig 5b) even after the jet has reached its apex, pointing indeed to a considerable contribution of a still upward moving zone. A more detailed approach for the fluid dynamics in the descent phase for the base of the jet seems therefore appropriate.

Table 1

R_{base} (µm)	d (µm/µs^2)	m_{jet} (ng)
6.0	4.5	0.378
12	1.1	3.13
24	0.28	24.4
R_{base} (µm)	d (mm/ms^2)	m_{jet} (µg)
48	70	0.195
96	18	1.50
192	4.2	13.3
384	1.1	99.0
768	0.28	771
R_{base} (mm)	d (m/s^2)	m_{jet} (mg)
1.5	72	5.91
3.0	18	47.3
6.0	4.5	378
12	1.1	3130
R_{base} (mm)	d (m/s^2)	m_{jet} (g)
24	0.28	24.4
48	0.07	195
96	0.018	1495
192	0.0042	13270

Relation between the induced deceleration according to eq. 3, the total mass of the jet (without droplet formation at the tip) and the radius R_{base} of the jet at the base with $R_{base} \equiv R(h{\sim}0.1)$. The liquid is here water at 24ºC. The total mass of the jet m_{jet} is calculated using the dimensionless volume V_{jet} for $0<h<\infty$; nearly 11% of the total jet volume is present between h=0 and h=0.1 (see also Fig.3e and Table S3).

To our current understanding a novel model for the jet shape is proposed that might also be relevant for applications wherein inertial acceleration and interfacial effects occur simultaneously, e.g. tail evolution of inkjet drops[13,14], solid nanojets formed with pulsed laser deposition[15], microjets induced by cavitation[16], and free-surface singular jet phenomena[17]. The presented model is predicted to be valid in a broad range of dimensions and physical parameters.

The model is exact and based on physical measurable parameters only. For water (see Table 1) we predict the existence of diminutive jets e.g. with a base radius of 10 um having a deceleration of about 2 µm/µs^2 and a total mass of 1 ng. The model as shown in Fig. 4b,c also predicts the shape of generated jets[17,22] using singular collapsing depressions of standing waves. We further predict the existence of extra-large and ultra-slow deceleration liquid tower jets (Table 1). Such large jets however can only be generated and observed in a nearly gravitation free environment in view of the small associated inertial deceleration with respect to gravitational acceleration. The experiment would entail a partially filled standing cylindrical tank placed in a nearly gravitation free environment subject

to slow but firm (vertically) oscillations until at a specific resonant frequency in the middle of the fluid surface jetting occurs because the local surface tension is broken by the appearance of a surface singularity[17]. The generated jet may initially decelerate very much like presented in Fig. 1c from several hundred m/s^2 (depending on the sharpness and total mass (< 1 mg) of the initial singularity) to a few m/s^2 when the total jet mass has increased to about 1 gram. When the jet mass further increases to about 200 gr the associated surface tension based inertial deceleration will decrease then to about 70 mm/s^2, whereas the base diameter of the jet will grow to 100 mm. Please realize that in space the potential energy needed to elevate 200 g above the fluid surface is a fraction of the gravitational energy needed at earth, and that the total energy stored in the local upward moving fluid prior to the rise of the liquid tower will finally determine how much mass it will contain and how towering it will become.

References

1. Worthington, A. M. On Impact with a Liquid Surface. *Proc. R. Soc. London* **34**, 217–230 (1882).
2. Worthington, A. M. & Cole, R. S. Impact with a Liquid Surface Studied by the Aid of Instantaneous Photography. Paper II. *Philos. Trans. R. Soc. London Ser. A, Contain. Pap. a Math. or Phys. Character* **194**, 175–199 (1900).
3. Rein, M. Phenomena of liquid drop impact on solid and liquid surfaces. *Fluid Dyn. Res.* **12**, 61–93 (1993).
4. Gekle, S. & Gordillo, J. M. Generation and breakup of Worthington jets after cavity collapse. Part 1. Jet formation. *J. Fluid Mech.* **663**, 293–330 (2010).
5. Gordillo, J. M. & Gekle, S. Generation and breakup of Worthington jets after cavity collapse. Part 2. Tip breakup of stretched jets. *J. Fluid Mech.* **663**, 331–346 (2010).
6. Yarin, A. L. Drop impact dynamics: Splashing, spreading, receding, bouncing... *Annu. Rev. Fluid Mech.* **38**, 159–192 (2006).
7. Rein, M. The transitional regime between coalescing and splashing drops. *J. Fluid Mech.* **306**, 145–165 (1996).
8. Zhao, H., Brunsvold, A. & Munkejord, S. T. Investigation of droplets impinging on a deep pool: Transition from coalescence to jetting. *Exp. Fluids* **50**, 621–635 (2011).
9. Manzello, S. L. & Yang, J. C. An experimental study of a water droplet impinging on a liquid surface. *Exp. Fluids* **32**, 580–589 (2002).
10. Geckle S., Gordillo J. M., van der Meer D., Lohse D. High-Speed Jet Formation after Solid Object Impact. *Phys. Rev. Lett.* **102,** 034502 (2009).
11. Nespresso spot, http://www.youtube.com/watch?v=cLPqWXy029g (2013).
12. Marston J. O., Thoroddsen S. T. Apex jet from impacting drops. *J. Fluid Mech.* **614,** 293-302 (2008).
13. Bos, van der, A. et al., Velocity Profile inside Piezoacoustic Inkjet Droplets in Flight. Phys. Rev. Applied **1**, 014004 (2014).
14. Martin G.D., Hoath S.D., and M Hutchings I.M., Inkjet printing - the physics of manipulating liquid jets and drops, Journal of Physics: Conference Series **105**, 012001 (2008).
15. Unger, C. et al. Time-resolved studies of femtosecond-laser induced melt dynamics. *Optics Express* **20**, 24864-24872 (2012).
16. Mitragotri,S., Healing sound: the use of ultrasound in drug delivery and other therapeutic applications. *Nature Reviews Drug Discovery* **4**, 255-260 (2005).
17. Zeff, B. W., Kleber, B., Fineberg, J. & Lathrop, D. P. Singularity dynamics in curvature collapse and jet eruption on a fluid surface. *Nature* **403**, 401–404 (2000).
18. Rayleigh, Lord. On the Capillary Phenomena of Jets. *Proc. R. Soc. London* **29**, 71–97 (1879).
19. Eggers, J. Universal pinching of 3D axisymmetric free-surface flow. *Phys. Rev. Lett.* **71**, 3458–3460 (1993).
20. James D. F. The meniscus of the outside of a small cylinder. *J. Fluid Mech*. **63,** 657-664 (1974).
21. Boucher E. A. & Jones T. J. G. Capillary Phenomena. *J.C.S. Faraday I.* **76,** 1419-1432 (1980).
22. Hogrefe, J. E. *et al*. Power-law singularities in gravity-capillary waves. *Phys. D Nonlinear Phenom.* **123**, 183–205 (1998).
23. Brenner, M. P., Lister, J. R. & Stone, H. A. Pinching threads, singularities and the number 0.0304. *Phys. Fluids* **8**, (1996).

Acknowledgements

We thank Howard Stone (Princeton Univ.) and Jens Eggers (Bristol Univ.) for stimulating discussions. Herman ten Berge (BFI Optilas) helped with high-speed camera data acquisition. This work was supported by the MicroNed program.

Supplementary information

Materials and methods

Experiments were performed under ambient atmosphere at 24 °C. A petri dish with diameter of 146 mm and height of 18 mm was completely filled with water and mixtures of water with glycerol. Viscosities, interfacial tensions and densities of the different aqueous solutions are listed in table S1. A syringe was placed over the centre of the petri dish at a certain distance. From this syringe a droplet, of

the same aqueous mixture as in the petri dish, was generated with a radius between 1.7 and 2.2 mm. The distance between syringe and bath defines the impact velocity of the droplet, which was in the range of 1.0 to 3.1 m/s. The impact of the droplet on the liquid surface and resulting rise and fall of a jet was recorded with high speed camera (FASTCAM Mini UX100) are frame rate of 6000 and 8000 fps (frames per second) and resolution of 1280 x 616 pixels. The recorded images were processed by computer software ImageJ and Matlab.

Table S1. Viscosities, interfacial tensions and densities of the different aqueous solutions used in our experiments (for 24 °C).*

	Viscosity (mPa·s)	Surface tension (mN/m)	Density (kg/m^3)
Water	0.91	72	998
60% glycerol	9.1	67	1155
78% glycerol	45	65	1204
~1% tween20	0.91	34	998

*Gallant RW. 1967. Physical properties of hydrocarbons. Part 14. Propylene glycols and glycerine. Hydrocarb. Process. 46(5):201–15; and Dorsey NE. 1940. *Properties of Ordinary Water-Substance in All Its Phases: Water Vapor, Water, and All the Ices;*. New York: Reinhold Publishing Corporation.

SI 1 Velocity field differences and viscous contributions

The velocity field differences δv_i inside the rising jet, both in axial and radial direction, and related viscous forces are considered of low viscosity fluids up to 45 mPa·s. The corresponding viscous pressure contributions follows equation $p_{viscous} = \eta.\delta v_i/R_{tip}$ or $p_{viscous} = \eta.\delta v_i/R_{base}$ The velocity field differences in radial direction can be estimated from the change in time of the radius of the tip R_{tip} of the jet and/or at the base of the jet R_{base}. The δv_i in axial direction can be estimated from the filling speeds of the jet through the base of the jet, and filling speed of the droplet on top of the jet through the tip of the jet.

Table S2. Axial and radial velocity field differences δv_i and corresponding viscous pressures $p_{viscous}$, jet radius at the base and tip, and corresponding approximated Laplace pressure $p_{Laplace}$ estimated from jets of different fluids.

Axial direction

	At base				At tip			
	R_{base} (mm)	δv_i (m/s)	$p_{viscous}$ (Pa)	$p_{Laplace}$ (Pa)	R_{tip} (mm)	δv_i (m/s)	$p_{viscous}$ (Pa)	$p_{Laplace}$ (Pa)
Water	2.6	0.21	0.08	28	0.45	0.20	0.45	160
60% glycerol	2.0	0.21	0.94	34	0.50	0.37	6.72	134
78% glycerol	5.0	0.11	0.97	13	2.1	0.12	2.47	31
~1% tween20	1.2	0.40	0.33	28	0.49	0.29	0.60	69

Radial direction

	At base				At tip			
	R_{base} (mm)	δv_i (m/s)	$p_{viscous}$ (Pa)	$p_{Laplace}$ (Pa)	R_{tip} (mm)	δv_i (m/s)	$p_{viscous}$ (Pa)	$p_{Laplace}$ (Pa)
Water	1.5 – 5.9	0.11	0.07	12 – 47	0.4 – 0.5	0.020	0.05	140 – 190
60% glycerol	2.7 – 6.2	0.11	0.38	11 – 25	0.3 – 0.5	0.016	0.56	140 – 240
78% glycerol	4.1 – 5.8	0.07	0.75	11 – 16	2.1 – 2.2	0.014	0.29	30 – 31
~1% tween20	0.8 – 2.5	0.08	0.10	14 – 42	0.3 – 0.5	0.019	0.07	71 – 120

The estimated Laplace pressures according to $p_{Laplace} = \gamma/R_{tip}$ or $p_{Laplace} = \gamma/R_{base}$ are found substantially larger than the viscous pressures. These results confirm with earlier work that confirms that viscous dissipation is low inside the already formed jet. The jet is here considered as a ballistic region, where fluid particles experience no further acceleration and move constantly with the velocity obtained at the end of the acceleration region at the base of the jet[4].

SI2 Jetting and breakup of droplets from the tip

Jetting of droplets from the tip and breakup of an interconnecting liquid bridge or neck is often observed. Break up due to capillary deceleration of the liquid at the tip inducing a perturbation by a capillary mechanism has also been reported[4,5]. However these breakup mechanisms can be severely delayed when the flow of liquid from the tip towards the droplet has a large velocity v: in these cases often a quasi-stable neck between the tip and the droplet is observed (see also Fig 5a). This neck acts then as a Bernoulli venturi between the tip and the droplet creating a pressure drop of ρv^2 to compensate the driving pressure difference p_{tip} - p_{drop}, and will try to maintain a fluid passage.

Here we propose following Gordillo & Gekle[5] that deceleration forces might contribute to the actual break-up, in particular we focus here on the actual moment of breakup of the liquid bridge connecting the jet and the droplet.

As long as the surface tension force of the liquid bridge (F_{neck}) with value $F_{neck} = 2\pi\, R_{neck} .\gamma$ is larger at some time t than the deceleration force exerted on the mass of the droplet $F_{deceleration} = m_{droplet} . d(t)$ the liquid bridge or neck will remain intact. However the liquid bridge or neck may break up as soon $F_{deceleration} > F_{neck}$ or $R_{neck} < m_{droplet} . d(t) / 2\pi.\gamma$. Herewith we can predict a minimum radius of the neck before break-up:

$$R_{neck} < m_{droplet} d(t) / 2\pi\gamma \qquad \text{(S1)}$$

This equation gives us an indication of the radius of the liquid bridge or neck before a droplet is emitted and also applies to the radius of the neck R_{neck} in Fig. S1.

We find for the condition for a sudden snap-off or break-up of R_{neck} in Fig. S2 a value of 210 to 240 µm according to equation (S1) with values of $m_{droplet}$ is 13.4 mg and deceleration of $d(t)$ = 7.0 ± 0.5 m/s^2. The evolution of R_{neck} is plotted about 2 ms before break-up happening between 50.5 and 51.0 ms (Fig. S2).

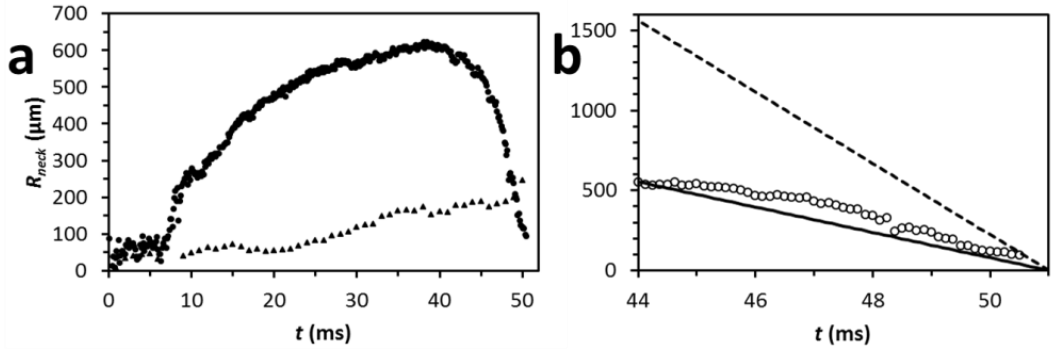

Figure S1 a Time plot of the liquid bridge radius R_{neck} between the tip of the jet and the droplet (●) and the condition according to equation (S1) (▲). Where both plots meet at t= 48.5 ms the pinch off of the liquid bridge (micro-thread or neck) starts. **b** Time plot of R_{neck} (○). Dashed and solid line according to different predictions from the universal pinching theory. The universal pinching process stops as soon as the condition stated in equation (S1) has been reached.

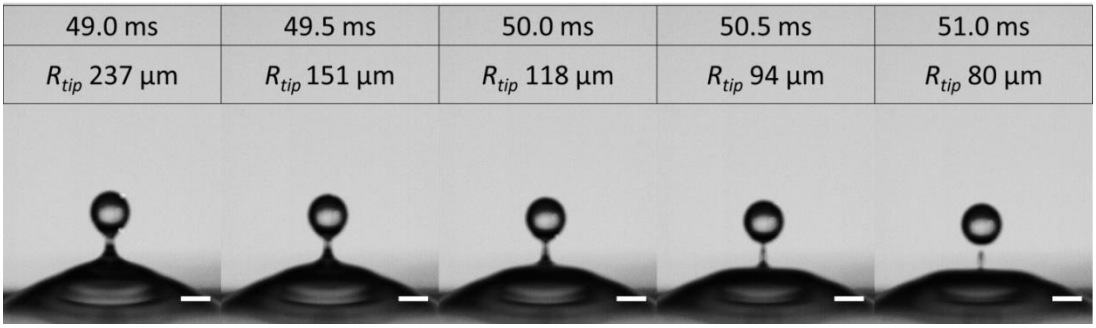

Figure S2 Five snapshots of the last 2 ms before break-up. Scale bars are 2000 µm. See also Figure 5.

The last stage of breakup of the neck between the last droplet and the tip during descend of the liquid jet may follow the universal pinch off mechanism proposed by Eggers[19]. The radius of the neck may follow different conditions for pinch off according to equation (S2) of ref [23].

$$R_{neck}(t) = S_{\min}\frac{\gamma}{\eta}\left(t_{breakup} - t\right) \qquad \text{with} \qquad S_{\min} = \frac{1}{60N - 27} \tag{S2}$$

In Fig. S1b the dashed line corresponds to N=1; S_{min} is 0.0303 and the solid line with N=2; S_{min} is 0.0108.

SI3 Curvatures, the shape of the liquid jet and the governing Young-Laplace equation

For non-slender jets we have to take into account the axial curvature $1/R_{ax}$ to the total curvature therefore the total local curvature $1/R_c$ is given by the sum of $1/R_{ra}$ and $1/R_{ax}$ (see Fig. S3), and get:

$$\frac{1}{R_c(h)} \equiv \frac{1}{R_{ra}(h)} + \frac{1}{R_{ax}(h)} = \frac{1}{R(h)\sqrt{1+R'^2(h)}} - \frac{R''(h)}{\left(1+R'^2(h)\right)^{3/2}} \tag{S3}$$

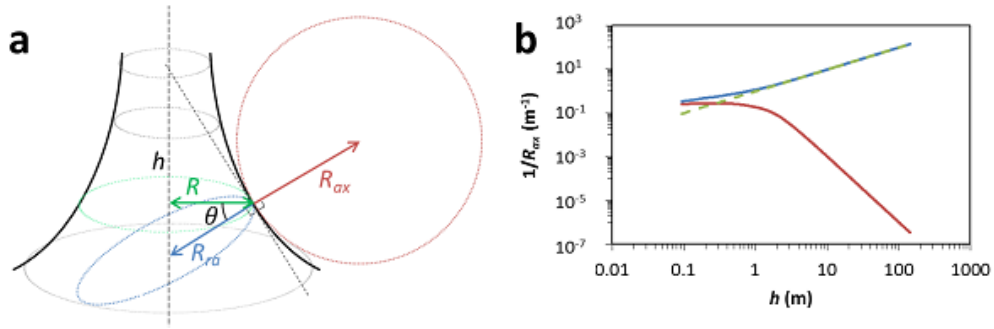

Figure S3 Curvature $1/R_c$ split in the two principle curvatures $1/R_{ra}(h)$ and $1/R_{ax}(h)$. **a** Schematic representation, **b** values calculated from approximate solution (S6) (blue) $1/R_{ra}(h)$ and (red) $-1/R_{ax}(h)$, the green dashed line is the sum of both and obeys equation (S4).

Pressure equilibrium between the Laplace Pressure and the inertial deceleration pressure:

$$\frac{1}{R_c(h)} = \frac{\rho d(t) h}{\gamma} \tag{S4}$$

In the slender jet approximation the axial contribution $1/R_{ax}(h)$ to the local curvature $1/R_c(h)$ can be neglected and we get $1/R_c(h) = 1/R_{ra}(h)$. The first derivative in this radial component can be neglected leaving $1/R_c(h) = 1/R(h)$ yielding:

$$R(h) = \frac{\gamma}{\rho d(t)}\frac{1}{h} \tag{S5}$$

This slender jet approximation gives a relative deviation less than 1% in the dimensionless (γ/ρd≡1) regime for 2.5<h<100.

Likewise we can try to solve equation (S3,S4) with iteration using solution (S5) as a first estimate for large h. We derived an approximate analytic solution for the height $h(R)$ as a function of the jet radius R.

$$h(\boldsymbol{R}) = \left[e^{-\sum_{i=0}^{n} a_i \left(\sqrt{\frac{\rho d}{\gamma}}\boldsymbol{R}\right)^i}\right]\frac{\gamma}{\rho d}\frac{1}{\boldsymbol{R}} \tag{S6}$$

for n = 12 we have:

a_3 = 0.58, a_6 = -0.0265, a_9 = 0.002, a_{12} = 0.0032, with other a_i = 0.

The polynomial approximation gives a relative deviation in $h(R)$ less than 1% in the dimensionless (γ/ρd≡1) regime for 0.1<h<100.

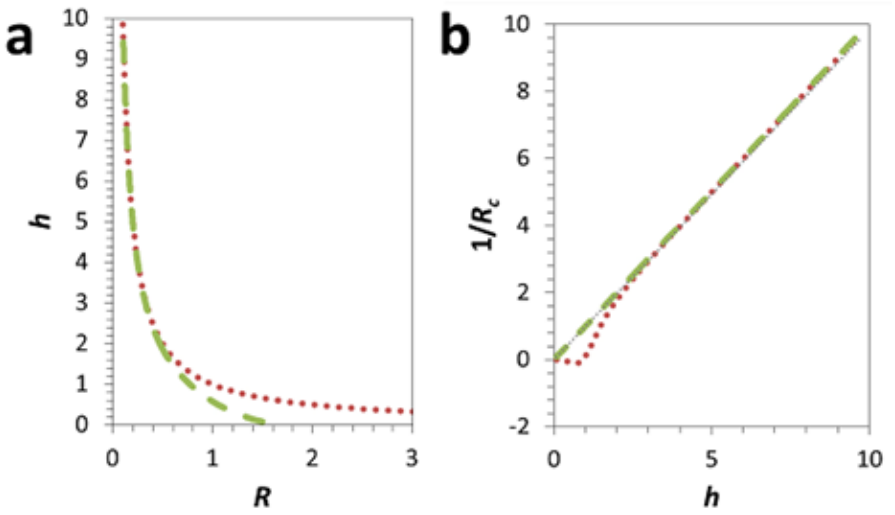

Figure S4 a Axial shape of the jet according to (red dotted line) approximate solution (S5) and (green dashed line) to the more approximate solution (S6). R_{base} is here defined at the point corresponding with the dimensionless point h=0.1 and has a value of R_{base} = 1.5. **b** The curvature $1/R_c(h)$ plotted versus h (green dashed line) according to solution eq. (S6) and (red dotted line) to solution eq. (S5). The polynomial approximation (green dashed line) gives an excellent match with an error less than 1% in the regime for $0.1<h<100$.

Approximate solutions (S5) and (S6) are compared for accuracy to the Young-Laplace equation in Fig S4a. Both approximate solutions follow the same trend at higher h, but not for small h. The solution (S6) (marked with green squares) is in excellent agreement to the governing Young-Laplace equation also for the emanating jet close to the liquid surface up to h = 0.1. Most of our experimental data confirm the theoretical predicted Eiffel tower shape solution (S6) as depicted in Fig S4a (green dashed line).
In Figure 3 a number of different rising jets have been depicted with an overlay of a fit (green dashed line) according to solution eq. (3 or S6). Please realize that solution (3 or S6) is fully determined by physical measurable parameters ρ, $d(t)$ and γ.

In our model we have assumed that the deceleration $d(t)$ is constant along the h axis. To our understanding this is a reasonable assumption, because it follows from an equal distribution of the inertial pressure difference between the base and the tip of the jet. As soon as the jet arises with a sharp tip out of the surface, the surface tension at the base will start to decelerate the tip and will try at the same time to keep the surface area as small as possible. The deceleration of the tip will impose an equally distributed inertial pressure difference along the h axis, which forms the boundary condition to reshape the liquid of the jet according to the introduced eq.2 (or S4). For larger h values a $R(h)\sim 1/h$ dependence is found for the shape of the jet. We can use this to calculate what the mass is of the jet above a specific height h.

$$m_{jet}(h)=\left[\int_h^{\infty}\rho\pi R^2(h)dh\right] \qquad \text{(S7)}$$

A remarkable observation is that if we substitute S7 in equation (5) and we assume the slender jet approximation we can calculate what the maximum deceleration $d_{max}(h)$ at a given height h is before pinch off or rupture of the jet occurs :

$$2\pi R(h)\gamma \geq d_{max}(h)m_{jet}(h) \quad \text{or} \quad d_{max}(h)\leq 2d \qquad \text{(S8)}$$

This means that the maximum allowed deceleration $d_{max}(h)$ at any point h is always half of the actual deceleration d. The jet is thus safe against rupture induced by inertial forces.

Table S3. Dimensionless values for h, R, $1/R_c$, of equation (3) and relative error RE. The dimensionless volume of the jet above h is defined as $V_{jet}(h) = \int_h^\infty \pi R^2(h)dh$.

The total volume of the jet above h=0 is bounded and estimated to be 6.67.

h	R	$1/R_c$	V_{jet}	RE (%)
~0	~1.66	~0	~6.67	
0.1000	1.4645	0.1013	5.9198	1.29
0.2000	1.3279	0.1992	5.3098	-0.44
0.3000	1.2198	0.2975	4.7995	-0.86
0.4000	1.1293	0.4002	4.3649	0.04
0.5000	1.0514	0.5034	3.9897	0.68
0.6000	0.9831	0.6048	3.6632	0.81
0.7000	0.9222	0.7042	3.3765	0.60
0.8000	0.8672	0.8021	3.1234	0.27
0.9000	0.8173	0.8994	2.8992	-0.06
1.0000	0.7715	0.9968	2.6994	-0.32
1.1000	0.7296	1.0946	2.5213	-0.49
1.2000	0.6910	1.1932	2.3617	-0.56
1.3000	0.6554	1.2927	2.2183	-0.56
1.4000	0.6225	1.3929	2.0891	-0.51
1.5000	0.5922	1.4938	1.9724	-0.42
1.6000	0.5641	1.5951	1.8667	-0.31
1.7000	0.5381	1.6968	1.7707	-0.19
1.8000	0.5140	1.8100	1.6833	0.55
1.9000	0.4917	1.9005	1.6033	0.03
2.0000	0.4709	2.0024	1.5301	0.12
2.1000	0.4517	2.1042	1.4629	0.20
2.2000	0.4337	2.2058	1.4009	0.26
2.3000	0.4171	2.3072	1.3438	0.32
2.4000	0.4015	2.4085	1.2908	0.36
2.5000	0.3869	2.5096	1.2417	0.39
2.6000	0.3733	2.6106	1.1961	0.41
2.7000	0.3605	2.7114	1.1536	0.42
2.8000	0.3486	2.8121	1.1139	0.43
2.9000	0.3373	2.9126	1.0767	0.43
3.0000	0.3267	3.0130	1.0419	0.43
3.1000	0.3167	3.1132	1.0092	0.43
3.2000	0.3073	3.2135	0.9785	0.42
3.3000	0.2984	3.3136	0.9495	0.41
3.4000	0.2900	3.4137	0.9222	0.40
3.5000	0.2821	3.5137	0.8963	0.39
3.6000	0.2745	3.6137	0.8719	0.38
3.7000	0.2673	3.7136	0.8487	0.37
3.8000	0.2605	3.8135	0.8267	0.36
3.9000	0.2540	3.9134	0.8058	0.34
4.0000	0.2478	4.0132	0.7859	0.33
5.0000	0.1991	5.0112	0.6301	0.22
6.0000	0.1662	6.0091	0.5255	0.15
7.0000	0.1426	7.0074	0.4507	0.11
8.0000	0.1249	8.0061	0.3945	0.08
9.0000	0.1110	9.0051	0.3507	0.06
10.0000	0.0999	10.0042	0.3157	0.04

Summary

This thesis explores relevant fluid dynamic processes for the formation of uniformly sized droplets in microfluidic systems. Growing droplets made from a bulk source have often liquid threads or jets in between to supply liquid to the droplet. Liquid threads and jets are however known to be instable and finding parameters determining their instability/stability will possibly promote a more controlled formation of uniformly sized droplets. Different droplet formation processes in microfluidic devices are explained, such as cross-flow, co-flow and flow focussing.

Dimensionless numbers (introduced in chapter 1) represent the ratio of relevant forces or pressures acting on the fluids and/or their interfaces. These forces and pressures originate from their related fluid dynamic parameters, such as viscosity, interfacial tension, mass density and velocity of the fluid within a specific fluidic confinement with a certain length scale. We show that the dimensionless Reynolds, Weber and Capillary numbers can be associated with the stability of liquid threads and/or jets and provide insight in droplet formation processes.

The phenomenon of spontaneous droplet formation at low flow rates of an inner fluid confined in a microfluidic channel is studied in chapter 2. A short overview of known processes of spontaneous droplet formation with micro-engineered microfluidic devices is presented. We have studied the process of auto breakup with rectangular and round glass capillaries, the latter provided with micro-corrugations and uniform sized droplets were obtained, but only if the outer fluid is able to enter the capillary during droplet formation.

The process of auto breakup is described by a new analytical model described in chapter 3. The model states that the instability of a liquid thread is induced by the decrease of a local liquid thread pressure inside the capillary near the growing droplet. Predicted droplet sizes have been experimentally verified accurately, and also the predicted breakup length inside a micro-corrugated capillary has been verified. The model states that viscous flow stabilises the liquid thread and that auto breakup happens as long as the capillary number is below a critical capillary number of 0.0625. Above 0.0625 droplets grow infinitely large. Auto breakup is however already hampered at Capillary numbers above 0.03, because between 0.03 and 0.0625 no well controlled droplet sizes

could be obtained by auto breakup. This is explained by the observed formation of a partially collapsed inner liquid thread that remains open and supplies the growing droplet with inner fluid.

In chapter 4 the formation and stability of a liquid thread in free surface flow feeding a large growing droplet is demonstrated and discussed. The shape of the liquid thread is positively tapering (towards the droplet) and can be described accurately by a Navier-Stokes based ordinary differential equation (ODE) assuming steady state, axisymmetry and an averaged fluid velocity over the cross section of the liquid thread. The axial shape of a viscous liquid thread is concave and its radial dimension has initially a cubic dependence with respect to the axial dimension. A driving force to stabilise the liquid thread was identified, which is a pressure gradient $Q = Q_0/L - Q_1$. Q_0 is the pressure drop over thread length L, and Q_1 is interfacial based dissipation of energy of the outer fluid. The maximum length of the liquid thread is predicted to be reached when Q goes towards 0 as the ratio Q_0/Q_1.

Shape and stability of emanating liquid jets, which appear after impact of falling droplets from a deep liquid, is presented in chapter 5. During rise and fall of the jet due to gravity, the jet is additionally decelerated towards the liquid surface by a tensile retraction force from the surface tension force exerted on the jet surface by the liquid bath. The retracting force generates an inertial deceleration pressure inside the jet that is balanced by the local Laplace pressure, herewith defining its local curvature and therefore also the shape of the complete jet. A deceleration based Young-Laplace equation is introduced and the predicted shape is experimentally verified for different fluids. Furthermore, the size of droplets forming on the tip of the jet can also be explained by the found pressure balance between the local Laplace pressure and the inertial deceleration of the jet (including the forming droplet).

In general we found that the stability of a liquid thread or jet seems correlated with an applied pressure difference that is distributed between the begin and end of the thread or jet. Studying auto breakup (chapters 2 and 3) of a confined liquid thread it was found that only when the applied pressure is high enough the liquid thread is stable and infinitely large droplets are formed. For the free surface flow liquid thread (chapter 4) it was found that breakup happens when the applied pressure gradient over the length of

the thread goes to zero. For the emanating jet (chapter 5) an inertial pressure difference between the base and tip of the jet comes into existence that opposes the squeezing Laplace pressure that wants to break up the liquid jet. Furthermore we found that the last stages of droplet breakup from a liquid thread or jet appeared to follow universal pinch-off, and also that micro-thread formation is observed between droplet and liquid thread or jet.

Acknowledgements

Useful contributions to science, the scientific community, and society require countless discussions and deeper reflections with others. Many people have been involved in my PhD project to enhance knowledge and understanding of the behaviour of fluids in relation to droplet formation as written in this PhD thesis. Here I would like to acknowledge everybody who has been involved, contributed and helped me with my PhD.

My promotor and supervisor Cees van Rijn I would like to acknowledge for his guidance on the analytical models for auto breakup in chapter 3 and the emanating liquid jet in chapter 5, which are for a large extent his design. Thanks also for his unceasing efforts to teach me scientific writing. His enthusiasm about the dynamic phenomena of fluids and keenness to unravel the physics is inspiring and motivated me to drift away from chemistry to the physics of fluids. Special thanks to Jaap Molenaar for his contribution to propose a mathematical model based on the work of Jens Eggers in chapter 4, which helped us to formulate stability criteria for liquid threads. I have learned a lot during our meetings and developed progressive mathematical insights on ODE's.

The department Laboratory of Organic Chemistry I thank for hosting my PhD project. I have shared the office with Ai Nguyen and Nagesh Wagdare, and the laboratories also with Jerome Paques and Tin Doan, with much pleasure and I thank them for help and support of all the different problems. The nice and inspiring environment of ORC was made possible by all people of ORC. Here I thank Ronald de Bruin for ordering chemicals and lab equipment, Elbert van der Klift for GPC and CE, Frank Claassen for LC-MS, Barend van der Lagen for NMR and FTIR, Remco Regeling for help with machinery, Anne-Marie Franssen and Cees van de Haar for their help with practical teaching, Elly Geurtsen, Aleida Ruisch, Linda Kaster for being a helping hand with all administrative work, Jos Paulusse, Mabel Caipa Campos and Hamilton Kakwere for sharing polymer chemistry and also TuHa Vong, Kim de Lange, Bart Rijksen, Ruud Cuypers, Annemarie Huijbrechts, Marloes Schurink, Aliaksei Pukin, Luc Scheres, Michel Rosso, Milena Rosso-Vasec, Jurjen ter Maat, Kishore Tetela, Feng Li, Paul Könst, Tijs Lammens, Loes Ruizendaal, Radostina Manova, Yessie Sarie, Anke Trilling, Jacinthe Gagnon, Florine Duval, Medea Kosian, Rickdeb Sen, Digvijay Gahtory, Nagendra Bhairamadgi, Sourav Bhattacharjee, Saurabh Srivastava, Satesh Gangarapu, Umesh Chinnaswamy

Panchatcharam, Sidhu Pujari, Aline Debrassi, Jaime Garcia-Hartjes, Alexandre Villela, Christy Nguyen, Sjoerd Slagman, Tjerk Sminia, Bas van den Berg, Esther van Andel, Sweccha Joshi, Wouter Biesta, Wilco Duvivier, Jorin Hoogenboom, Fred van Geenen, Yao Shen, Pepijn Geurtjes, Bram Bielen, Nishant Sewgobind, Ganesan Palaniswamy, Rajesh Ramaneti, Jacob Baggerman, Rokus Renirie, Peter Steunenberg, Stefanie Lange, Ankush Mane, Zhanhua Wang, Menglong Yang, Fatima Garcia Melo, Jorge Escorihuela Fuentes, Txema Alonso Carnicero, Steven Calder, Hendra Willemen, Judith Firet, Anke Kuijk, Tanja Verwijst, Esther Roeven, Jelmer van der Rijst, Johanna Molenaar, Nadine Verstappen, Ton Marcelis, Maurice Franssen, Teris Verbeek, Tom Wennekes, Maarten Smulders, Maarten Posthumus, Carel Weijers, Han Zuilhof, Michel Nielen, Ernst Sudhölter, Erik van Rozendaal, Frans Kampers for interesting discussions and support.

The department of Physical Chemistry and Soft Matter I thank for their help on CLSM and PAT tensiometer and trained me on operating these machines. I also thank the department of Physics and Physical Chemistry of Foods for their help on rheometers, density meter, and PAT tensiometer. And I thank the department of Food Process Engineering for using their high speed camera. I thank the people from MicroNed consortium and WP-IIA.

For the evaluation of this PhD thesis I thank the committee Jasper van der Gucht, Jacco Snoeijer, Michiel Kreutzer, and Hans Reinten. Here I also thank Jacob Baggerman, Coen Hendriksen, Ai Nguyen, Anke Kuijk, Wim van Heugten, and Ellen Wemmenhove for reading previous versions of the PhD thesis and/or providing critical comments.

Here I also would like to thank my family and friends for all their support and help during my time as a PhD student. Among those I am honoured to have Inge Minten and Jacob Baggerman as my paranymphs. One very special person I would like to thank is Ellen Wemmenhove, because of her help and support during the last two years.

Willem

About the author

Willem van Heugten was born on 12 September 1981 in Duiven, the Netherlands. After graduation from secondary school, Liemers College, in 2001 he started studying Molecular Life Sciences at Radboud University Nijmegen, the Netherlands. He did an internship on the topic of virus capsids at Organic Chemistry at Radboud University Nijmegen, and an internship on crystallography of enzymes and computational dynamics of proteins at Dundee University, United Kingdom. Directly after obtaining his Master of Science degree in 2007 he started his PhD project on droplet formation and fluid dynamics in microfluidic systems at the Laboratory of Organic Chemistry at Wageningen University, the Netherlands under supervision of Cees van Rijn. The main results of this PhD project are presented in this thesis. From 2012 until 2014 he worked as a Scientist at Aquamarijn Micro Filtration BV and from 2014 until present he worked at Micronext BV.

List of publications

Dead-end emulsification in the auto breakup regime, W.G.N. van Heugten, C.J.M. van Rijn, 2009, Physics@FOM Veldhoven, The Netherlands

Spontaneous droplet formation in microfluidic devices, W.G.N. van Heugten, C.J.M. van Rijn, 2010, World Conference on Emulsions, Lyon, France

On the stability of viscous liquid threads, C.J.M. van Rijn, W.G.N. van Heugten, and J. Molenaar, submitted

Rise and Fall of a Liquid Jet: The physics behind jet shape and droplet size, C.J.M. van Rijn and W.G.N. van Heugten, submitted

Auto breakup: Analytical model for breakup of confined liquid threads, W.G.N. van Heugten and C.J.M. van Rijn, submitted

Overview of completed training activities

Discipline specific activities

Courses

Food hydrocolloids: Fundamentals and applications, WUR, 2009

Advanced Organic Chemistry, WUR, 2009-2011

Meetings

Annual NWO conference Organic Chemistry, 2007-2011

Annual MicroNano conference, 2008-2011

MicroNed meetings, 2007-2011

*Physics@FOM Veldhoven, the Netherlands, 2009

*World emulsion congress, Lyon, France, 2010

* Represents oral presentations. Posters have been presented at the other conferences.

General courses

VLAG PhD week, 2008

Techniques for writing and presenting a scientific paper, WU Library, 2011

Workshop: pictures, tables and infographics in your research, WUR, 2011

Advanced course: Guide to scientific artwork, WU Library, 2011

Optionals

Group meetings & Colloquia, Laboratory of Organic Chemistry, 2007-2011

PhD study-trip, organised by Laboratory of Organic Chemistry, China, 2009

PhD study-trip, organised by Laboratory of Organic Chemistry, UK, 2011

Preparation of Research Proposal

Part of the research described in this thesis was financially supported by the Dutch MicroNed program.

Thesis layout: By the author

Cover page design: By the author
Picture was taken by Herman ten Berge (Acal BFi Nederland BV)

Published by: CPI - KONIKLIJKE WÖHRMANN